学 位 論 文

Formation and Chemical Dynamics of the Galaxy and Globular Clusters
(銀河系と球状星団の形成と化学力学進化)

平成11年12月博士（理学）申請

東京大学大学院理学系研究科
天文学専攻

中 里 直 人

Ph.D. thesis

Formation and Chemical Dynamics of the Galaxy and Globular Clusters

NAKASATO, Naohito

Department of Astronomy, School of Science,

University of Tokyo

Abstract

In this thesis, I present the results of the numerical simulations of the globular cluster formation and the formation of the Galaxy. I adopt the Smoothed Particle Hydrodynamics (SPH) method to construct the self-consistent three-dimensional dynamical and chemical models for the formation of stellar systems. To simulate the formation of a stellar system from gases, own SPH code treats three different particles as dark, gas and star particles. The gravity between these particles is computed by the special purpose computer GRAPE to accelerate calculations (GRAPE-SPH code). I incorporate the various physical processes associated with the formation of stellar systems, i.e., radiative cooling and star formations. The formed stars affect the dynamics and chemical properties of the gas component by way of the energy and mass ejection. For these feedback processes by stars, the Type II and Ia supernovae explosion and stellar winds are considered. As a result, the chemical evolution of gases is implemented self-consistently. In own GRAPE-SPH code, the chemical evolution of total metal (Z), iron (Fe) and oxygen (O) are computed with the fixed metallicity yield.

Using own GRAPE-SPH code, I investigate the formation processes of the globular clusters. I assume that, in the collapsing galaxy, isothermal cold clouds form through thermal condensations and become proto-globular clouds (PGC). With this assumption, I calculate the size of PGC by solving the linearized equations for perturbation. The result of the solution of the linearized equations is used as initial conditions for three-dimensional calculations. The evolution of the inner region of the PGC is computed with own GRAPE-SPH code. When the initial gases contain no heavy elements, the evolution of proto-clouds sensitively depends on the initial radius. For the smaller initial radius, the initial star burst is so intense that the subsequent star formation occurs in the central regions to form a dense star cluster as massive as the globular cluster. When the initial gases contain some heavy elements, the metallicity of gases affects the evolution and the final stellar mass. If the initial radius of the proto-globular clouds was relatively large, the formation of a star cluster as massive as the globular clusters requires the initial metallicity as high as $[\mathrm{Fe/H}] \geq -2$. The self-enrichment of heavy elements in the star cluster does not occur in all cases.

All previous numerical models of the formation of the Galaxy have lacked the proper treatment of the chemical evolution and/or the required spatial resolutions. In this thesis, I construct the detailed model of the formation and evolution of the Galaxy using own GRAPE-SPH code. To efficiently generate the proper initial conditions, we adopt the path integral method. By computing the dark matter evolution of each spherical region, I examine the properties of the resulted halos and select the desired halo for hydrodynamical simulations. From the result of the hydrodynamical simulations, I make the detailed comparison between the model galaxy and the number of observational facts of the Galaxy. By categorizing the stellar components with the metallicity and age, the model galaxy consists of three components as the Galaxy. Each stellar component shows similar properties with the properties of the Galaxy. The early evolution of the model reveals that the most bulge stars form during the sub-galactic merger that occurred in the region where the potential is deepest. Because of the strong star burst induced by the mergers, the metallicity distribution function of the bulge stars becomes wide as the observation. From these results, I conclude that the sub-clump merger in the proto-galaxy can form the galactic bulge. For the disk stars and the halo stars, the model galaxy reproduces the number of observational properties. However, the model galaxy has too much metal poor stars than the Galaxy. Higher resolution model will be required to model the precise structure and chemical properties of the Galaxy.

Contents

Chapter 1

Introduction

During the long history of astronomy, wealth of observational data has been accumulated. In coming years, much more observational data will continue to be obtained. Such high quality data include the precise proper motion of over 100 thousand stars in the Galaxy (ESA 1997), many catalogs of galaxies and clusters of galaxy (e.g., Huchra, et al. 1995; Abel, Corwin, & Olowin 1989), very detailed structures of various objects (e.g., Massey & Hunter 1998), and high quality spectra of nearby galaxies and high red-shift proto-galaxies (e.g., Dietrich et al. 1999). To advance our understanding of astrophysical problems, detailed comparisons between these observational data and theoretical predictions are required. Among many astrophysical problems, the origin of stellar systems is one of the most outstanding problems for theoretical astrophysicists. To tackle this problem, we concern about a very wide field of physics, which range from atomic reactions of gases to a large-scale structure formation by gravity. Because of these properties of this problem, many previous authors have investigated by various ways.

In particular, to understand the origin and the formation processes of our galaxy (Milky Way) is most crucial in understanding the formation of stellar systems. The reason

is that the Galaxy is the only object where we can observe various astrophysical processes such as star forming processes (e.g., Olofsson et al. 1999), dynamics of each star (ESA 1997), metallicity of each star (e.g., Edvardsson et al. 1993; Boesgaard et al. 1999), precise information about the dark matter potential (e.g., Alcock et al. 1993; Honma & Sofue 1997), and the age of the universe (e.g., Pont, Mayor & VandenBerg 1998). We can use observational facts to infer the formation process of the Galaxy as in Eggen, Lynden-Bell, & Sandage (1962) and Searle & Zinn (1978). Also, we can use these data as constraints to the theoretical predictions of our model. In this thesis, I have done the numerical simulations of the formation of the Galaxy and the galactic globular clusters. By comparing the numerical results with the various observational facts, we can understand the formation process of stellar systems. The aim of my thesis consists in following three parts.

1. Self-consistent numerical models for the formation of stellar systems

The first is to construct the self-consistent numerical models for simulating the formation of stellar systems.

We need detailed dynamical and chemical models for the Galaxy and the globular clusters to compare with the recent high quality data. Many previous numerical models lack the proper treatment of the chemical evolution (e.g., Katz 1992; Steinmetz & Müller 1995), or entirely lack the dynamical properties (i.e., one-zone chemical evolution models (e.g., Pagel 1997)). We adopt the Smoothed Particle Hydrodynamics (SPH) method to construct the self-consistent three-dimensional dynamical and chemical models for the formation of stellar systems (Chapter 2 and Appendix).

The SPH method has been widely used to calculate three-dimensional hydrodynamics with the Lagrange scheme (Lucy 1977; Gingold & Monaghan 1977). The SPH method has been applied to many astrophysical problems. Because of its Lagrangian nature, it is suitable to problems that have large density contrasts, e.g., the formation of galaxies (e.g., Evrard 1988; Hernquist & Katz 1989; Katz 1992; Steinmetz & Müller 1994), the evolution of galaxies (e.g., Friedli & Benz 1995), the cosmological simulations (e.g., Navarro & White 1994), and a cloud-cloud collision (e.g., Lattanzio et al. 1985; Habe & Ohta 1992). Various codes have been developed to combine SPH and N-body systems. In these codes, gravitational forces are calculated in many different ways such as direct summations, Particle-Particle/Particle-Mesh methods (e.g., Evrard 1988), Tree methods (e.g., Hernquist & Katz 1989; Benz et al. 1990), and the method to use the special purpose computer GRAPE (e.g., Umemura et al. 1993; Steinmetz 1996).

To simulate the formation of a stellar system from gases, we use our GRAPE-SPH code using Remote-GRAPE library (Nakasato, Mori & Nomoto 1997). In our code, the gravity is computed by the special purpose computer GRAPE to drastically accelerate

calculations. The SPH formulation that we use is the same as Navarro & White (1993). We use a spatially variable smoothing length and integrate equations of motion with a second order Runge-Kutta method as described in Navarro & White (1993) or Leap-frog method. To simulate the formation of stellar systems from gases, our GRAPE-SPH code includes various physical processes related to the formation of stellar systems. For the evolution of the metal-free cloud, we solve the rate equation of hydrogen and helium plasma to follow the formation and destruction of H_2 molecules, which is the main coolant of metal-free clouds at low temperatures. For the evolution of the metal-rich cloud, we use the metallicity dependent cooling function to solve the energy equation. We adopt the star formation recipe as used in the usual SPH codes (Katz 1992). We incorporate the effect of stellar winds and Type II and Type Ia supernovae explosion for the energy and mass feedback processes. For the Type Ia supernova model, we use the recent progenitor model of Hachisu, Kato & Nomoto (1999). In our code, we follow the chemical evolution of total metal (Z), iron (Fe) and oxygen (O) with the fixed metallicity yield. Our GRAPE-SPH code is an up-to-date SPH implementation for the formation of stellar systems.

2. Formation of globular clusters

The second aim is to simulate the formation of the globular clusters using our numerical code (Chapter 3).

The globular clusters (GC) belong to the oldest populations in our galaxy. Their formation (Elmergreen et al. 1999) is closely related to the formation process of our galaxy. The formation of a globular cluster may take place in two stages: (1) the formation of proto-globular clouds (PGC) and (2) the formation of a star cluster from the PGC. There are three scenarios for the formation of a PGC, denoted as primary, secondary, and tertiary model (Fall & Rees 1987), where the PGC forms in different stages, i.e., before, during, or

after the collapse of the galaxy, respectively.

Once the PGC forms, there might be many ways to form a globular cluster. Murray & Lin (1993) summarized the scenarios of the formation of GCs from PGCs as follows. The PGC can be divided into two types depending on their masses. The cloud, whose mass exceeds the Jeans mass, is gravitationally unstable, thus spontaneously collapsing to form stars. The cloud, whose mass is smaller than the Jeans mass, is stable until some instabilities are introduced. A cloud-cloud collision or cloud-disk collision can trigger such instabilities. When such collisions occur, the cloud would become thermally unstable owing to the efficient cooling. This cooling would lead to the formation of a very dense region, thus inducing a burst of star formation.

Though much work has been done to investigate the formation process, there is no definite theory of how the globular clusters form. Because almost all previous work about this area has been restricted to the qualitative discussion, we investigate the formation process of the globular clusters quantitatively by means of numerical calculations in this thesis. The SPH method that includes star formation processes like ours has been applied to many astrophysical problems. Such problems include the formation of isolated galaxies (Katz 1992; Steinmetz & Müller 1994), the evolution of galaxies (Friedli & Benz 1995), and the cosmological simulations (Navarro & White 1993). However, our study is the first attempt to apply this method to the globular cluster formation.

3. Formation of the Galaxy

The third is to construct high resolution numerical models for the formation and the evolution of the Galaxy (Chapter 4).

From the observational point of view, there have been two distinct scenarios for the

formation of the Galaxy. One is the "free-fall collapse" scenario proposed by Eggen, Lynden-Bell, & Sandage (1962). By evaluating the orbital motions of stars near the sun, they found a strong correlation between the orbital motion of stars (eccentricity) and the ultraviolet excess (metallicity). From these results, they have concluded that the collapse that produced the Galaxy was very rapid and occurred in nearly free-fall time scale. On the other hand, Searle & Zinn (1978) have proposed the "slow collapse" scenario. They analyzed the metallicity of the halo globular clusters and found no correlation between the metallicity of clusters and its position. Form this fact, they have concluded that the formation of the Galaxy was not the ordered collapse as proposed by Eggen, Lynden-Bell, & Sandage (1962), but the processes where small fragments continued to collapse for a longer time scale than the free-fall time scale. Recently, the galactic scale objects are thought to form by the structure formation in the cold dark matter (CDM) cosmology, which is a standard cosmological model at this time. According to the CDM scenario, larger clumps increase their masses by the progressive merger of smaller clumps. During such evolutions, the angular momentum also increases owing to the angular momentum transfer by a tidal force of surrounding clumps. At some epoch, the over-dense region is virialized to form a dark halo of a certain mass. In the CDM scenarios, the Galaxy formation occurred during the gradual formation of a dark halo. Consequently, the formation process of the Galaxy in the CDM cosmology was the midway of the above two scenarios.

After late 1980's, three-dimensional simulations of formation process of a galaxy have become possible because of more sophisticated numerical algorithms and the evolution of available computing resources. Katz (1992) has done the first three-dimensional simulation of the cosmological galaxy formation. He investigated the evolution of a spherical top hat over-dense region of a mixture of dark matter and gases with the Tree-SPH codes (Hernquist & Katz 1989). Using the star formation recipes, he modeled the formation of a spiral galaxy system, which consists of a nearly spherical dark halo and stellar and gas disk. The rotation

curves of the stellar disk in his model results in flat rotation like observed spiral galaxies. In the subsequent studies, Steinmetz & Müller (1994, 1995) investigated the disk structure with the method and initial conditions similar to Katz (1992). Their model included chemical evolution by formed stars so that they could compute the chemical properties of spiral galaxies. Their model starts with the initial number of particles of $\sim$ 8,000 for both gas and dark matter particles. The spatial resolution of the model of Steinmetz & Müller is limited by the gravitational softening length of $\sim$ 1 - 2 Kpc (Steinmetz & Müller 1995). Such small number of particles and the limited spatial resolution of a stellar component are not sufficient to resolve the detailed structure of a spiral galaxy, especially the structure of a bulge component (the size of the galactic bulge is $\sim$ 2 Kpc) and a thin disk.

In this thesis, I follow the method and the model by the previous authors but use a larger number of particles to study the detailed formation and evolution processes of the Galaxy. I evolve the spherical top hat over-dense region of a mixture of dark matter and gases with my GRAPE-SPH code. The largest model of this study uses initially over 60,000 particles. The initial masses of the gas and dark matter particles in this model are $\sim 4 \times 10^6\ M_\odot$ and $\sim 3.6 \times 10^7\ M_\odot$, respectively. The gravitational softening lengths for the gas and dark matter particles are 0.5 Kpc and 1.0 Kpc, respectively. With this numerical resolution, I can resolve the structure of a bulge ($\sim$ 2 Kpc) in reasonable accuracy. In the previous studies by Katz (1992) and Steinmetz & Müller (1994, 1995), mainly the various structural properties are concerned. In this thesis, I compare the chemical properties of stars with the observational facts of the Galaxy. For this purpose, the chemical evolution of total metal (Z), iron (Fe) and oxygen (O) is incorporated in the GRAPE-SPH code. Using own GRAPE-SPH code, I can compare the dynamical and chemical properties of the numerical models with the observational facts of the Galaxy. If the model reproduce a number of the observational facts, the numerical results predict various formation and evolution history of the Galaxy

4. Summary

In this thesis, I describe our numerical code for the formation of stellar systems and investigate the formation of globular clusters and the Galaxy using my numerical code. I adopt the SPH method to model the formation of stellar systems. This GRAPE-SPH code includes various physical processes associated with the formation of stellar systems. In particular, the chemical evolution model in the code is constructed in a self-consistent manner. By using such a state-of-the-art numerical model, I investigate the globular cluster formation and the formation of the Galaxy. These two topics are closely related since the globular clusters might form during the formation of the Galaxy. Thus, I will infer the formation of the Galaxy including the globular cluster formation by combining the numerical results for each system (Chapter 5).

Chapter 2

SPH method and including physical processes

The Smoothed Particle Hydrodynamics (SPH) method has been widely used to calculate three-dimensional hydrodynamics with the Lagrange scheme (Lucy 1977; Gingold & Monaghan 1977). The SPH method has been applied to many astrophysical problems. Because of its Lagrangian nature, it is suitable to the problem that has large density contrasts, e.g., the formation of galaxies (e.g., Evrard 1988; Hernquist & Katz 1989; Katz 1992; Steinmetz & Müller 1994), the evolution of galaxies (e.g., Friedli & Benz 1995), the cosmological simulations (e.g., Navarro & White 1994), and a cloud-cloud collision (e.g., Lattanzio et al. 1985; Habe & Ohta 1992). Various codes have been developed to combine SPH and N-body systems. In these codes, gravitational forces are calculated in many different ways such as direct summations, Particle-Particle/Particle-Mesh methods (e.g., Evrard 1988), Tree methods (e.g., Hernquist & Katz 1989; Benz et al. 1990), and the method to use the special purpose computer GRAPE (e.g., Umemura et al. 1993; Steinmetz 1996).

A GRAPE (GRAvity PipE) is a special purpose computer to calculate gravitational force and potential efficiently (Sugimoto et al. 1990). We need a host computer, which is connected to GRAPE board, to control it and conduct other calculations (e.g., time integration). The use of GRAPE for SPH simulations (hereafter GRAPE-SPH) has many advantages. The reason is that the GRAPE can calculate not only gravitational force and potential but also construct lists of neighbor particles in a short time. In SPH simulations, we need the lists of neighbor particles to calculate hydrodynamical quantities. Searching neighbor particles with GRAPE is much more efficient than a direct search on the host computer. With GRAPE-SPH code, therefore, we need to calculate only pure hydrodynamical part of SPH on the host computer.

Although the cost of N-body part of SPH can be significantly reduced by using GRAPE, the speed of the hydrodynamical part of the code is limited by the speed of the host computer. The speed of a workstation (WS) is being rapidly improved. To take full advantage of GRAPE for SPH calculations, we have to use the state-of-the-art WS as a host. If the host WS of GRAPE is much slower than a fast WS available now, the total performance of GRAPE-SPH is lower than that of the SPH simulation on the fast WS without GRAPE. Of course, by developing new interface to new WS, we could solve this problem. This approach, however, requires much human time. Moreover, during the development of the new interface, an ever newer WS with different interface might become available.

We take a different, novel approach to solve this problem. We use the Parallel Virtual Machine (Geist et al. 1994), which is a most popular message-passing systems in parallel computing, to connect the WS that is directly connected to a GRAPE board with another fast machine. The SPH part can be performed on the fast machine. In fact, all simulation code except the N-body part is run on the fast machine and the WS connected to GRAPE

board serves essentially as the intelligent communication interface. Figure 1 and 2 shows the present GRAPE system and our new approach, respectively. In our new approach, the combinations of the WS and GRAPE behave as the "remote GRAPE" system that is connected directly to the Local Area Network (LAN). Thus, any computer on the LAN can be used as the host (remote-host) of the GRAPE. We construct the library named Remote-GRAPE. The description and performance analysis of Remote-GRAPE are presented in Appendix.

To simulate the formation of stellar systems from gases, we have implemented the GRAPE-SPH code using Remote-GRAPE library. Our GRAPE-SPH code includes various physical processes, e.g., radiative cooling, star formation, and feedback from formed stars. Though there are many different implementations of the SPH method (a recent comparison of various SPH implementations is found in Thacker et al. 1998), the SPH formulation that we use is the same as Navarro & White (1993). We use a spatially variable smoothing length and integrate equations of motion with a second order Runge-Kutta method as described in Navarro & White (1993) or Leap-frog method. In the following sections, details of the implementation of our SPH code are described.

1. Basic equations

The basic equations of hydrodynamics are as follows:

$$\frac{D\rho}{Dt} + \rho\nabla\cdot\boldsymbol{v} = 0, \tag{2.1}$$

$$\frac{D\boldsymbol{v}}{Dt} + \frac{\nabla P}{\rho} = -\nabla\Phi, \tag{2.2}$$

$$\frac{Du}{Dt} - \frac{P}{\rho^2}\frac{D\rho}{Dt} = \frac{\nabla\cdot(\kappa\nabla T)}{\rho} + \Gamma - \frac{\rho}{\mu^2}\Lambda, \tag{2.3}$$

and

$$\nabla^2\Phi = 4\pi G\rho, \tag{2.4}$$

where $\frac{D}{Dt}$ is the Lagrange derivative. The first equation is the continuity equation, where ρ is the mass density and $\boldsymbol{v}$ is the velocity of fluid. The second equation represents the conservation of momentum, where P is the pressure and Φ is the potential of fluid. The third equation is the thermal energy equation, where u is the thermal energy per unit mass, κ is the coefficient of thermal conductivity, Γ is the heating function, Λ is the cooling function, and μ is the mean molecular mass. The fourth equation is the Poisson's equation, where G is the gravitational constant. We also need the equation of state that relates P, ρ, and u.

2. SPH method

In SPH, physical quantities at one position are calculated by smoothly averaging over neighbor particles. A smoothly averaged value of a physical quantity $f(\boldsymbol{r})$ is given by

$$< f(\boldsymbol{r}) >= \int f(\boldsymbol{r}')W(\boldsymbol{r}-\boldsymbol{r}';h)d\boldsymbol{r}', \tag{2.5}$$

where $W(\boldsymbol{r};h)$ is the kernel function, and h is the smoothing length that specifies the size of the kernel. The derivative of $f(\boldsymbol{r})$ is estimated as

$$< \nabla f(\boldsymbol{r}) >= \int f(\boldsymbol{r}')\nabla W(\boldsymbol{r}-\boldsymbol{r}';h)d\boldsymbol{r}'. \tag{2.6}$$

We treat continuous fluid as an assembly of discrete particles in SPH. Thus, we replace the integral in equation (2.5) with a summation over the particles and the volume element with $m/\rho(\boldsymbol{r})$, where m is the mass of the particles and $\rho(\boldsymbol{r})$ is the density. As a result, Eq. (2.5) is represented in the SPH form as

$$< f(\boldsymbol{r}) >= \sum \frac{m_j}{\rho(\boldsymbol{r}_j)} f(\boldsymbol{r}_j)W(\boldsymbol{r}-\boldsymbol{r}_j;h). \tag{2.7}$$

The momentum equation (2.2) is represented in the SPH form as

$$\frac{D\boldsymbol{v}_i}{Dt} = -\sum m_j\left(\frac{P_i}{\rho_i^2} + \frac{P_j}{\rho_j^2}\right)\nabla W(\boldsymbol{r}_i-\boldsymbol{r}_j;h) - (\nabla\Phi)_i. \tag{2.8}$$

Also using Eq. (2.1), Eq. (2.3) is represented as

$$\frac{Du_i}{Dt} = \frac{1}{2}\sum m_j(\frac{P_i}{\rho_i^2} + \frac{P_j}{\rho_j^2})(\boldsymbol{v}_i - \boldsymbol{v}_j)\nabla W(\boldsymbol{r}_i - \boldsymbol{r}_j; h) + \Gamma - \frac{\rho}{\mu^2}\Lambda \tag{2.9}$$

(we neglect the thermal conduction in the present study). The density is determined from

$$\rho_i = \sum m_j W(\boldsymbol{r}_i - \boldsymbol{r}_j; h), \tag{2.10}$$

instead of using continuity equation (2.1). The form of $W(\boldsymbol{r}_i; h)$ is arbitrary as long as it is diferentialble to a sufficient order and falls rapidly for $r > h$. We adopt the spline kernel (Monaghan & Lattanzio 1985), which is used in most SPH calculations as

$$W(q,h) = \frac{1}{\pi h^3}\left\{\begin{array}{cc} 1 - \frac{3}{2}q^2 + \frac{3}{4}q^3, & (0 \le q \le 1) \\ \frac{1}{4}(2-q)^2, & (1 \le q \le 2), \\ 0, & otherwise \end{array}\right\} \tag{2.11}$$

where q is defined as $q = r/h$. This spline kernel is zero outside $r = 2h$, so the summation in the above SPH equations is calculated over neighbor particles inside $2h$. In our SPH code, the neighbor search is done by the Tree methods (see Appendix).

We use the smoothing length that can vary spatially and evolve with a time as follows. For each time step, we compute the smoothing length for each particle with a following equation as,

$$h_{\rm new} = 0.5 h_{\rm old}\left[1.0 + \left(\frac{N_{\rm nb}}{N_{\rm old}}\right)^{\frac{1}{3}}\right], \tag{2.12}$$

where $N_{\rm nb}$ is the user specified number of neighbor particles and $N_{\rm old}$ is the number of neighbor particles in a previous time step. In the present paper, we set $N_{\rm nb} = 50$ - 100. To conserve the momentum in solving equation of motions, we have to use symmetrized smoothing length in computing a kernel estimate as

$$h_{ij} = \frac{1}{2}(h_i + h_j). \tag{2.13}$$

We note that there are other methods to symmetrized the kernel estimate (Hernquist & Katz 1989).

We add an artificial viscous term to Eqs. (2.8) and (2.9). The standard formulation of artificial viscosity term is following:

$$Q_{ij} = \left\{\begin{array}{cc} \frac{-\alpha c_{ij}\mu_{ij} + \beta\mu_{ij}^2}{\rho_{ij}}, & {\rm for}(\boldsymbol{v}_i - \boldsymbol{v}_j)\cdot(\boldsymbol{r}_i - \boldsymbol{r}_j) \le 0 \\ 0, & {\rm otherwise}, \end{array}\right\} \tag{2.14}$$

$$\mu_{ij} = \frac{h(\boldsymbol{v}_i - \boldsymbol{v}_j)\cdot(\boldsymbol{r}_i - \boldsymbol{r}_j)}{(\boldsymbol{r}_i - \boldsymbol{r}_j)^2 + (0.1h)^2}, \tag{2.15}$$

where c_{ij} and ρ_{ij} are the arithmetic means of the sound velocity and density, respectively (Monaghan 1992). α and β are the parameters to control the effectiveness of viscosity term, and we set $\alpha = 1.0$ and $\beta = 2.0$ in the present paper. This from of an artificial viscosity term cause the viscous angular momentum transport. Following Navarro & Steinmetz (1997), we use a shear free viscosity formulation as

$$Q'_{ij} = Q_{ij}\frac{f_i + f_j}{2} \tag{2.16}$$

$$f_i = \frac{|\nabla\cdot\boldsymbol{v}_i|}{|\nabla\cdot\boldsymbol{v}_i| + |\nabla\times\boldsymbol{v}_i| + 0.0001c_i/h_i}. \tag{2.17}$$

In the present paper, we use equation of state for ideal gas with $\gamma = 5/3$ as

$$P = (\gamma - 1)\rho u. \tag{2.18}$$

3. Solving equations of motions

In our SPH code, we can treat three types of different particle, i.e., gas, dark and star particles. The gravity between these particles is computed by the special purpose computer GRAPE. The gas particles interact with other particles only by gravity. We use two types

of the GRAPE system: GRAPE-3AF and GRAPE-4. In using GRAPE-3AF, we use the Remote-GRAPE library, which we have developed to speed up calculations.

The time step of each particle is determined from a following equation;

$$\Delta t = \eta \min\left(\left(\frac{\eta\epsilon}{|v|}\right), \left(\frac{\epsilon}{|a|}\right)^{\frac{1}{2}}\right), \tag{2.19}$$

where η is the numerical parameter, ϵ is the gravitational softening length, $|v|$ and $|a|$ are the absolute value of the velocity and the acceleration, respectively. We set $\eta = 0.5$ in the preset study. For gas particles, an additional constraint (the Courant condition) is used besides above equations as

$$\Delta t_{\rm gas} = \frac{C_{\rm courant} h}{h|\nabla \cdot \boldsymbol{v}| + c + 1.2(\alpha c + \beta \max(|\mu_{ij}|))}, \tag{2.20}$$

where $\max(|\mu_{ij}|)$ means that the maximum absolute value of the equations (2.15) over neighbor particles. $C_{\rm courant}$ is the Courant number and we set $C_{\rm courant} = 0.3$ - 0.5 in the preset study.

In the formation processes of a stellar system, the large density contrasts are developed as the system evolves. This means that the time scale of evolution in different places differs very much. Thus, we have to use an individual time step scheme to make calculations more efficient, especially when the number of particles is large. For the individual time step scheme, we follow the scheme of Navarro & White (1993). First we compute the time step (Δt_e) determined by equations (2.19) (and (2.20) for gas particles). Then we make the actual time step (Δt_a) a greatest power of 2 subdivision, which is smaller than Δt_e, of the system-time-step ($\Delta t_{\rm sys}$), i.e., $\Delta t_a = \Delta t_{\rm sys}/2^n \leq \Delta t_e$. The system-time-step is the fundamental time step to synchronize all particles.

The time integration of equations of motions is done by the Leap-frog method that is modified for the individual time step scheme or the second order Runge-Kutta method that

is described in Navarro & White (1993). Both methods are second order accurate in a space and a time.

4. Physical processes

To simulate the formation of stellar systems from gases, we have to consider various physical processes: radiative cooling, star formation, and feedback from formed stars. In this section, we describe the implementation of such physical processes in our SPH code.

4.1. Radiative cooling

The radiative cooling rates depend on the temperature and ionization states of the gas. Also, the chemical composition of the gas affects the cooling rate. We perform SPH simulations for the following three cases (A, B, C) of gases.

Case A: We assume that the chemical composition of the gases is primordial with no heavy elements and the gas is in ionization equilibrium. In this case, our treatment of radiative cooling is the same as adopted by Katz, Weinberg & Hernquist (1996); they computed the cooling rate using the two-body processes of H and He, and free-free emissions. The cooling function ($\Lambda(T)$) is shown in Figure 4 with the solid line. In this case, the cooling rate decreases very rapidly as the temperature T decreases below 2×10^4 K so that the gas would not radiatively cool below $T \sim 10^4$ K.

Case B: We assume that the gases includes some heavy elements and is in ionization equilibrium. In this case, we use the cooling function with different chemical composition that is computed by MAPPINGS III software by R.S. Sutherland (MAPPINGS III is the successor of MAPPINGS II that is described in Sutherland & Dopita (1993)). We compute

the cooling function of the ionization equilibrium gas for [Fe/H] $= -5.0$ - 0.0 with the solar abundance ratio (see Table 4 of Sutherland & Dopita (1993)) and present the results in Figure 4 with the dashed lines (each line corresponds to [Fe/H] $= -1, -2, -3$ respectively from the top to the bottom). Existence of heavy elements significantly enhances the cooling rates. At $T < 10^4$ K, the cooling due to the forbidden line emission of carbon and oxygen is efficient. For [Fe/H] $= 0$, the cooling rates around $T \sim 10^5$K are 100 times larger than the cooling rates of primordial hydrogen and helium gas. These differences would make the evolution of the gas very different.

Case C: We concern about the non-equilibrium cooling. If the gas cools from high temperatures, ionization equilibrium is not realized. Figure 3 shows the ratio between the recombination time ($t_{\rm recom}$) of hydrogen and the cooling time ($t_{\rm cool}$) of the primordial gases in ionization equilibrium; $t_{\rm recom}/t_{\rm cool}$. The $t_{\rm recom}$ and $t_{\rm cool}$ are defined as

$$t_{\rm recom} = \frac{1.0}{\alpha(T) f_e(T)} \tag{2.21}$$

and

$$t_{\rm cool} = \frac{3 k_b T}{2\Lambda(T)}, \tag{2.22}$$

where the α is the recombination coefficient of hydrogen and electron, f_e is the fraction of free electrons, and k_b is the Bolzman constant. For α, we use the value of Spitzer (1978). Clearly, the cooling time is much shorter than the recombination time for $T \sim 2 \times 10^4$ K, so that ionization equilibrium is not realized when the gas cools from high temperatures. In the non-equilibrium case, the existence of electrons and ionized hydrogen at $T < 10^4$ K makes it possible to form H_2 molecules through the creation of intermediaries H^- and H_2^+ as:

$$\begin{aligned} H + e &\rightarrow H^- + \text{photon} \\ H + H^- &\rightarrow H_2 + e \end{aligned} \tag{2.23}$$

and

$$\begin{aligned} H + H^+ &\rightarrow H_2^+ + \text{photon} \\ H_2^+ + H &\rightarrow H_2 + H^+ \end{aligned} \tag{2.24}$$

(Shapiro & Kang 1987). These H_2 molecules cause further cooling down to $T \sim 10^2$ K owing to the rotational-vibrational line excitation.

To include the effect of such molecular cooling, we have to solve rate equations that determine the ionization states of H and He atoms, and the formation and destruction of H_2 molecules. In our case, the typical time step in solving the rate equations is shorter than the dynamical time step, which is determined mainly by the Courant condition. Integrating all equations with a shorter timestep than the dynamical time is very costed work. So we divide the dynamical timestep with dynamical variables (density etc.) being constant in solving the energy and rate equations, which is similar to the method adopted in Shapiro & Kang (1987). The rate-coefficients are also the same as used in Shapiro & Kang (1987). Included species are H^0, H^+, He^0, He^+, He^{++}, H^-, H_2^+, H_2, H_2^* and e, where H_2^* is the exited hydrogen molecule. In our SPH code, we solve the rate equations for 10 species in each SPH particle with a reasonable computing time. Solving the rate equations for the gas including heavy elements (over 200 species) is not feasible with a current resource so that we only concern the hydrogen and helium plasma in the present paper.

The cooling function for the non-equilibrium case is presented in Figure 4 with the dotted line. In computing these cooling rates, we follow the isobaric temperature evolution of the fully ionized gas. Initially, the temperature and hydrogen number density of the gas are 10^7 K and 0.01 cm^{-3}, respectively. We assume optically thin plasmas so that the gas cools rapidly. Around $T \sim 2 \times 10^4$ K, H_2 molecules begin to form. At $T < 10^4$ K, the cooling rate due to H_2 molecules is comparable to the cooling rate for [Fe/H] $= -1.0$ gas.

Finally, we summarize the treatment of the cooling rates in our SPH code. We can

perform SPH simulations for these three cases A, B and C. In chapter 3, we will study the evolution of a PGC with two different initial chemical compositions, i.e., a metal-free gas cloud and a metal-rich gas cloud. In the former case, we solve the energy and rate equations simultaneously for each SPH particle (case C) if the gas temperature is lower than 3×10^4 K and the gas particle is not in the heating phase (see section 4.3). If these conditions are not met, we use the pre-computed cooling table for the ionization equilibrium case (case A). In the latter case, we use the pre-computed cooling table to solve the energy equations (case B). In chapter 4, we will follow the evolution of a proto-galactic cloud, which has initially no heavy element, with Case A and B.

4.2. Star formation

Our treatment of star formation is the same as adopted by Katz (1992). Hereafter, "STAR" means "star particle", which is not an individual star but an association of many stars. A STAR forms in the region where the flow is converging, cooling, and Jeans unstable. These conditions are expressed as

$$(\nabla \cdot \boldsymbol{v})_i < 0, \tag{2.25}$$

$$t_{\rm cool} < t_{\rm d}, \tag{2.26}$$

$$t_{\rm d} < t_{\rm sound}. \tag{2.27}$$

Here $t_{\rm cool}$, $t_{\rm d}$, and $t_{\rm sound}$ are the cooling time, dynamical time, and sound crossing time, respectively, and expressed as

$$t_{\rm cool} = \frac{\mu^2 u}{\rho \Lambda}, \tag{2.28}$$

$$t_{\rm d} = \frac{1}{\sqrt{4\pi G \rho}}, \tag{2.29}$$

$$t_{\rm sound} = \frac{h_i}{c_s}, \tag{2.30}$$

where μ is the mean molecular weight, u is the specific thermal energy, and c_s is the local sound speed. A STAR forms in the region where these all three conditions are satisfied.

The star formation rate is given as

$$\frac{D\rho_*}{Dt} = -\frac{\rho}{t_{\rm starform}} = -C\sqrt{4\pi G}\rho^{\frac{3}{2}}, \tag{2.31}$$

where ρ_* is the density of a star, and $t_{\rm starform} = t_{\rm d}/C$ with a star formation parameter C. The last term of equation (2.31) is similar to the Schmidt's law (Schmidt 1959). Integrating equation (2.31) over one time step δt and making calculations with the equations for SPH, we obtain the mass of a newly formed star in δt as

$$m_{\rm star} = \left[1 - \frac{1}{1 + 0.5\frac{\delta t}{t_{\rm starform}}}\right] \pi h_i^3 \rho_i. \tag{2.32}$$

The newly formed STAR is then treated as a collision-less particle. There are some modifications to the above algorithm in the simulation of formation of a galaxy and we will explain those things in chapter 4.

4.3. Feedback from stars

The formed stars eject gases and heavy elements in stellar winds and supernova explosions and heats up, accelerate, and enrich circumstellar and interstellar medium. High energy explosions like a supernova produce high temperature and low density regions in interstellar medium. In the SPH method, the numerical accuracy for high density regions is much better than mesh based methods but the accuracy for low density regions are poorer. In a typical resolution of usual SPH simulations such as Navarro & White (1993), the numerical resolution (100 - 1000 pc) is larger than a typical size of supernova remnants (< 100 pc). Thus, it is difficult to properly include the energy, momentum, and mass release from stars in the SPH method because of the nature of the SPH method and the poor

resolutions in current computing resources. We must use some approximations to mimic real feedback processes in the SPH method.

One of the method has been proposed by Navarro & White (1993). In their method, the energy produced by a supernova explosion is distributed to neighbor gas particles of each STAR mostly as a thermal energy and the rest is distributed as a velocity perturbation to the gas particles; the fraction of the energy in a kinetic form is a free parameter. We note that Leitherer, Robert, & Drissen (1992) presented the population synthesis model of stellar feedback processes. In the present paper, we distribute the energy to neighbor particles in a pure thermal form as a zero-th order approximation.

4.3.1. Energy ejection

The energy ejection rate per STAR is given as

$$E_{\rm eject} = e_{\rm SW} R_{\rm SW} + e_{\rm SNII} R_{\rm SNII} + e_{\rm SNIa} R_{\rm SNIa}, \tag{2.33}$$

where $e_{\rm SW}$ is the total ejected energy by stellar winds during the stellar life time and $e_{\rm SNII}$ and $e_{\rm SNIa}$ are the energy ejected by one Type II and Ia supernovae explosion, respectively. The R_{SW} is the number of stars per unit time expelling their envelopes at the current epoch and $R_{\rm SNII}$ and $R_{\rm SNIa}$ are the rate of Type II and Type Ia supernovae, respectively. We define the R_{SW} and R_{SNII} as follows

$$R_{\rm SW} = \frac{\int_{M_{\rm ms}}^{M_{\rm up}} \phi(m) dm}{\tau(M_{\rm ms})} \tag{2.34}$$

$$R_{\rm SNII} = \frac{\int_{M_{\rm ms}}^{M_{\rm ma}} \phi(m) dm}{\tau(M_{\rm ms}) - \tau(M_{\rm ma})}, \tag{2.35}$$

where $\phi(m)$ is the initial mass function (IMF), namely $\phi(m)dm$ gives the number of stars in the mass range of $(m, m+dm)$ and the $\tau(m)$ is the stellar lifetime as a function of stellar

mass (David, Forman & Jones 1990). In the present study, we assume the power-low type IMF as

$$\phi(m) = A m^{-2.35}, \tag{2.36}$$

where the A is the constant. For the upper and lower limit masses in the IMF, $M_{\rm up} = 120$ and $M_{\rm lo} = 0.05$ $M_\odot$ are assumed. In Eqs. (2.34) and (2.35), $M_{\rm ma}$ (= 50.0 $M_\odot$) and $M_{\rm ms}$ (= 8.0 $M_\odot$) are the upper and lower limit masses of the stars that explode as Type II supernovae.

For the Type Ia supernovae rates, we follow the chemical evolution model of galaxies by Kobayashi et al. (1998). They adopt the single-degenerate scenario (Nomoto et al. 1994) for the progenitor model of Type Ia supernovae. In their mode, the Type Ia supernovae rates at some epoch t is written as

$$R_{\rm SNIa}(t) = C_{\rm SNIa} \frac{\int_{M(t)}^{M(t+\Delta t)} \phi(m) dm}{\Delta t}, \tag{2.37}$$

where the $M(t)$ is the mass of the star which has the life time of t (namely $M(t) = \tau^{-1}(m)$) and $C_{\rm SNIa}$ is the constant to be calibrated by the observational constraints. From the result of the evolution of the progenitor model by Hachisu, Kato & Nomoto (1996, 1999), the mass ranges of the secondary stars that explode as Type Ia supernovae are

$$M_{\rm sec} = [1.8, 2.6], \quad [0.9, 1.5] \quad M_\odot. \tag{2.38}$$

We note that these mass ranges weakly depend on the metallicity of the star. We only compute $R_{\rm SNIa}$ for these mass ranges and set $R_{\rm SNIa} = 0$ for other mass ranges. Figure 5 shows $R_{\rm SNIa}$ as a function of time (in this plot we set $C_{\rm SNIa} = 1.0$). In the present paper, we set $C_{\rm SNIa} = 4.0 \times 10^{-4}$ from the result of the test calculations. We note that the other authors (Carraro, Lia & Chiosi 1998; Raiteri, Villata, & Navarro 1996) adopt the different progenitor model such as Greggio & Renzini (1983) and Matteucci & Greggio (1986).

For the supernova energy, we assume that $e_{\rm SNII} = e_{\rm SNIa} = 10^{51}$ erg. For the stellar wind energy, $e_{\rm SW}$ is estimated to be 0.2×10^{51} erg for solar metallicity stars from the observational data of OB associations (Abbot 1982). The Chemical abundance of a massive star significantly affects $e_{\rm SW}$ (Leitherer, Robert, & Drissen 1992), so that we use metallicity dependent $e_{\rm SW}$ as $e_{\rm SW} = 0.2e_{\rm SNII}(Z/Z_\odot)^{0.8}$, where Z is the mass fraction of heavy metals in the STAR.

4.3.2. Mass ejection

In our code, the mass ejection due to star stellar winds of massive stars ($m \geq M_{\rm ms}$) is combined with the mass ejection due to Type II supernova. The mass ejection due to stellar winds of the main sequence stars ($m < M_{\rm ms}$) is treated separately. Thus, the mass ejection rate per STAR is written as

$$M_{\rm eject} = m_{\rm SNII}R_{\rm SNII} + m_{\rm SWm}R_{\rm SWm} + m_{\rm SNIa}R_{\rm SNIa}, \tag{2.39}$$

where $m_{\rm SNII}$ is the average mass that explodes as a Type II supernovae, and $m_{\rm SWm}$ is the average mass that is ejected by stellar winds of the main sequence stars, and $m_{\rm SNIa}$ is the mass that explode as a Type Ia supernovae. The $R_{\rm SWm}$ is the number of stars per unit time expelling their envelopes at the current epoch. The $m_{\rm SNII}$ and $m_{\rm SWm}$ are defined as

$$m_{\rm SNII} = \frac{\int_{M_{\rm ms}}^{M_{\rm ma}} m\phi(m)dm}{\int_{M_{\rm ms}}^{M_{\rm ma}} \phi(m)dm} - m_{\rm NS}, \tag{2.40}$$

$$m_{\rm SWm} = \frac{\int_{M_{\rm ll}}^{M_{\rm ms}} m\phi(m)dm}{\int_{M_{\rm ms}}^{M_{\rm ll}} \phi(m)dm} - m_{\rm WD}. \tag{2.41}$$

Here $m_{\rm NS}$ is the mass that is locked up in the neutron star and $m_{\rm WD}$ is the mass that is locked up in the white dwarf star. The $M_{\rm ll}$ ($= 1.0\ {\rm M}_\odot$) is the mass of the star, the life time

of which almost equals to the Hubble time. We assume that $m_{\rm NS} = 1.4$ and $m_{\rm WD} = 1.0\ {\rm M}_\odot$. In the present paper, we assume that Type Ia supernova is produced by the Chandrasekhar mass white dwarf so that $m_{\rm SNIa}$ is $1.4\ {\rm M}_\odot$. We define the $R_{\rm SWm}$ as follows

$$R_{\rm SWm} = \frac{\int_{M_{\rm ll}}^{M_{\rm ms}} \phi(m)dm}{\tau(M_{\rm ll}) - \tau(M_{\rm ms})}, \tag{2.42}$$

The fraction of heavy metal in $m_{\rm SNII}$ and $m_{\rm SNIa}$ is computed using the nucleosynthesis yield of Type II and Ia supernovae (Tsujimoto et al. 1996; Nomoto et al. 1997). We compute the chemical evolution of total metal (Z), iron (Fe) and oxygen (O) in our code. The used metallicity yield is tabulated in Table 1.

With the present algorithm and the adopted parameters, single star burst of 10^8 $M_\odot$ will produce $\sim 5.5\times10^5$ Type II supernovae explosions and $\sim 1.4\times10^5$ Type Ia supernovae explosions and eject $\sim 2.2\times10^7$ $M_\odot$ gases after the 15 Gyr evolution. The ejected gases contain $\sim 1.6\times10^6$ $M_\odot$ of heavy elements, which include $\sim 1.5\times10^5$ $M_\odot$ of iron and $\sim 1.0\times10^6$ $M_\odot$ of oxygen.

4.3.3. Summary

The feedback phase is divided into three phases: a stellar wind phase, a Type II supernova phase, and a Type Ia supernova phase. The stellar wind phase continues for $\tau(M_{\rm ma})$, during which only the energy ejection from STARs is included; the ejected mass is included in the Type II supernovae phase for simplicity. The Type II supernova phase begins at $t = \tau(M_{\rm ma})$ and ends at $t = \tau(M_{\rm ms})$. During the Type II supernova phase, the mass ejection is the sum of the contributions by the stellar winds of massive stars and Type II supernovae. The Type Ia supernova phase begins at $t = \tau(M_{\rm ms})$. During the Type Ia supernova phase, the energy ejection and mass ejection are the sum of the contributions by the the Type Ia supernovae and the stellar winds of main sequence stars. We present the

schematic view of the feedback processes in Figure 6.

The thermal energies, gases, and heavy elements from stellar winds and supernovae are smoothed over neighbor particles of the STAR within a neighbor radius of R_f (feedback radius). Such neighbor particles are called "in heating phase".

5. Test calculations

5.1. Shock tube problem

A standard test calculation for the hydrodynamics code is the Sod's shock tube problem (Sod 1978; Hernquist & Katz 1989). This is a one-dimensional test problem that has an analytic solution. The initial condition of the problem is following as (Monaghan & Gingold 1983):

$$\begin{array}{llll} \rho = 1.0 & P = 1.0 & v = 0.0 & \mathrm{x} < 0.5, \\ \rho = 0.25 & P = 0.1795 & v = 0.0 & \mathrm{x} \geq 0.5. \end{array} \tag{2.43}$$

Initially, we distribute 400 particles in the range $-0.5 \leq x \leq 1.5$. The particles are distributed in equally spaced manner so that the mass of the particles is $\rho \times (2.0/400)$, i.e., 5.0×10^{-3} in $x < 0.5$ and 8.975×10^{-4} in $x \geq 0.5$, respectively. Actually, the particles in the range $x < 0.0$ and $x > 1.0$ are the boundary particles that are not evolved along with time. When we solve this test problem, we set $\gamma = 1.4$. Figure 7 shows the result of the test problem. The solid line is the analytic solution and dots represent the numerical results. Although there are post-shock oscillations, our numerical results are almost consistent with the analytic solution as Hernquist & Katz (1989). The results presented in Figure 7 are obtained with the scheme that the times step of all particles are equal. If we use the individual time step scheme, the results are not changed.

5.2. Adiabatic collapse

A test calculation for the SPH code including self gravity is the adiabatic collapse (Evrard 1988; Hernquist & Katz 1989). This is a three-dimensional test problem of a collapse of an isothermal gas sphere.

Initially, the gas sphere of radius R and total mass M has a density profile as:

$$\rho(r) = \frac{M}{2\pi R^2} \frac{1}{r}. \tag{2.44}$$

The sphere is isothermal with specific thermal energy $u = 0.05GM/R$. When we solve this test problem, we set $\gamma = 5/3$ and the unit of the calculations are such that $G = M = R = 1.0$. Also, we set the gravitational softening length $\epsilon = 0.1$ and the desired number of neighbor particles $N_{\mathrm{nb}} = 50$. The number of particles used in the calculations is 5,000. Figure 8 shows the evolution of total (solid liens), and other energies. The total energies is conserved within ~ 1 %. At the first stage of the evolutions, the gas sphere collapse. At $t \sim 1.1$, the sphere become the maximum compression and expand after that time. After $t = 2$, the sphere is nearly equilibrium state so that we terminate the calculations. During the evolution, the total angular momentum is also conserved within ~ 1 %. The results presented here are obtained with the individual time step scheme as Hernquist & Katz (1989). Our SPH code reproduces almost same results with their results.

6. Summary

In this chapter, we describe the details of the implementation of our GRAPE-SPH code. In our code, the gravity is computed by the special purpose computer GRAPE to drastically accelerate calculations. The SPH formulation that we use is the same as Navarro & White (1993). We use a spatially variable smoothing length and integrate equations of motion with a second order Runge-Kutta method as described in Navarro & White

(1993) or Leap-frog method. To simulate the formation of stellar systems from gases, our GRAPE-SPH code includes various physical processes associated with the formation of stellar systems. For the evolution of the metal-free cloud, we solve the rate equation of hydrogen and helium plasma to follow the formation and destruction of H_2 molecules (Case C), which is the main coolant of metal-free cloud at low temperature. For the evolution of the metal-rich cloud, we use the metallicity dependent cooling function to solve the energy equation (Case B). We adopt the star formation recipe as used in the usual SPH codes. For the energy and mass feedback processes by stars, we incorporates the effect of stellar winds, Type II supernovae, and Type Ia supernovae for the energy and mass feedback processes. For the Type Ia supernovae model, we use the recent progenitor model of Hachisu, Kato & Nomoto (1999). In our code, we follow the chemical evolution of total metal (Z), iron (Fe) and oxygen (O) with fixed metallicity yield. Our GRAPE-SPH code is a up-to-date SPH implementation for the formation of stellar systems.

Table 1. The heavy metal yield used in our code

	M[a]	Z	Fe	O
Type II SNe	14.0 $M_\odot$	2.54 $M_\odot$	9.07×10^{-2} $M_\odot$	1.80 $M_\odot$
Type Ia SNe	1.4 $M_\odot$	1.4 $M_\odot$	7.43×10^{-1} $M_\odot$	1.43×10^{-1} $M_\odot$

Note. — These data from Tsujimoto et al. (1996); Nomoto et al. (1997).

[a]The total ejected mass per 1 supernova explosion.

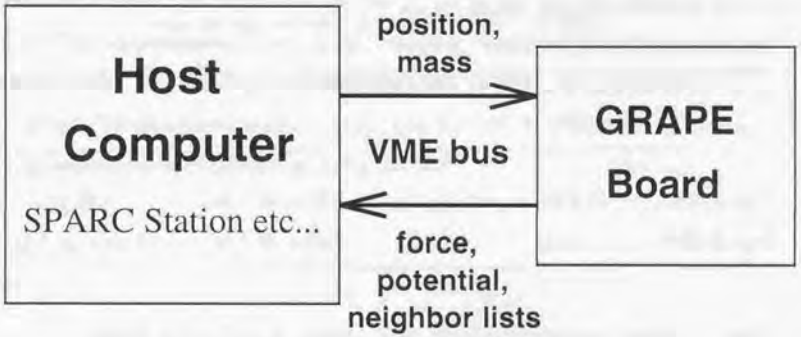

Fig. 1.— The schematic diagram of the GRAPE system.

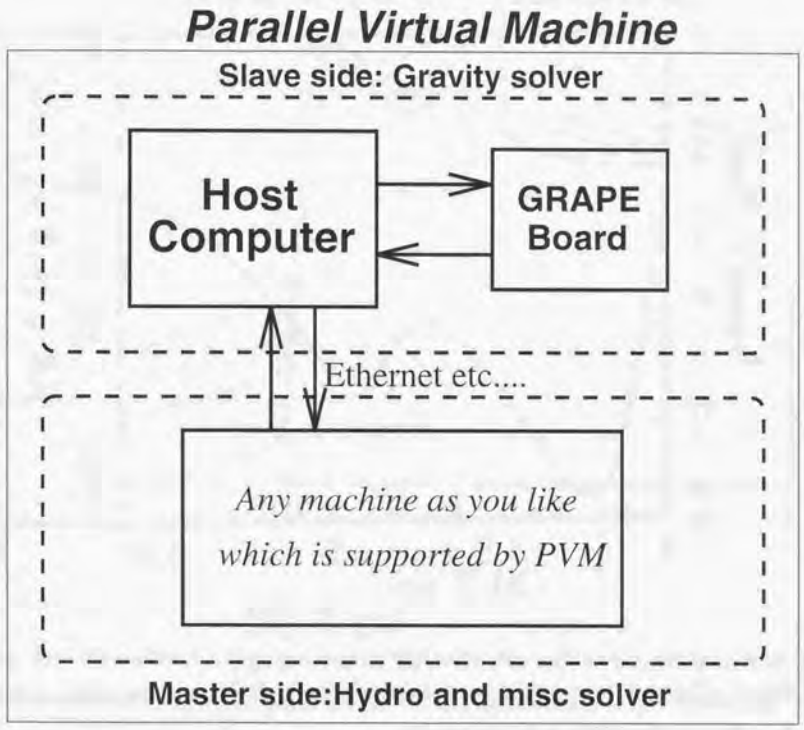

Fig. 2.— The schematic diagram of the Remote-GRAPE system.

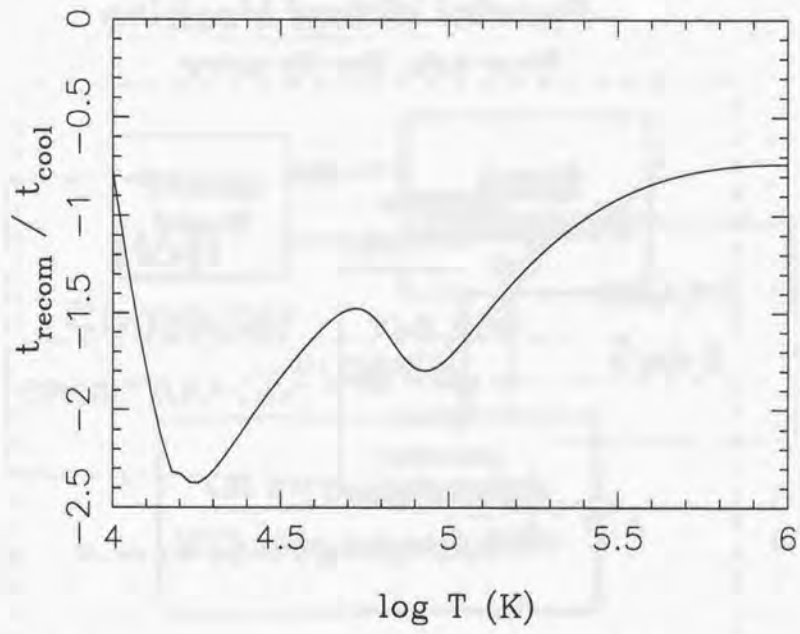

Fig. 3.— The ratio between the recombination time of hydrogen and the cooling time (i.e., $t_{\rm recom}/t_{\rm cool}$) as a function of the temperature.

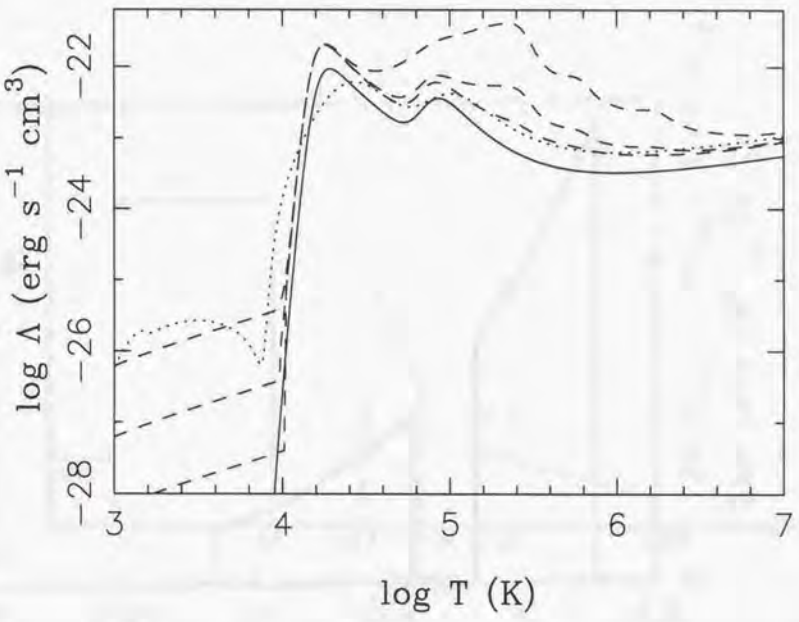

Fig. 4.— The various cooling rates used in SPH code. The solid and dotted lines show the cooling function for Case A and C, respectively. The dashed lines show the cooling function for Case B. From the top to the bottom line, each line corresponds to [Fe/H] = −1, −2 and −3, respectively.

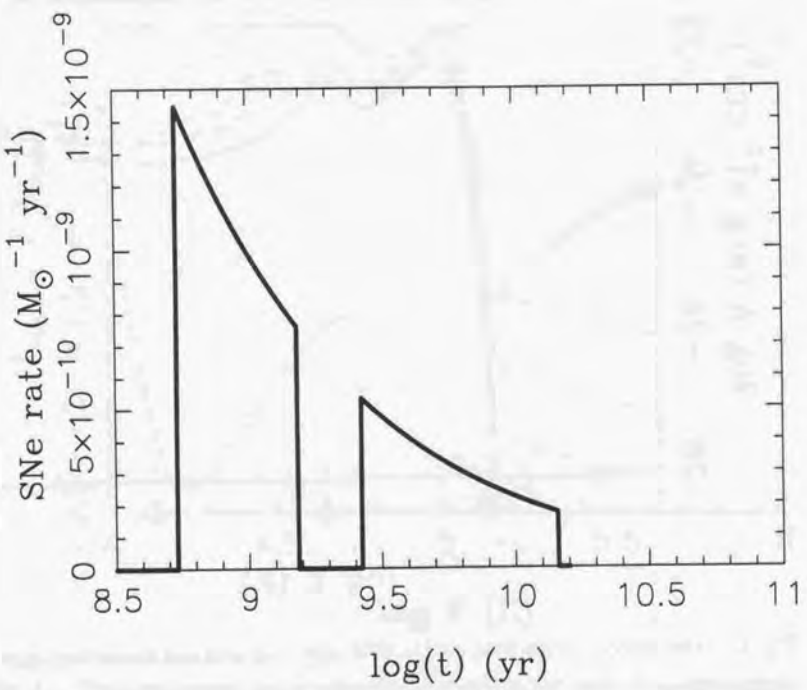

Fig. 5.— The Type Ia supernova rata ($R_{\rm SNIa}$) as a function of time.

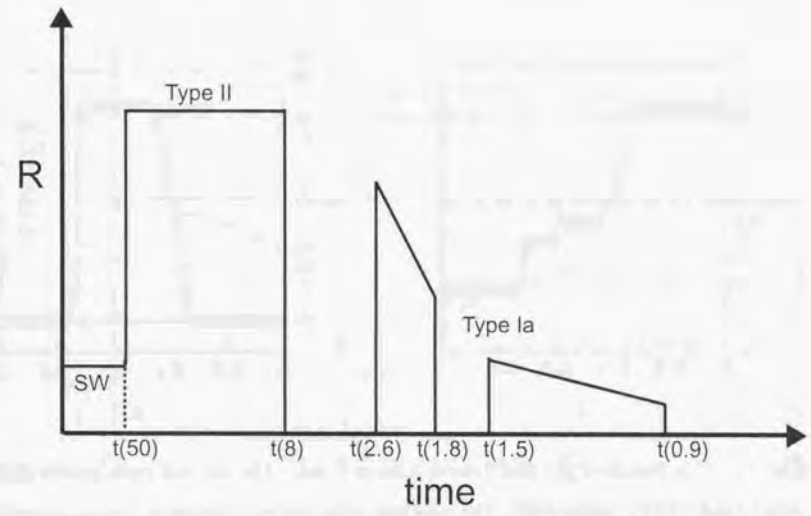

Fig. 6.— The schematic view of the feedback processes in our SPH code. The "t(m)" is the stellar lifetime as a function of mass ($m/M_\odot$).

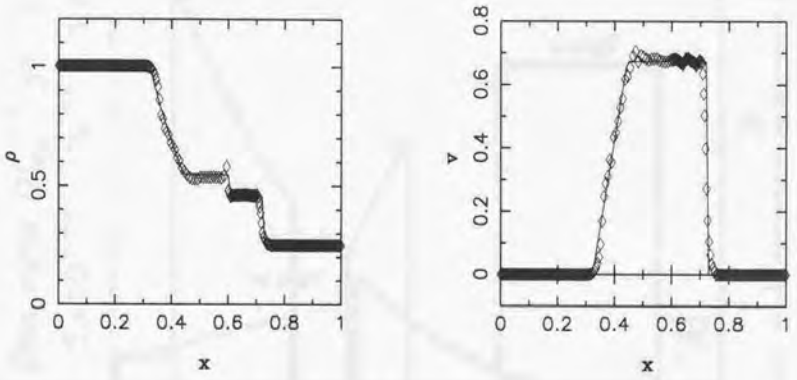

Fig. 7.— The results of the Sod's shock tube problem. The left and right panels show a density and velocity, respectively. The solid line is the analytic solution and the square shows the numerical results.

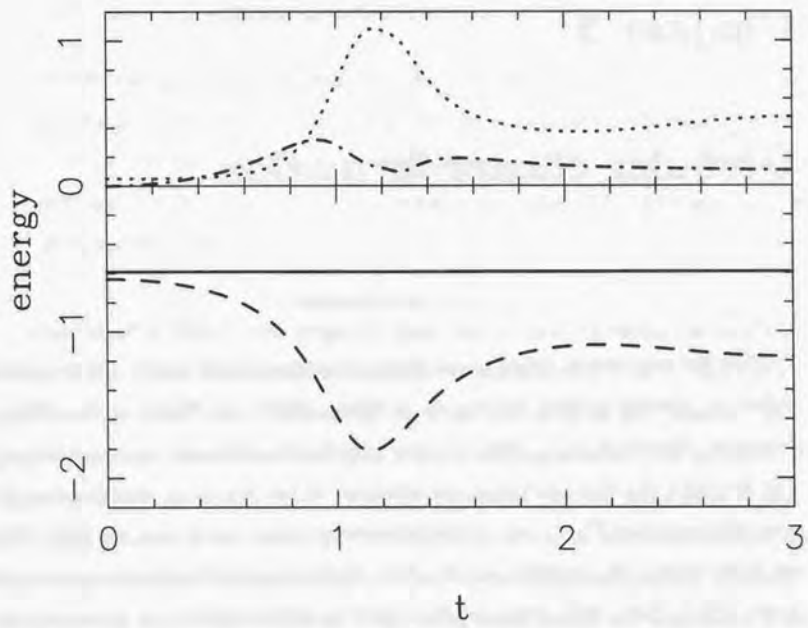

Fig. 8.— The results of the adiabatic collapse: the evolution of various energies are plotted as total (solid line), potential (dashed line), thermal (dotted line) and kinetic (dash-doted line) energies.

Chapter 3

Globular cluster formation

1. Introduction

The globular clusters belong to the oldest populations in our galaxy. For the general reviews on globular clusters, see Meylan, & Heggie (1997) and Harris (1991). Their formation (Elmergreen et al. 1999) is closely related to the formation process of our galaxy. The formation of a globular cluster may take place in two stages: (1) the formation of a proto-globular cloud (PGC) and (2) the formation of a star cluster from the PGC. There are three scenarios for the formation of a PGC, denoted as primary, secondary, and tertiary model (Fall & Rees 1987), where the PGC forms in different stages, i.e., before, during, or after the collapse of the galaxy, respectively.

- The primary model was suggested by Peebles & Dicke (1968). They showed that the Jeans mass of the recombination stage of the universe is comparable to the observed masses of globular clusters and thus the PGC can form due to the gravitational instability. Globular clusters may be debris of these objects. The most serious problem with this primary model is that there have been few intergalactic globular

clusters discovered. Almost all globular clusters ever discovered exist in galaxies.

- In the secondary model, on which we concentrate in the present paper, the PGC forms due to thermal instabilities (Fall & Rees 1985). Our detailed investigation and calculation are presented in the following sections.

- For the tertiary model, one example is that globular clusters form from large-scale unorganized motion of interstellar gas as in the Magellanic Clouds, which are now producing young clusters (Kumai, Basu & Fujimoto 1993). Another example is that very young globular clusters are observed in nearby galaxy NGC 1705 and 1569 (Ho & Filippenko 1996).

Once the PGC forms, there might be many ways to form a globular cluster (GC). Murray & Lin (1993) summarized the scenarios of the formation of GCs from PGCs as follows. The PGC can be divided into two types depending on their masses. The cloud, whose mass exceeds the Jeans mass, is gravitationally unstable, thus spontaneously collapsing to form stars. The cloud, whose mass is smaller than the Jeans mass, is stable until some instabilities are introduced. A cloud-cloud collision or cloud-disk collision can trigger such instability. When such collisions occur, the cloud would become thermally unstable owing to the efficient cooling. This cooling would lead to the formation of a very dense region, thus inducing a burst of star formation.

In the thesis, we examine quantitatively the above still qualitative scenario of the globular cluster formation. We use our Smoothed Particle Hydrodynamics (SPH) code (Lucy 1977; Gingold & Monaghan 1977) to simulate the formation of a globular cluster from a PGC. Our code includes the following physical processes: radiative cooling, star formation, energy feedback from stars including stellar winds and supernovae, and chemical enrichment from stars. The SPH method which includes star formation processes like ours

has been applied to many astrophysical problems. Such problems include the formation of isolated galaxies (Katz 1992; Steinmetz & Müller 1994), the evolution of galaxies (Friedli & Benz 1995), and the cosmological simulations (Navarro & White 1993). However, our study is the first attempt to apply this method to the globular cluster formation.

Among the two triggers of the instability, collapse and collision, we concentrate on the collapse case in the present paper. The collision case for a wide range of parameters (masses of the two clouds, a relative velocity between the clouds etc.) will be discussed elsewhere.

2. Method

To simulate the formation of a star cluster from gases, we use our GRAPE-SPH code using Remote-GRAPE library (Nakasato, Mori & Nomoto 1997). The details of our GRAPE-SPH code are described in Chapter 2. In this section we note on the star formation algorithm and the specific treatment of the energy feedback used in this chapter.

In the regions with increasing densities, first two conditions for the star formation (Eq. 2.25 and 2.26) are almost satisfied. Thus whether STAR forms in some regions is determined mostly by the Jeans criterion (Eq. 2.27). The critical density for the star formation in our treatment is obtained as

$$\rho_{\rm Jeans} > \left(\frac{\gamma b}{4\pi G\mu m}\right)^3 \frac{1}{m_i^2} T^3 \left(\frac{1}{\beta^6}\right). \tag{3.1}$$

Here, it is assumed that the neighbor radius is expressed as

$$h_i = \beta \left(\frac{m_i}{\rho_i}\right)^{1/3}, \tag{3.2}$$

where β is determined experimentally, because h_i is determined in order to make the number of neighbor particles almost constant in some range (30 - 80 in our codes). Since the typical value of β is 1.0 - 1.1, β^6 ranges 1.0 - 2.0. Then if m_i is constant, the critical

density is determined almost only by the temperature. The typical calculations in the present paper use 5000 gas particles for a $10^6\ M_\odot$ gas sphere. Thus the initial mass per particle (m_i in Eq. 3.1) is $\sim 200\ M_\odot$. For $T = 10^3$ K and 10^2 K, the critical density for star formation is $\rho_{\rm Jeans} \sim 10^{-17}$ and 10^{-23} g cm^{-3}, respectively. With the star formation recipes used in our SPH code, the STAR forms only in the very high density region if $T \sim 10^4$ K. There are, however, the maximum density ($\rho_{\rm max}$) that numerically reached in the SPH method; it is estimated

$$\rho_{\rm max} \sim \frac{N_{\rm n} m_i}{\epsilon^3}, \tag{3.3}$$

where $N_{\rm n}$ is the number of neighbor particles and ϵ is the gravitational softening length. In the present calculations, $\rho_{\rm max} \sim 1.8 \times 10^{-20}$ g cm^{-3}, These arguments ensure that with the star formation recipes used in our SPH code and the initial conditions of the present calculations, the STAR forms in the region where the temperature is as low as 10^2 K.

As described in Chapter 2, the thermal energies, gases, and heavy elements from stellar winds and supernovae are smoothed over neighbor particles of the STAR within a neighbor radius of R_f (feedback radius). We treat R_f as a parameter to meet the observational constraints. Such neighbor particles are called "in heating phase". When the gas particles are in heating phase, we assume that the cooling is suppressed as proposed in Mori, Yoshii & Nomoto (1999). This treatment produces the high temperature region around the STAR and the star formation is forbidden in the gas particles in heating phase.

3. Proto-Globular Cloud formation

We first examine the radiative condensations, which occur in a wide range of astrophysical circumstances from solar prominence to interstellar clouds (Meerson 1996). Radiative condensations in optically thin plasma have been considered by many authors since the pioneering work by Parker (1953) and Field (1965). The scale length of

gravitational instability in a collapsing proto-galaxy is much larger than the radii of globular clusters (Lin & Murray 1996). As will be shown in the following sections, the scale length of radiative condensations is comparable to the radii of globular clusters. Thus, in a collapsing proto-galaxy, radiative condensations may be the only mechanism to form a PGC (Fall & Rees 1985; Lin & Murray 1996).

3.1. Radiative condensations in a collapsing proto-galaxy

The characteristic equation for the growth rate of radiative condensations, n, is obtained from the linearized equations for perturbations as

$$n^3 + n^2 c_s \left(k_T + \frac{k^2}{k_K} \right) + n c_s^2 k^2 + \frac{c_s^3 k^2}{\gamma} \left(k_T - k_\rho + \frac{k^2}{k_K} \right) = 0, \tag{3.4}$$

where c_s is the sound speed, γ is the ratio of the specific heats, $k = 2\pi/\lambda$ is the wavenumber of the perturbation, k_ρ and k_T are the wavenumber of sound waves whose frequencies are equal to the growth rate of isothermal and isochoric perturbation, respectively, and k_K is the inverse of the scale length of thermal conduction (Field 1965). k_ρ, k_T and k_K are expressed as

$$k_\rho = \frac{\mu(\gamma-1)\rho_0}{c\mathrm{k_b}\mathrm{T_0}} \frac{\Lambda(T_0)}{\mu^2}, \tag{3.5}$$

$$k_T = \frac{\mu(\gamma-1)}{c\mathrm{k_b}} \frac{\rho_0}{\mu^2} \frac{d\Lambda}{dT}, \tag{3.6}$$

$$k_K = \frac{c\mathrm{k_b}\rho_0}{\mu(\gamma-1)\kappa}, \tag{3.7}$$

where T_0 and ρ_0 are the equilibrium temperature and density, respectively, $\mathrm{k_b}$ is the Bolzman constant, and $\Lambda(T)$ is the cooling function. We assume $\gamma = 5/3$ and $\kappa = 5.6 \times 10^{-7} \quad T^{2.5}$ erg s^{-1} K^{-1} cm^{-1}. Solving Eq. (3.4) as a cubic equation of n for different k, we obtain the dispersion relation between n and k. In applying to our galaxy, we adopt $T_0 \sim 1.0 \times 10^6$ K and $\rho_0 \sim 1.7 \times 10^{-24}$ g cm^{-3} (Fall & Rees 1985). With these values, the dispersion relation

has a peak at some k . In the present paper, we assume that the scale for the maximum growth rate is typical scale of a PGC. To obtain the typical scale of a PGC for different T_0 and ρ_0, equation (3.4) is viewed as a quadratic in k^2 (see Section II (d) in Field (1965)).

The results for different T_0 and ρ_0 are presented in Figure 1. In applying to our galaxy, we obtain the scale length of ~ 600 pc. This scale length is consistent with the following simple estimate. For the adopted cooling function, the wavelengths for k_ρ and k_K with $T_0 \sim 1.0 \times 10^6$ K and $\rho_0 \sim 1.7 \times 10^{-24}$ g cm^{-3} are respectively obtained as

$$\lambda_\rho > 10^3 \quad \mathrm{pc} \quad \text{and} \quad \lambda_K < 1 \quad \mathrm{pc}. \tag{3.8}$$

This implies that the perturbation with a scale greater than 10^3 pc is dumped owing to the limit of the sound speed, and the perturbation with a scale smaller than 1 pc is also dumped by thermal conduction. Thus the typical scale of a PGC in our galaxy is estimated to be several hundreds pc and the mass of a PGC ranges from 10^7 to 10^8 $M_\odot$.

3.2. Density profile of a PGC

The estimated scale of a PGC is larger than the present radius of globular clusters (10 - 100 pc). This implies that during radiative condensations, a PGC shrinks before star formation begins or star formation in a PGC occurs in the central region of the cloud. If we consider the metal-free PGC where the ionization equilibrium is achieved, the cooling time, t_c, of the PGC is much shorter than the dynamical time, t_d ($t_c/t_d \sim 0.25$ for $T_0 \sim 1.0 \times 10^6$ K and $\rho_0 \sim 1.7 \times 10^{-24}$ g cm^{-3}). After the short period of radiative condensations ($\sim t_c$), the PGC becomes a warm dense cloud ($T \sim 10^4$ K) surrounded by a hot thin gas with T_0 (Fall & Rees 1985).

The qualitative discussion on the evolution of such a metal-free PGC has been presented by Lin & Murray (1996). They argued that in the first stage of collapsing galaxy,

the assumption of ionization equilibrium is not valid because of little radiative emission. If the ionization equilibrium is not achieved, the temperature of high density regions can be as low as $\sim 10^2$ K due to hydrogen molecular cooling. In this case, the high density cold cloud with $T = 10^2$ K is surrounded by a warm gas. The critical mass of the isothermal sphere confined by an external pressure depends on the cloud temperature (Ebert 1955; McCrea 1957). If the temperature of the cloud is $\sim 10^2$ K, the critical mass is $\sim 10^2\ M_\odot$. According to Lin & Murray (1996), such a small cloud as $M \sim 10^2\ M_\odot$ collapses to make the first stars in the proto-galaxy. These first generation stars are the source of radiative emission to maintain the ionization equilibrium. If such radiation continues long enough, a cold PGC will evolve almost isothermally with $T \sim 10^4$ K and form the isothermal profile of $\rho \propto r^{-2}$. The core size of the PGC will decrease from the initial size of several hundreds pc to a size comparable to the observed globular cluster. According to these arguments, we can assume that the density structure of a PGC has a form of $\rho \propto r^{-2}$.

For the initial density profile of the PGC, we use the King model with the concentration parameter $c = 0.5$ (Binney & Tremaine 1987). The mass of the sphere is assumed to be $M = 10^6\ M_\odot$, which nearly equals to the Jeans mass of the current conditions (ρ_0 and T_0). We assume that this sphere represents the inner regions of the PGC. We examine three different cases for a initial radius of $R_i = 150$, 200, and 300 pc. The initial density profiles of the three cases are presented in Figure 2. For the smaller R_i, the central density of the PGC is higher. The temperature of the sphere is assumed to be $T \sim 10^4$ K. The properties of the inner region of the PGC, which are the initial conditions of our calculations, are summarized as follows:

- The mass of the clouds is $M \sim 10^6\ M_\odot$.
- The radius of the clouds is $R_i \sim 150$ - 300 pc.
- The clouds is an isothermal sphere with $T \sim 10^4$ K.

- Initially, the velocity of the cloud is zero.

In the following calculations, the initial number of gas particles is ~ 5000 so that the initial mass of the one gas particle is $\sim 200\ M_\odot$. The dependence of varying the initial number of gas particles is discussed in Section 4.3. In all cases, the gravitational softening length for all particles is set to be 1 pc and fixed during the calculations.

4. Results

First, we note on the feedback radius (R_f). We use the Strömgren radius ($R_{\rm St}$) of a typical OB star as R_f. The typical value is $R_{\rm St} \sim 10$ - 100 pc, where the density of the ISM is ~ 1 cm^{-3} (Osterbrock 1974). The radius depends on the density of the ISM as $R_{\rm St} \propto n^{-2/3}$. In the central region of our initial models, n ranges from 100 cm^{-3} to 1000 cm^{-3}. Thus, we can estimate $R_f \sim 1-5$ pc (using the largest value of $R_{\rm St}$). In the following two subsections, we choose $R_f = 3$ pc for all gas particles. The results for both cases are summarized in Table 1. The results for different R_f are described in Section 4.3.

4.1. Evolution of the metal-free PGC

In this section, we describe the evolution of the metal-free PGC for case C.

As presented in the previous sections, the metal-free PGC may evolve isothermally with $T \sim 10^4$ K. The isothermal evolution of PGC is terminated when the ionizing radiations from the first generation stars stop. Without ionizing radiation, the PGC cools efficiently by H_2 molecules. Our calculations start from that time when the PGC begins to cool. We assume $M = 10^6\ M_\odot$, and the initial temperature of $T = 10^4$ K and the King profile sphere. Since the size of the PGC at this stage is unknown, we examine three different cases for an

initial radius of $R_i = 150$, 200, and 300 pc.

In all three cases, the initial density of the central region is high enough for efficient cooling to occur, so that the temperature of the central region decreases rapidly to $\sim 10^2$ K. Due to the high density and low temperature ($\sim 10^2$ K), a burst of star formation occurs in the central region in all cases. After the first star formation, the central region becomes the heating region and the temperature of the central region increases gradually.

At $t \sim 6$ Myr, Type II supernovae start to occur and the temperature of the heating region increases rapidly to T $\sim 10^9$ K. The left panel of Figure 3 shows the evolutionary changes in the central temperature for $R_i = 150$ pc. Such a high temperature region expands and the central density begins to decrease (see the right panel of Figure 3). The expansion of the central region leads to the formation of a shell structure as seen in the evolution of the gas density profile (Figure 4). The density profile at $t = 6$ Myr, clearly shows the shell structure. After that time, the shell expands outwardly (see the right panel of Figure 4).

The star formation after the shell formation occurs not in the central region but in the shell. Figure 5 show the change in the radius of the star forming region as a function of time for $R_i = 150$ pc. We can see that the star forming region moves outward. At $t = 10$ Myr, where we stop the computation for $R_i = 150$ pc, the stellar mass reaches $\sim 1.3 \times 10^5\ M_\odot$. This means that the star formation efficiency is ~ 13 %. The bound stellar mass at $t =$ 10 Myr is $\sim 10^5\ M_\odot$ and the mass is comparable to the typical mass of globular clusters ($\sim 10^5\ M_\odot$). At $t = 10$ Myr, the gas is almost removed from the central region. Figure 6 shows the projected particle positions of STAR particles (left panel) and the stellar density profile (right panel) at $t = 10$ Myr. The STAR particle shows elongated shape (bar like shape). Such a shape is caused by the radial orbit instability of the STARs formed at the large radius (Palmer & Papaloizou 1987). The central density of STARs is as high as $\sim$

100 $M_\odot$ pc^{-3} and the central velocity dispersion of the STARs is ~ 3 km s^{-1}. This value of velocity dispersion is smaller than the observed value (Dubath, Meylan & Mayor 1997). We need to follow further evolution of the star clusters for proper comparison, which is not feasible with present code. The number of STAR particles at $t = 10$ Myr is ~ 2500.

For $R_i = 200$ pc and 300 pc, the overall evolution is similar to the case for $R_i = 150$ pc and the stellar masses at $t = 10$ Myr are $\sim 8.5 \times 10^4\ M_\odot$ and $\sim 5.6 \times 10^4\ M_\odot$, respectively. The bound stellar mass are $\sim 5 \times 10^4\ M_\odot$ for both case. These results are summarized in Table 1. The initial concentration correlates with the final stellar mass and the final concentration of stellar system. In order for the stellar system as massive as $10^5\ M_\odot$ to form, the PGC should be as compact as $R_i < 200$ pc ($\rho_c > 10^{-22}$ g cm^{-3}) for the metal-free condition.

4.2. Evolution of the metal-rich PGC

The chemical composition of stars in globular clusters is one of the most crucial quantities to constrain the model for the globular cluster formation. The assumption that PGC initially has some heavy elements is quite reasonable. Actually, all globular clusters in our galaxy have some metals of [Fe/H] $= -2.25$ - 0. The metallicity distribution of the globular clusters shows bimodal distributions (Harris 1991). From this fact, we choose the initial metallicity of the cloud ranging from [Fe/H] $= -2$ to 0. For comparison, we will evolve the lower metallicity ([Fe/H] $= -3$) cloud. The results presented in this section are obtained for case B.

Using the same initial conditions presented in section 4.1, we evolve the PGC for different metallicity. For the initial radius of the cloud, we set $R_i = 300$ pc. The first star formation occurs in the central region and the STARs heat up the surrounding matter to

gradually increase the temperature of the central region. At $t \sim 6$ Myr, Type II supernovae begin to occur and the temperature of the heating region increases rapidly to $T \sim 10^6$ K. Figure 7 shows the evolutionary changes in the central temperature (left panel) and gas density (right panel) for [Fe/H] $= -2$. Although the initial decrease in the temperature is small, the evolution for [Fe/H] $= -2$ is similar to the evolution of the metal-free cloud. After $t \sim 6$ Myr, the central high density region makes the shell structure as in the metal-free case. At $t = 10$ Myr, the bound stellar mass reaches $\sim 1.0 \times 10^5\ M_\odot$ for [Fe/H] $= -2$.

For higher metallicity, i.e., [Fe/H] ≥ -1, details of the evolution are somewhat different. We compare the central temperature evolution for different metallicity in Figure 8. Due to the different cooling rate, the initial decrease in the temperature is larger for higher metallicity. This difference leads to different star formation history as shown in Figure 9. For [Fe/H] $= 0$, the initial star burst is very intense and then the SFR decrease sharply becoming lower than the low metallicity case after $t = 1$ Myr. This is because the heating rate due to the stellar winds is much larger for higher metallicity. The rise in the SFR after $t = 6$ Myr for [Fe/H] $= 0$ is caused by Type II supernovae.

The SFR for [Fe/H] $= -1$ is almost constant during the evolution. For [Fe/H] $= -2$, the first star formation occurs at $t \sim 0.5$ Myr because of the lower cooling rates. The SFR after $t = 2$ Myr is almost constant but lower than for [Fe/H] $= -1$.

The bound stellar mass at $t = 10$ Myr is $\sim 1.5 \times 10^5\ M_\odot$ and $1.0 \times 10^5\ M_\odot$ for [Fe/H] $= -1$ and 0, respectively. The reason for such a metallicity dependence is summarized below. The bound stellar mass, the central stellar density, and the central velocity dispersion are summarized in Table 1. The results depend on the metallicity as follows:

1. The initial metallicity significantly affects the star formation history. This difference makes the subsequent evolution different.

2. For the higher metallicity, the final stellar mass at $t = 10$ Myr is larger because of the more efficient cooling rate.

3. The bound stellar mass is not an increasing function of the initial metallicity. This is because heating due to the stellar winds is larger for higher metallicity.

4. For lower metallicity ([Fe/H] $= -3$), only $\sim 3 \times 10^3\ M_\odot$ stars form. This implies that [Fe/H] ≥ -2 is necessary to form globular clusters of $\sim 10^5\ M_\odot$ if $R_i \sim 300$ pc.

The stellar mass for [Fe/H] $= -3$ ($\sim 3 \times 10^3\ M_\odot$) is much smaller than that for the metal-free cloud ($\sim 5.5 \times 10^4\ M_\odot$). This is because the cooling rate for [Fe/H] $= -3$ at $T < 10^4$ K is smaller than the cooling rate due to H_2 molecules as shown in Figure 4 of Chapter 2. Consequently, the formation of H_2 molecules or some heavy metals is required to efficiently cool the proto-galactic clouds.

4.3. Parameter dependence

In this subsection, we describe the dependence of the results on various numerical parameters, e.g., the initial particle number (N_i) and the feedback radius (R_f). We use the metal-rich cloud of [Fe/H] $= -1$ as a reference model, where $N_i = 5000$ and $R_f = 3$ pc.

First, we describe the dependence on the initial particle number. With larger (smaller) number of initial gas particles, the initial masses of the gas particles are smaller (larger). There is no strong dependence on the mass of the gas particles in our star formation recipes because Eq. (2.32) dose not include the mass of the gas particles. However, the maximum density ($\rho_{\rm max}$) that can be represented in the SPH method depends on the mass of the gas particles, which may produce weak dependence on N_i. To confirm this, we evolve the model with $N_i = 10^4$. The overall evolution is almost indistinguishable to the reference model.

The stellar mass at $t = 10$ Myr becomes $\sim 1.2 \times 10^5\ M_\odot$, which is slightly smaller than $1.3 \times 10^5\ M_\odot$ in the reference model. For $N_i = 2500$ (a half of the reference model), we obtain the stellar mass of $\sim 1.5 \times 10^5\ M_\odot$. In Figure 10, we compare the gas density profiles at $t = 10$ Myr for different N_i. The position of the shell for the model with $N_i = 10^4$ is different from other models because of the smaller stellar mass at the same epoch. However, all three models show the similar density profiles so that we conclude that the dependence on the initial gas particle number is week. Thus, $N_i \sim 5000$ is sufficient for the current numerical model.

Secondary, we describe the dependence on the size of the feedback radius R_f. In our model, the cooling and the star formation are suppressed for the gas particles in heating phase. We therefore expect that the size of R_f affects the star formation history. With larger $R_f = 5$ pc, the star formation rates are smaller and the final stellar mass ($\sim 0.9 \times 10^5\ M_\odot$) is smaller than $1.3 \times 10^5\ M_\odot$ in the reference model ($R_f = 5$ pc). On the other hand, we obtain the stellar mass of $\sim 1.9 \times 10^5\ M_\odot$ with smaller R_f ($= 2$ pc). Within the reasonable range of R_f around 3pc, the final stellar mass changes by a factor of 0.7 - 1.5.

4.4. Summary of the numerical results

The results of our calculations are summarized as follows (see also Table 1) :

1. In all cases, the overall evolution is similar. Initially, the star burst occurs in the central region. The central star burst is halted by the heating due to Type II supernovae. The heating cause the expansion of the central region and forms a shell structure. The subsequent star formation occurs in the shell.

2. For the metal-free collapse case, the stellar mass at $t = 10$ Myr correlates with initial concentrations. To obtain the star cluster as massive as globular clusters ($\sim 10^5\ M_\odot$), the initial concentration of the PGC must be large enough, i.e., $R_i < 200$ pc.

3. For the metal-rich collapse, the initial metallicity significantly affects the evolution. To obtain the star cluster as massive as globular clusters, the initial metallicity must be as larger as [Fe/H] ~ -2. If the initial metallicity is low ([Fe/H] < -2), very few stars form.

4. This suggests that during the initial phase of the galaxy formation, i.e., when the ISM contains little heavy element, the formation efficiency of the globular cluster is low.

5. The results is not strongly affected by the initial number of gas particles. $N_i \sim 5000$ is sufficient for the current numerical model. The dependence on the feedback radius is more evident.

5. Discussion

5.1. Star formation in the shell

In all our numerical models, a shell-like gaseous structure is formed. The formation of the shell-like structure of gases has also been reported in the simulations of the formation of dwarf elliptical galaxies (Mori et al. 1997; Mori, Yoshii & Nomoto 1999). They argued that the difference in the density structure between normal ellipticals (de Vaucouleurs law) and dwarf ellipticals (exponential law) can be explained by the formation of such a shell-like structure and the star formation in the shell. The most crucial difference between the normal elliptical and the dwarf is their mass, and the less massive galaxy is more strongly affected by the energy inputs from stars. Similar argument may be applicable to our numerical models. In the case of the globular cluster formation, however, the mass is even smaller than the dwarf galaxies. Owing to this fact, the effect of the energy inputs from stars is more drastic so that the star formation in the shell is much less efficient than

in the dwarf galaxies. Also, the stars formed in the shell is not gravitationally bound due to the outward velocity of the shell. Thus, the bound globular cluster consists of the stars formed before the shell formation. The stellar density of such stars is not affected by the shell formation and the star formation in the shell.

The chemical composition of stars in globular clusters is one of the most crucial quantities to constrain the model for the globular cluster formation. The stars in a globular cluster have almost the same heavy elements abundances (Suntzeff 1993). This small dispersion in metallicity (σ[Fe/H]) suggests that the formation period of globular clusters is so short that the stars in globular clusters can be regarded to form almost simultaneously as shown in our numerical models.

Brown, Burkert & Truran (1991, 1995) suggested that the second generation stars would form in the shell and the self-enrichment could occur there. In our model, the star formation takes place in the shell after $t = 5$ Myr (see Figure 5). However, when the stars form in the shell, the shell has not been enriched with newly ejected heavy metal as shown in the solid line in Figure 5. This line shows the radius of the metal-enriched region defined as $r = (\Sigma r_i m_i)/(\Sigma m_i)$ by summing over the metal-enriched gas particles. The metal-enriched region expands outwardly but does not reach the star forming region, which implies that the self-enrichment dose not occur in our model (we note that the star formation is suppressed in the gas particles near the STARs in our numerical model). In the present numerical model, the STAR inherits the chemical composition of the corresponding gas particle. Hence the metallicity of STARs is same as the initial metallicity of gases. In the present model, no external medium outside the cloud is included, because of technical difficulties in the SPH method (see, however, Nagasawa & Miyama (1987) for a possible improvement). If there exists external medium outside the cloud, the density of the shell would be higher and the star formation history would be different; this possibility needs

further study to confirm.

5.2. Failed Globular clusters

When a PGC is an initially metal-free cloud or the initial metallicity of a PGC is low, the resulted mass and the central stellar density are lower than the observed mass and density of the globular clusters. Such "failed" globular clusters might be the field halo stars. Another possibility is a open cluster. Typical age of open clusters in our galaxy is $\tau < 10^9$ yr. However, there also exist such old open clusters as $\tau > 10$ Gyr (Friel 1995). The age of the most old open cluster is comparable to the age of globular clusters. The central density of the "failed" globular cluster is as low as the central density of typical open clusters. Thus, the formation processes of such old open clusters may be the similar to our model of globular cluster formation but starting from lower initial concentration. Very old open clusters might be the debris of "failed" globular clusters and there might have existed many more open clusters at the formation of our galaxy.

6. Conclusions

For the processes of globular clusters formation, only the qualitative scenarios have been discussed previously (Fall & Rees 1985; Lin & Murray 1996). In this paper, we present the first attempt to simulate the globular cluster formation with three-dimensional hydrodynamical method, which includes the star formation and its feedback effects. We assume that, in the collapsing galaxy, isothermal cold clouds form through thermal condensations and become proto-globular clouds. We obtain the size of proto-globular clouds by means of the linear stability analysis (Figure 1) and compute the evolution of the inner region of the PGC starting from various initial radius R_i. The results of our

calculations are summarized as follows:

1. In order for the globular cluster-like system to form from a metal-free PGC, the initial concentration of the PGC must be large enough.

2. It is required that the metallicity of a PGC is high enough to produce the globular cluster-like system. In our calculations, the required metallicity is estimated to be [Fe/H] ≥ -2.

3. In all cases, the shell like structure of the gas forms. Although the star formation occurs in the shell, the self-enrichment is not seen to occur.

Based on the earlier qualitative works and the present quantitative results, the processes of globular clusters formation in the proto-galaxy can be understood as follows:

1. In the collapsing proto-galaxy, the first generation stars of $M \sim 10^2\ M_\odot$ form due to the efficient cooling by hydrogen molecules. Such population III stars eject the gas with heavy elements and chemically contaminate the proto-galaxy gases.

2. Such first generation stars radiate dissociative photons, and the entire proto-galaxy is settled down to ionization equilibrium.

3. With equilibrium cooling, the density perturbation grows due to thermal instability, and forms an isothermal cloud with a density structure of $\propto r^{-2}$. Such clouds are the proto-cloud of globular clusters.

4. When the density of the PGC becomes high enough, the burst of star formation occurs. Some high density clouds produce the globular clusters, and others may produce the field stars and/or the halo open clusters.

5. During the formation of the galaxy, the formation efficiency of the globular cluster become significantly large when the metallicity of the PGC become as large as [Fe/H] ~ -2.

As mentioned in section 5.1, we do not take account of the effect of the external medium in the present calculations. If we include the effect of the external medium, the structure of the shell may be different and further star formation may occur in that shell. Brown, Burkert & Truran (1995) suggested that only a few supernovae per Myr is sufficient to reverse the contraction of the $10^6\ M_\odot$ cloud. Such an effect of the external medium needs to be studied.

The globular cluster formation is considered to occur not only in the proto-galaxies but also in the present galaxies, e.g., LMC, SMC, and interacting galaxy NGC4038/NGC4039. In such environment, different formation processes would take place, which correspond to the tertiary models (Kumai, Basu & Fujimoto 1993). In the case of NGC4038/NGC4039 (the Antennae galaxies), many globular clusters are being produced by galaxy merging. Detail formation processes of globular clusters in such systems needs to be studied. Also, the effect of the formation of many globular clusters on the galaxy merging process needs a further study.

Table 1. The summary of the numerical results

R_i[a]	[Fe/H][b]	Mass[c]	ρ_c[d]	σ_c[e]
150 pc	no metal	$1.0 \times 10^5\ M_\odot$	$10^{2.5}\ M_\odot\ \mathrm{pc}^{-3}$	2.98 km s^{-1}
200 pc	no metal	$5.1 \times 10^4\ M_\odot$	$10^{1.1}\ M_\odot\ \mathrm{pc}^{-3}$	1.87 km s^{-1}
300 pc	no metal	$5.5 \times 10^4\ M_\odot$	$10^{1.4}\ M_\odot\ \mathrm{pc}^{-3}$	3.66 km s^{-1}
300 pc	0	$1.0 \times 10^5\ M_\odot$	$10^{2.0}\ M_\odot\ \mathrm{pc}^{-3}$	3.21 km s^{-1}
300 pc	-1	$1.5 \times 10^5\ M_\odot$	$10^{2.0}\ M_\odot\ \mathrm{pc}^{-3}$	2.33 km s^{-1}
300 pc	-2	$1.0 \times 10^5\ M_\odot$	$10^{1.7}\ M_\odot\ \mathrm{pc}^{-3}$	2.68 km s^{-1}
300 pc[f]	-3	$2.9 \times 10^3\ M_\odot$		

Note. — [a]The initial radius of the PGC.

[b]The initial metallicity ([Fe/H]) of the PGC.

[c]The bound stellar mass at $t = 10$ Myr.

[d]The central stellar density at $t = 10$ Myr.

[e]The central stellar velocity dispersion at $t = 10$ Myr.

[f] ρ_c and σ_c is omitted of this case.

Table 2. The dependence on numerical parameters

N_i[a]	R_f[b]	Mass[c]
5000	3 pc	$1.5 \times 10^5\ M_\odot$
2500	3 pc	$1.5 \times 10^5\ M_\odot$
10^4	3 pc	$1.2 \times 10^5\ M_\odot$
5000	2 pc	$1.9 \times 10^5\ M_\odot$
5000	5 pc	$8.6 \times 10^4\ M_\odot$

Note. — [a]Used initial gas particle number.

[b]The feedback radius.

[c]The stellar mass at $t = 10$ Myr.

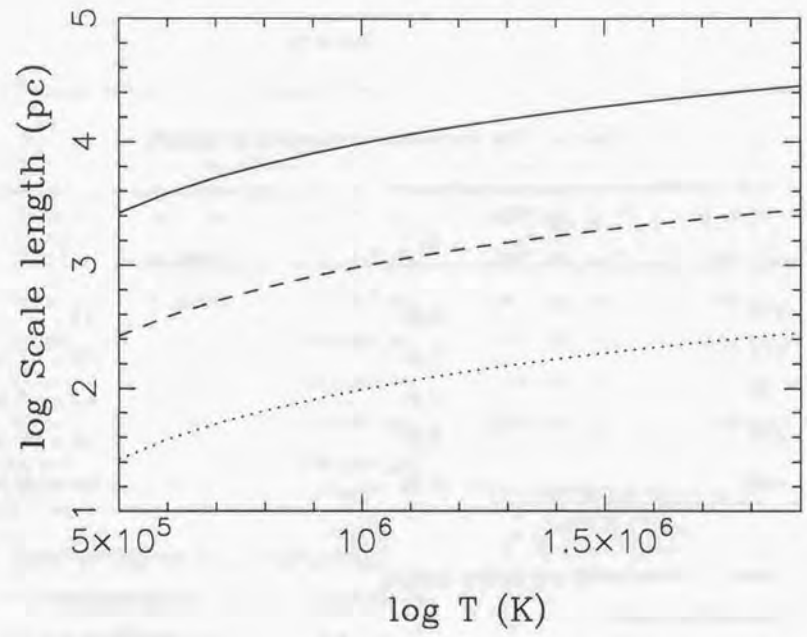

Fig. 1.— The estimated scale length of a proto-globular cloud corresponding to the maximum growth rate in Eq. (3.4). The solid, dashed, and dotted lines correspond to $\rho_0 = 1.0 \times 10^{-25}$, 1.0×10^{-24}, and 1.0×10^{-23} g cm^{-3}, respectively.

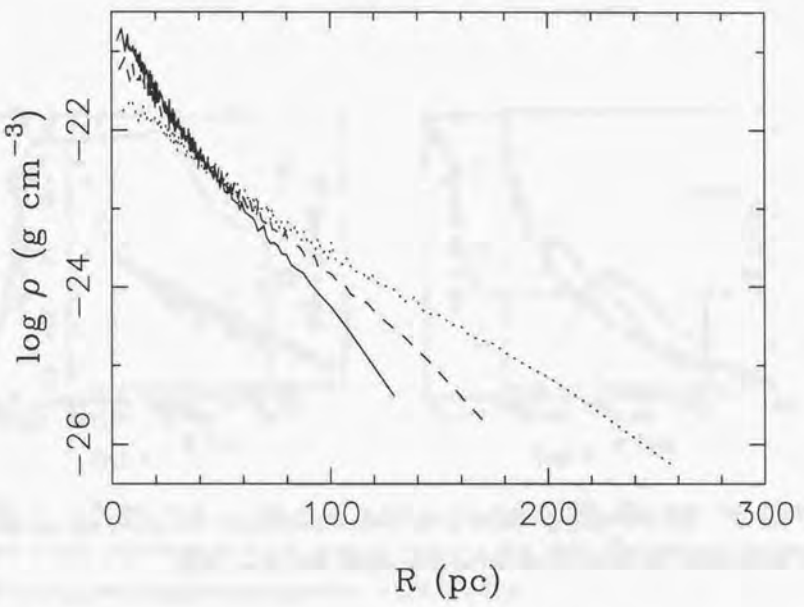

Fig. 2.— The initial gas density (g cm^{-3}) profile of the King model. The solid, dashed, and dotted lines show the profiles for $R_i = 150$, 200, and 300 pc, respectively.

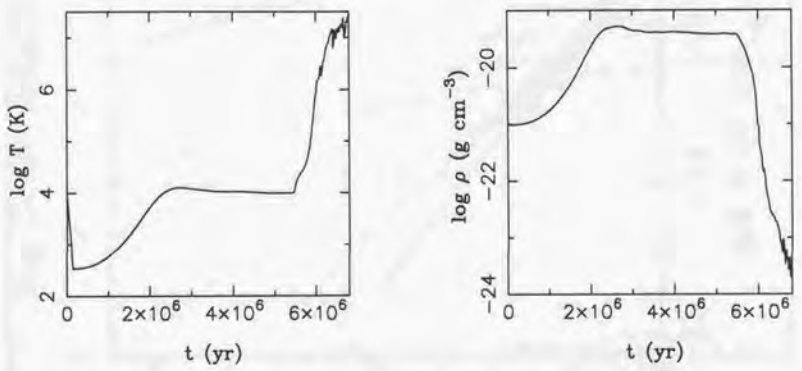

Fig. 3.— The evolutionary changes in the central temperature (left panel) and gas density (right panel) are shown for the metal-free collapse with $R_i = 150$ pc.

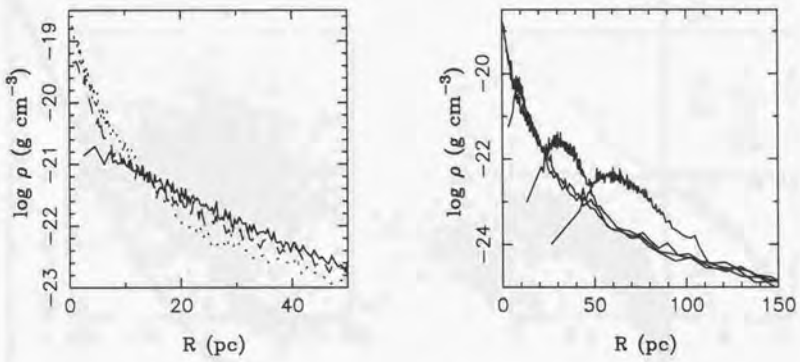

Fig. 4.— The gas density profile as a function of radius (pc). left: The solid, dashed and dotted lines respectively shows the profile at $t = 0$, 2, 4 Myr. right: The solid lines with the decreasing central density correspond to $t = 5$, 6, 7, 8 Myr.

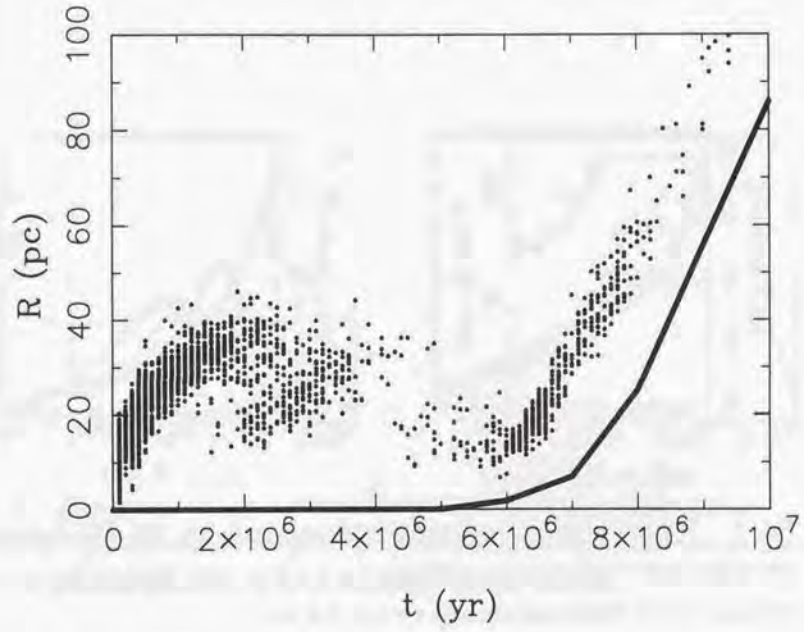

Fig. 5.— The radius (pc), at which stars form, as a function of time (yr) for the metal-free collapse with $R_i = 150$ pc.

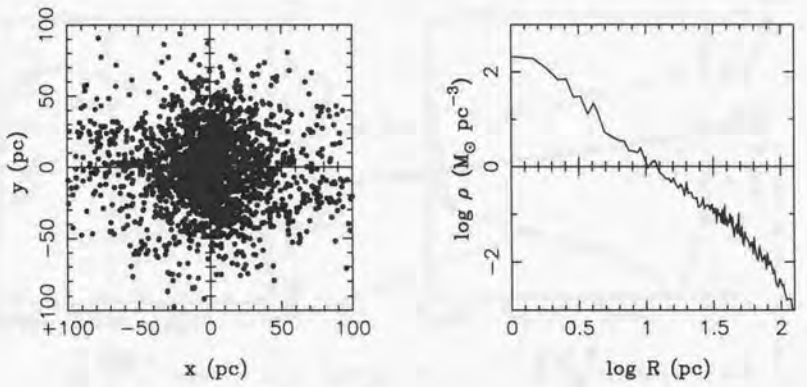

Fig. 6.— The projected position of particles at $t = 10$ Myr for metal-free collapse with $R_i = 150$ pc (left panel). The stellar density profile at $t = 10$ Myr for the same model.

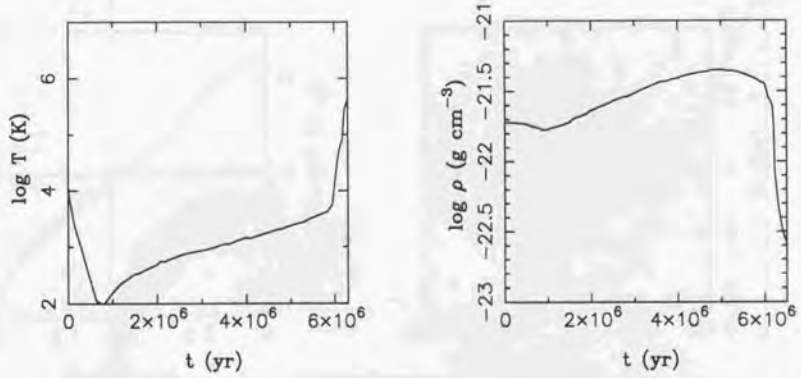

Fig. 7.— The evolutionary changes in the central temperature (left panel) and gas density (right panel) are shown for the collapse of [Fe/H] = −2 sphere.

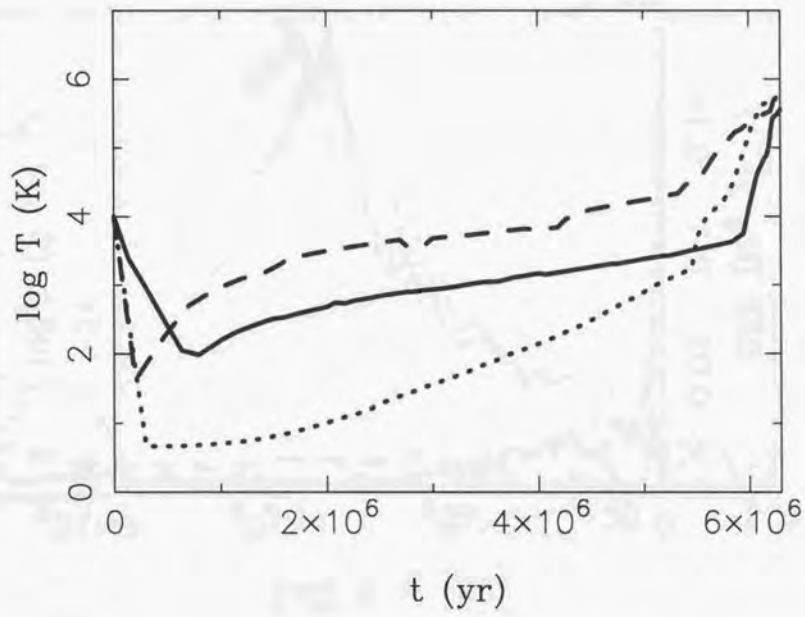

Fig. 8.— The evolutionary changes in the central temperature for the collapse of [Fe/H] = −2 (solid line), −1 (dashed line) and 0 (dotted line) sphere.

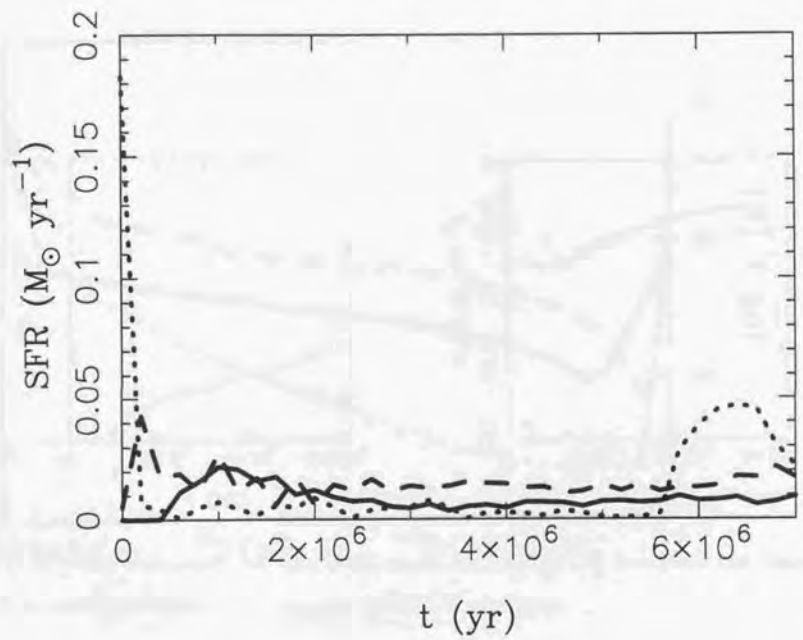

Fig. 9.— The comparison of SFR as a function of time for [Fe/H] = −2 (solid line), −1 (dashed line) and 0 (dotted line).

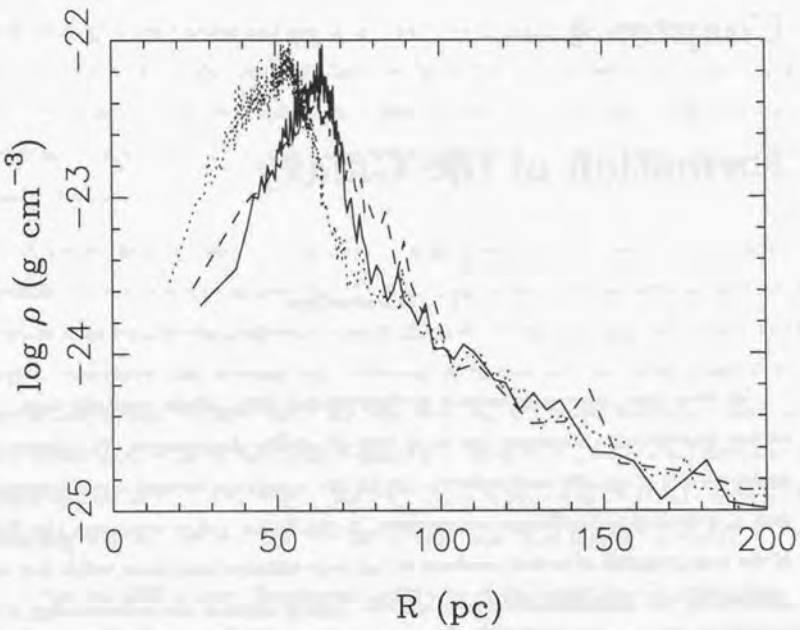

Fig. 10.— The comparison between the reference model (solid line) and other model. The dashed line corresponds to the model with $N_i \sim 2500$. The dotted line corresponds to the model with $N_i \sim 10000$.

Chapter 4

Formation of the Galaxy

1. Introduction

In these days, increasing number of observational data become available from various ground-based telescopes and many type of satellite observatories. To advance our understanding of astrophysical problems, the detail comparisons between such observational data and theoretical predictions are required. In the field of galaxy dynamics, the data of the proper motion of several hundreds of the solar neighborhood stars, which has been obtained by the *Hippaarcos* astrometry satellite, greatly enhance the understanding of the dynamics of the Galaxy (the Milky Way) and its formation and evolution process (Chiba & Yoshii 1998). In this chapter, we investigate the formation process of the Galaxy using high resolution numerical simulations. By comparing our numerical results with various high quality data, we can understand the formation process and evolution of the Galaxy.

From the observational point of view, there were two distinct scenarios for the formation of the Galaxy. One is the "free-fall collapse" scenario proposed by Eggen, Lynden-Bell, & Sandage (1962). By evaluating the orbital motions of stars near the sun, they found

a strong correlation between the orbital motion of stars (eccentricity) and the ultraviolet excess (metallicity). From this facts, they have concluded that the collapse that produce the Galaxy was very rapid and occurred in nearly free-fall time scale. On the other hand, Searle & Zinn (1978) have proposed the "slow collapse" scenario. They analyzed the metallicity of the halo globular clusters and found no correlation between the metallicity of clusters and its position. From this fact, they have concluded that the formation of the Galaxy was not the ordered collapse as proposed by Eggen, Lynden-Bell, & Sandage (1962) but the processes in which small fragments continued to collapse for a longer time scale than the free-fall time scale.

A recent theory predict that the galactic scale objects were formed by the structure formation in the cold dark matter (CDM). According to the CDM scenario, larger clumps increase their mass by the progressive merger of smaller clumps. During such evolutions, the angular momentum also increases due to the angular momentum transfer by a tidal force of surrounding clumps. At some epoch, the over-dense region is virialized to form a dark halo of a certain mass. Namely, the Galaxy formation occurred during the gradual formation of a dark halo in the CDM cosmology. Thus, the formation process of the Galaxy in the CDM cosmology was the midway of the "free-fall collapse" and "slow collapse" scenarios.

After late 1980's, three-dimensional simulations of the formation of a galaxy have become possible because of more sophisticated numerical algorithms and the evolution of available computing resources. In Katz (1992), the first self-consistent three-dimensional simulation of cosmological galaxy formation was done. He investigated the evolution of a spherical top hat over-dense region of mixture of dark matter and gases with the Tree-SPH codes (Hernquist & Katz 1989). Using the star formation recipes, he was able to model the formation of a spiral galaxy, which consists of the nearly spherical dark halo, and the stellar and gas disk. The rotation curves of the stellar disk in his model shows flat rotation curves

like observed spiral galaxies. In the subsequent studies, Steinmetz & Müller (1994, 1995) investigated the disk structure of their model galaxy with the method and initial conditions similar to Katz (1992). Their model included a chemical evolution by formed stars so that they could compute the chemical properties of a spiral galaxy. Their model starts with the initial number of particles of $\sim$ 8,000 for both gas and dark matter particles. This means that the initial masses of the gas and dark matter particles in their simulations are 2×10^7 $M_\odot$ and 1.8×10^8 $M_\odot$, respectively. The spatial resolution of the model of Steinmetz & Müller is limited by the gravitational softening length of $\sim$ 1 - 2 Kpc (Steinmetz & Müller 1995). Such small number of particles and the limited spatial resolution are not sufficient to resolve the detailed structure of a spiral galaxy, especially the structure of a bulge component (the size of the bulge of our galaxy is $\sim$ 2 Kpc) and a thin disk.

In this thesis, we follow the method and the model by the previous authors but use more particles to study the detailed formation and evolution processes of the Galaxy. we evolve the spherical top hat over-dense region of mixture of dark matter and gases with our GRAPE-SPH code, which use the Remote GRAPE system (Nakasato, Mori & Nomoto 1997). Our SPH code includes various physical processes, i.e., radiative cooling, star-formation, energy feedback from stars, and chemical evolution. The largest model of this study uses initially over 50000 particles for a 10^{12} $M_\odot$ spherical region. This is, the initial masses of the gas and dark matter particles in such model are 4×10^6 $M_\odot$ and 3.6×10^7 $M_\odot$, respectively. The gravitational softening lengths for the gas and dark matter particles are 0.5 Kpc and 1.0 Kpc, respectively. Since the scale lengths of the thin disk and thick disk component of the Galaxy are 0.3 Kpc and 1.4 Kpc respectively, we can marginally resolve the structure of the thin and thick disk component Also, we can resolve the structure of a bulge ($\sim$ 2 Kpc) in reasonable accuracy. In the previous studies such as Katz (1992) and Steinmetz & Müller (1994, 1995), mainly the structural properties are concerned. In this thesis, we compare the chemical properties of stars with the observational facts of

the Galaxy. We compute the chemical evolution of total metal (Z), iron (Fe) and oxygen (O) in our code and incorporate the recent progenitor model of Type Ia supernovae. The treatment of the chemical evolution in our SPH code is self-consistent. That is, the ejected heavy metal affects the evolution of gases by way of the metallicity dependent cooling.

To model the cosmological galaxy formation, we need to use the physically motivated initial conditions, which is described below. The strategy of our simulations is following: First, we generate many number of a spherical top hat 3 σ over-dense region as Katz (1992). Then we follow the evolution of dark matter particles of these spherical region with a usual N-body code from high redshift. At appropriate redshift, we examine the properties of each halo and select the desired halo for hydrodynamical simulations. After the selection of some halos, we restart the hydrodynamical N-body simulation from the beginning. We will analyze the properties of stellar components and compare the results with the several properties of the Galaxy. If our model galaxy shows similar structures and properties with the Galaxy, we can speculate the formation processes of spiral galaxies.

2. Method

The details of our GRAPE-SPH code are described in Chapter 2. The most important and ambiguous physical process in the formation of stellar systems is the star formation process. In this section we note the star formation algorithm used in this chapter.

In our treatment, the Jeans unstable and cooling region is the place for star formation (Katz 1992). He has added another criterion to the above physical conditions (see section 4.2 of chapter 2 for details) as follows. Within an interval Δt, the probability for star formation can be estimated as

$$P = 1.0 - \exp(-\Delta t / t_{\rm starform}), \tag{4.1}$$

i.e., the star formation process is assumed to be a Poisson process. In our code, we compare P and a random value $(0-1)$ at intervals of Δt. If P is larger than the random value, the star formation occurs. Introducing this "probability criterion", we can control the threshold density for star formation by changing a parameter C (Eq. 2.31 in chapter 2). We compute the P as a function of the density (ρ) for different value of C and present the results in Figure 1. When we compute the P, we assume that $\Delta t = 2.0 \times 10^6$ yr, which is also used in the present calculations. We can interpret the meaning of C as follows:

- larger C means lower threshold density.
- smaller C means higher threshold density.

To summarize, if we use this "probability criterion", the changing of the value of C leads different global star formation history.

Here, we investigate the effect of varying C. We evolve the spherical region of $10^{12}\ M_\odot$, which consists of 10 % gases and 90 % dark matter, with several different star formation parameters C. Initially, we set up the sphere in a rigid rotation and in an outward expansion. The angular speed of the rotation corresponds to $\lambda = 0.05$, where λ is the spin parameter defined as

$$\lambda = \frac{L|E|}{GM^{2.5}}. \tag{4.2}$$

In this definition, L, E, and M are the angular momentum, the total energy, and the mass of the sphere (Padmanabhan 1993). This initial condition is the same as adopted in the simulation of formation of disk galaxies (Katz 1992; Steinmetz & Müller 1995). We evolve the sphere with two different star formation parameters, i.e., $C = 0.1$, 0.5 and 1.0.

In Figure 2, we present the star formation history for $C = 0.1$ and $C = 1.0$. For $C = 1.0$, star formation rates (SFR) increase rapidly than $C = 0.1$. These very old stars in $C = 1.0$ model have large vertical velocity so that the formed galaxy is more extended than $C = 0.1$ as presented in Figure 3. This figure shows the projected edge on surface density of stars at $t = 5$ Gyr. In Table 1, some dynamical properties are compared for different value of C. There is a clear correlation between C and the ratio of X and Z axis velocity-dispersion or the spin parameter. From these results, we conclude that the $C = 0.1$ and $C = 1.0$ galaxies resemble the late type and the early type galaxy, respectively. In these simulations, only one parameter determines the property of the formed galaxy. Such idea, specifically a different type galaxy has a different star formation history, has been discussed from long time ago and used to reproduce some observational properties in the study of the chemical evolution model of galaxies. The time scale of star formation is thought to be a most crucial parameter for determining the morphological difference of galaxies (Noguchi 1998).

The results presented in this section are obtained with small number of particles (the initial number of gas particles ~ 6000) as the previous authors (Katz 1992; Steinmetz & Müller 1995). With such small number of particles, we cannot make detailed comparisons between our results and the several properties of the Galaxy. Thus, in the following sections, we present the Galaxy formation simulation results with much higher resolution. We adopt the $C = 0.1$ to reproduce the Galaxy in the following sections.

3. Initial conditions

The first step is to generate many number of a spherical top hat 3 σ over-dense regions. Each spherical region is generated by the COSMICS package (Bertschinger 1995) with a different seed for the random number generator. The COSMICS package uses the standard Zel'dovich approximation (Zel'dovich 1970; Efstathiou et al. 1985) to compute the displacements and velocities of the dark matter particles from a Gaussian random density field. The power spectrum of this density field represents the CDM spectrum. In the present study, we set the Hubble constant, Ω, and Λ to be 50 km s^{-1} Mpc^{-1}, 1.0 and

0.0, respectively. The density field is normalized by setting the rms density fluctuations (σ_8) smoothed by $8h^{-1}$ Mpc scale at Z = 0.0 to 1.0. The definition of σ_8 is following

$$\sigma_8^2 = \int_0^\infty 4\pi k^2 P(k) W^2(k) dk \tag{4.3}$$

where $P(k)$ is the power spectrum of the density filed and W(k) is the Fourier transform of an appropriate spherical window function of radius = $8h^{-1}$ Mpc. By changing the seed for the random number generator, we can obtain a desired number of density field realizations.

The starting redshift and the mass of the spherical regions are assumed to be ~ 25 and $\sim 1.0 \times 10^{12}\ M_\odot$, respectively. Thus, the comoving radius of the spherical region is $\sim$ 1.4 Mpc. To generate a 3 σ over-dense region, we use the path integral method to generate constrained density field (Bertschinger 1987). We note that there are two methods to set up the over-dense region for an initial condition of cosmological simulations. One is to seek the desired over-dense region by sampling different random filed realizations, which is used by the cosmological hydrodynamical simulations of formation of X-ray clusters (Anninos & Norman 1996). Other is to select the desired halo from the results of the large scale cosmological N-body simulations and use it as an initial condition for a cosmological galaxy formation model (Navarro & White 1994). The path integral method is a fastest method among other methods. In the present study, we generate over 50 density realizations and pick up a spherical region from each realization.

The second step is to follow the evolution of dark matter particles of such over-dense regions using the N-body code. Since we follow the evolution of an isolated spherical region, we make the region in rigid rotations to give a sufficient angular momentum. The typical spin parameter of a virialized halo in CDM cosmology ranges from 0.01 to 0.1 and the average value is 0.05 - 0.07 (Efstathiou & Jones 1979; Barnes & Efstathiou 1987). In the following sections, we set the spin parameter of the selected halo to be 0.1 to model the formation of a spiral galaxy. Also we add the corresponding Hubble velocity to the velocity

field of the sphere since we integrate the equation of motion not in the comoving unit but in the physical units. We use the Remote-GRAPE system or tree method (with $\theta = 1.0$) to follow the evolution of these over-dense regions; there are no differences in accuracies between these methods. The number of particles used in these N-body simulations is $\sim$ 25000, the mass of the particles is $4.0 \times 10^7\ M_\odot$, and the gravitational softening length is 1 Kpc. In both methods, the total energy conserves within 1 % after 3 Gyr of the evolution. At appropriate redshift, we examine the properties of each halo and select the desired halo for a hydrodynamical simulation.

The results of low resolution hydrodynamical simulations presented in the previous section show that the formation epoch of the gas disk is $\sim$ 2 Gyr from the beginning of the simulations. This epoch corresponds to the redshift Z $\sim$ 2.5. Hence, we select the single halo model at Z $\sim$ 2.5. The reason is that if the two dominant halos exist at this time, the disk will be destroyed by the major merger event.

We have selected some single halo models at Z $\sim$ 2.5 from the results of the dark matter particles evolution model. Once we select some halos, we restart the hydrodynamical N-body simulation from Z $\sim$ 25. For the initial condition, we set the gas particles in top of the dark matter particles, i.e., the number of the gas particles is the same as the number of the dark matter particles. As a result, the total number of hydrodynamical simulations is $\sim$ 50,000. The initial velocities of the gas particle are the same with the corresponding dark matter particle. In the hydrodynamical simulations, the baryon fraction is assumed to be 0.1 (i.e., 10 % gases and 90 % dark matter in mass). That is, the initial masses of the gas and dark matter particles in our model are $4 \times 10^6\ M_\odot$ and $3.6 \times 10^7\ M_\odot$, respectively. We set the gravitational softening length for the gas and dark matter particles to be 0.5 Kpc and 1.0 Kpc, respectively. When the star formation occurs, the formed STAR inherits the phase space value (positions and velocities) and gravitational softening length (0.5 Kpc) of

the corresponding gas particle.

4. High resolution simulations of formation of the Galaxy

In this section, we present the results of our high resolution simulations of formation of the Galaxy. Following the method described in the previous section, we select three models (model A, B and C) from 50 spherical regions. Model A and B are single-halo models and Model C is a double-halo model that is selected as a comparison with the models A and B. The results presented in this section are obtained with model A, which is the best model in the present study. We will describe the difference between model A and B in the next section. The comparison between model C and others will be also described in the next section.

4.1. Overall evolution

First, we show the evolutions of dark matter particles in Figure 4. At the beginning of the evolution, the spherical region is expanding due to the Hubble velocity while the small scale structures are growing. There are many small clumps in the first three panels. These small clumps gradually merge to produce the larger clumps. At t $\sim$ 0.3 - 0.5 Gyr, the 3 clumps merge and the resulted clump become the primary halo that eventually becomes a spiral galaxy. After that time, the merging of the smaller clumps to the primary halo continues. At t $\sim$ 1 Gyr, the dark matter is almost virialized and the evolution becomes a quasi-static state as shown in Figure 5. This figure shows the radial density profile of the dark matter particles for the different epochs. The solid line corresponds to $t = 1$ Gyr and other dashed lines correspond to $t = 2$, 3, 4, and 5 Gyr, respectively. The dashed lines are almost indistinguishable.

In Figure 6, we present the evolutions of gas particles. From these plots, we see that the gas disk forms around t $\sim$ 1.8 Gyr. The edge on and face on projected surface density of the gas particles at t = 5 Gyr (Z $\sim$ 0.87) are shown in Figure 7. The spiral structures of the gas disk are clearly shown in Figure 7. Although the entire disk is relaxed to the nearly stable state, the spiral structures are naturally produced by the local gravitational instability (Binney & Tremaine 1987). Figure 9 shows the unstable region in the gas disk. In this figure, the region where the Toomore's Q value is greater than 1.0 is shown in red. The Toomore's Q value is defined as

$$Q = \frac{2c_s\Omega}{\pi G\Sigma}, \tag{4.4}$$

where c_s is the sound velocity, Ω is the angular speed, and Σ is the surface density of the gas (Binney & Tremaine 1987).

The SFR as a function of time is plotted in Figure 10. The first star formation occurs at t $\sim$ 0.015 Gyr. Within first 0.15 Gyr, the SFR remains low value. After t $\sim$ 0.015 Gyr, the SFR increases with time and become maximum at t $\sim$ 0.4 Gyr. This time corresponds to the time of the largest merger event. After that time, the SFR gradually decreases and eventually become almost constant ($\sim 2\ M_\odot\ \mathrm{yr}^{-1}$) after t $\sim$ 3 Gyr. This constant star formation mainly occurs in the gas disk. The resulted stellar surface density is presented in Figure 8. As Figure 7, the edge on and face on projected surface density of the star particles at t = 5 Gyr are presented. The Figure 8 matches the real image of the Galaxy and, the stellar disk and bulge are clearly shown.

To investigate the properties of different stellar component, we categorize stars into three groups; disk stars, halo stars, bulge stars. The stars are categorized by following simple conditions.

- bulge stars : R $<$ 2 Kpc

- disk stars : R $<$ 10 Kpc and |Z| $<$ 2 Kpc

- halo stars : R $>$ 2 Kpc and |Z| $>$ 2 Kpc

We use the position of the stars at $t = 5$ Gyr in applying these conditions. The resulted number of STAR particles and mass for each component are summarized in Table 2.

Three components show the different kinematics as shown in Figure 11. This figure shows the distribution functions of the velocity for each component. The halo stars have a wider distribution than other two components. The peaks of these distribution functions for the disk ($\sim$ 270 km s^{-1}) and bulge stars ($\sim$ 180 km s^{-1}) almost correspond to the rotational velocity for each component. There is a difference in the formation history of each component. Figure 12 shows the SFR as a function of time for each component, which is normalized by the total mass of the component. The stars categorized to bulge stars form earlier than others. We will return to this point in the next subsection. After $t \sim 2$ Gyr, the most star formation occurs in the gas disk and become quasi-statically. The SFR in the disk after $t \sim 2$ Gyr is $\sim 2\ M_\odot\ \mathrm{yr}^{-1}$, which is larger than the observed current SFR ($\sim 1\ M_\odot\ \mathrm{yr}^{-1}$) in the galactic disk.

We compare the metallicity distribution function for each component in Figure 13. In this figure, if the metallicity of stars is smaller than [Fe/H] $= -5$, such stars are categorized in the lowest bin, i.e., the lowest bin includes the metal-free stars. The bulge stars show the wide metallicity distribution function as observed. We see that the distribution function of the halo stars is more metal-poor than other components. Also, the halo component contains many metal-free stars. These metal-free stars is the first generation star (Population III stars) at each clump. The formation epoch of the metal-free stars is early so that the position of these stars is at at high latitude. For the disk component, the peak of the distribution function is almost solar value as observed.

From these results, we conclude that we obtain the stellar system that is very similar to the Galaxy. If we categorize the stars using the information of the chemical properties and the formation epoch (t_{form}) of stars, the three components of the Galaxy are more clearly shown. In Figure 14, we present a such result. The left, center and right panels of this figure show the stars categorized by the following conditions:

- left : Metal-poor ($Z/Z_\odot < -3$) stars

- center : Old ($t_{form} < 1$ Gyr) and metal-rich ($Z/Z_\odot > 0$) stars

- right : Young ($t_{form} > 4$ Gyr) stars

Metal-poor stars show the extended distribution since such stars formed at an early epoch and the star formation occurred at high latitude. The old and metal-rich stars are concentrated in the galactic center. This point will be concerned in the next subsection. Since the young stars are located near the galactic plane, the most recent star formation occurs in the disk.

4.2. Formation of the bulge

There are several scenarios for the formation processes of a bulge component of spiral galaxies (Bouwens, Cayon, Silk 1999). Such scenarios can be divided into three categories as: 1. the merging of sub-clump in the proto-galactic cloud, 2. the secular evolution of the stellar disk, and 3. the in-fall of dwarf galaxies.

The galactic bulge is thought to form by rapid star formation. Matteucci & Brocato (1990) and Matteucci, Romano, & Molaro (1999) proposed that the chemical evolution model of the galactic bulge and obtain the following results: the galactic bulge forms by the star burst, the time scale of which is $\sim$ 1.0 Gyr. One of the predictions of their results

is that the element ratio such as [O/Fe] remains high for metal-rich stars because of the short formation time scale of the bulge. Due to the delay of Type Ia supernovae explosion, the metallicity of the bulge stars is mainly originated in Type II supernovae. The one-zone chemical evolution model as Matteucci, Romano, & Molaro (1999) can predict the chemical properties of the galactic bulge, however, the chemical and dynamical model is required to predict the dynamical properties of the bulge. In this subsection, we use our high resolution formation model of the galaxy to study the formation of the galactic bulge.

As presented in Figure 12, the over 60 % stars located near the galactic center formed during first 0.5 Gyr of the evolutions. Figure 15 shows that the stellar density plots of first 0.5 Gyr. The two clumps merge during t = 0.4 - 0.5 Gyr. This merging of the clumps causes the star burst as shown in the SFR plots (Figure 10). The estimated formation time scale ($\sim$ 0.5 Gyr) is shorter than the chemical evolution model of the bulge by Matteucci, Romano, & Molaro (1999).

According to the prediction of Matteucci, Romano, & Molaro (1999), we select the true bulge star from the stars near the galactic center (R $<$ 2 Kpc) by the following conditions:

- [Fe/H] > -2 and [O/Fe] > 0.3

The mass and number of the true bulge stars are 1.3×10^{10} $M_{\odot}$ and 8,891, respectively.

We compare the metallicity distribution of these stars with the observation of K-giant stars McWilliam & Rich (1994) in Figure 16. Our results reproduce the wide metallicity distribution of the bulge stars. This wide distribution is caused by the strong star burst. However, the number of metal-rich stars ([Fe/H] > 0) in our model is fewer than the observation. This result is expected since the best fit model of Matteucci, Romano, & Molaro (1999) is that there are more massive stars than the IMF used in our code. Our

model adopt the the power-low type IMF as

$$\phi(m) = Am^{-x}, \tag{4.5}$$

where x the index of the IMF and we set $x = 2.35$ in the present study. In Matteucci, Romano, & Molaro (1999), they reported that the peak metallicity of the distribution function in their model depended on the value of x. To match the observation of McWilliam & Rich (1994), they concluded that the allowed range of x was 2.1 - 2.35. Thus, by changing the shape of the IMF and/or adopting a time-dependent IMF are possible solutions of the problem that there are fewer number of metal-rich stars in our model. In the current model, the parameter related to this problem is the size of the feedback radius (R_f). We will return to this point in the next section.

In Figure 18, we plot the average velocity and the velocity dispersion of the bulge stars. The bulge stars are substantially rotationally supported as the galactic bulge. The rotational speed of the bulge stars is $\sim$ 160 - 230 km s^{-1}, which is smaller than the rotational speed of the disk stars ($\sim$ 270 km s^{-1}). This means that the angular momentum of the bulge is lost during merging process. Figure 19 compare the mean velocity dispersion for the bulge stars as a function of [Fe/H] with the observational results of Minniti (1996). Except the metallicity range [Fe/H] = $[-1, 0]$, our model is similar to the observation.

Our model reproduce the chemical and the dynamical properties of the galactic bulge. We conclude that the galactic bulge has formed by the sub clump merger in the proto galaxy. The merger event causes the star burst and such high SFR is responsible for the wide range metallicity distribution of the observed bulge stars.

4.3. Properties of the disk stars

In this subsection, we show the properties of the disk stars in our model.

The stellar surface density of the disk stars shows the exponential profile as shown in Figure 20. The scale length of the stellar disk at $t = 5$ Gyr is ~ 5.0 Kpc. This value is little larger than the observed scale length of the Galaxy.

Yoshii & Sommer-Larsen (1989) argued that the exponential surface profile observed in disk galaxies can be naturally explained by the viscous evolution in the gas disk. They have shown that the exponential profile is obtained if the viscous time scale is comparable to the star formation time scale. One of the physical mechanisms that produce the viscous evolution in a gas disk is the local gravitational instability (Toomre 1964). Since the star formation processes are also related to the gravitational instability in the gas disk, the assumption that the viscous time scale is comparable to the star formation time scale is plausible (Yoshii & Sommer-Larsen 1989). The viscous angular momentum transfer redistributes the angular momentum in the gas disk. After the viscous evolution, the gas disk shows the exponential profile and the rotational velocity of the disk shows a flat rotation curve. If the effect of the star formation is incorporated, the results are not changed Saio & Yoshii (1990). As shown in the Figure 9, the gravitational instability occurs in our numerical simulations. We note the numerical angular momentum transfer. We adopt the shear free viscosity formulation as described in Section 2. Navarro & Steinmetz (1997) have presented the numerical experiments of the effect of the numerical angular momentum transfer. They evolved the gas disk with different formulation of an artificial viscosity term and traced the changes of half angular momentum radius (R_J : the angular momentum inside R_J equals to the half of the total angular momentum of the disk). The R_J is changed by factor of two if the standard artificial viscosity term is used. On the other hand, there was no violent angular momentum transfer due to the shear free artificial viscosity term within the Hubble time. Consequently, the adoption of the shear free artificial viscosity formulation suppresses the numerical angular momentum transfer. Thus, we conclude that the viscous evolution of the gas disk occurs in our numerical model. Such evolution in the

gas disk produce the exponential profile of the stellar disk.

In Figure 21, we present the relation between the metallicity and the radius within the disk. The solid dots represent our result and the straight line shows the observed gradient (~ -0.065 dex Kpc^{-1}) in Maciel & Quireza (1999). This observed gradient is obtained by averaging the disk planetary nebulae, HII regions, and young stars observations. There is a spread in the observed relation and the spread is ~ 1.0 dex. Although such spread cannot be reproduced by the one-zone chemical evolution model, our result shows the spread as the observation. Since the solid dots in Figure 21 are the averaged value at each location, the spread (~ 0.5 dex) is smaller than the observation. The true dispersions at each location range from 0.5 - 1.3 dex.

We select the solar cylinder stars from disk stars and compare the properties with observations. The solar cylinder stars are defined as

- $7 < R < 8$ Kpc and $|Z| < 1.5$ Kpc.

In Figure 22, we compare the metallicity distribution function with the observed one of Edvardsson et al. (1993). In our results, there are more metal-poor stars than the observation. The fraction of stars that is metal poorer than [Fe/H] < -1.0 is ~ 10 % in our model. The fact that there are few metal-poor stars near the sun is called "G-dwarf" problem. Although the standard one-zone chemical evolution model predicts the half of the stars is metal poorer than [Fe/H] < -0.5, only 2 % of the stars near the sun are metal poorer than [Fe/H] < -0.6 (Sommer-Larsen 1991). This failure originates from the incorrect assumptions used in the standard one-zone chemical evolution model. These assumptions are that 1: the gas is initially metal-free, 2: closed box model and 3: constant yield. The assumption that the chemical evolution near the sun proceeded in a closed box manner is thought to be incorrect. While the gas disk forms, the star formation in the disk

occurs and the chemical enrichment near the sun proceeds. That is, the in-fall of gases occurred in the dynamical picture of the formation of the Galaxy (Larson 1972). If we incorporate the in-fall of gases into the chemical evolution model, the "G-dwarf" problem is resolved (Pagel 1997). Another possibility is proposed that the metal-enriched gases are ejected by the galactic wind due to the bulge formation (Köppen & Arimoto 1990). This means that the pre-enrichment has occurred before the formation of the gas disk (Truran & Cameron 1971).

In our dynamical and chemical model, the in-fall and the pre-enrichment of gases are properly treated within the numerical accuracies. Although we use the fixed metallicity yield as the one-zone chemical evolution model, this is not critical to the "G-dwarf" problem. To solve the "G-dwarf" problem in our model, the gases should be more metal rich before the gas disk formation. Thus, a parameter related to the "G-dwarf" problem in our model is the size of the feedback radius (R_f) as noted before in section 4.2. The results presented in this section are obtained with $R_f = 0.5$ Kpc. This value is same value as the gravitational softening length since the numerical resolution in our code is limited by the gravitational softening length. We will return to this point in the next section.

Figure 23 shows the relations between [O/Fe] and [Fe/H] for the solar cylinder stars. The solid dots are our result and the white squares are the observational data from Nissen et al. (1994); Edvardsson et al. (1993); Gratton (1991); Barbuy & Erdelyi-Mendes (1989). Our results match the observation quantitatively. In our results, the turn over due to the Type Ia supernova explosion is obvious. The upper limit of [O/Fe] for the metal-poor regime comes from the use of the fixed metallicity yield and the value corresponds to the ratio between Fe and O Table 1 in Chapter 2. Due to the instantaneous recycling approximation adopted in the standard one-zone chemical evolution model, such an one-zone model cannot produce the observed dispersion in the relation between [O/Fe] and [Fe/H]. In contrast, our

model shows the dispersion of [O/Fe] vs. [Fe/H] relation.

Figure 24 shows the age-metallicity relation for the solar cylinder stars. The observed relation of Edvardsson et al. (1993) is shown in the white squares. Our results are almost consistent with the observation except in the metal-poor regime.

From the various comparison between numerical results and the observational data, we conclude that our model can quantitatively reproduce the chemical properties of the disk stars. However, the "G-dwarf" problem is not completely solved in the current model. By choosing different feedback radius may be the solution to this mismatch.

4.4. Properties of the halo stars

The properties of halo stars are well observed by the halo globular clusters. From such observations, the stellar density profile of the halo is expressed to be $\propto r^{-3.5}$ (Harris 1976). The comparison between our numerical result and this fact is shown in Figure 25. The stellar density of our model is well fitted by the observed profile. We infer that the halo field stars and the halo globular clusters are the same populations. In chapter 3, we present the simulation of the globular cluster formation and conclude that the globular cluster formation is not efficient in the proto-galactic environment. Namely, the failed globular clusters may become the field halo stars. This speculation is supported by our numerical model.

From the observation of the metallicity of the halo globular clusters, there is no correlation between the metallicity of a star and its position (Searle & Zinn 1978). From this fact, they have concluded that the formation of the Galaxy is not the ordered collapse as proposed by Eggen, Lynden-Bell, & Sandage (1962). In the CDM scenarios, the structure formation proceeds stochastically. Thus, the structure formation in the CDM

scenario predicts that no correlation between the metallicity of a star and, its position and kinematics.

The result of our model is shown in Figure 26 and 27. By integrating the orbit of randomly selected stars, we estimate eccentricity of the stars as Chiba & Yoshii (1998). In Chiba & Yoshii (1998), they present the distribution function of the eccentricity of the sample stars, which have the precise proper motion obtained by the *Hippaarcos* astrometry satellite. We integrate the orbit of the selected stars in the fixed potential of the dark matter particles. From the orbit of the stars, the eccentricity (e) is estimated as

$$e = \frac{r_{\rm max} - r_{\rm min}}{r_{\rm max} + r_{\rm min}}, \tag{4.6}$$

where the $r_{\rm max}$ and $r_{\rm min}$ are the maximum and minimum distances from the galactic center. The left panel of Figure 26 shows the relation between the estimated e and the metallicity ($[{\rm Z/Z_\odot}]$). The right panel of Figure 26 shows the relation between the estimated e and the $r_{\rm max}$. As expected, there is no correlation between the eccentricity and other quantities. Figure 27 shows the normalized e-distribution function for the halo stars. The metal-rich stars ($-2 < [{\rm Z/Z_\odot}] < -1$) contain more fraction of high eccentric stars than metal-poor stars ($[{\rm Z/Z_\odot}] < -3$). This trend is reported in Chiba & Yoshii (1998). Thus, the kinematics of the halo stars in our model are qualitatively similar to the halo stars of the Galaxy.

5. Discussion

5.1. Dependence on the initial conditions

The initial condition used in the previous section is selected by the following strategy. We generate about 50 density field realizations and pick up a spherical region from the realization. Then we follow the N-body evolution of the dark matter particles. From the result of the evolution of the dark matter particles, we select the single halo model at Z $\sim$

2.5. 39 of realizations are the single halo model and others are the multiple halo models. Thus, there are many number of candidates for the initial condition. As noted previously, we select three models (model A, B and C) from 50 spherical regions. Model A and B are single-halo models and the results presented in the previous section are obtained with the model A. Model C is a double-halo model that is investigated as a comparison with the models A and B. Figure 28 show the projected dark matter density at Z $\sim$ 2.5 for the three models.

We compare the SFR as a function of time for these three models in Figure 29. The evolution of first 1 Gyr reflects the different merging history of each model. For the single-halo models (model A and B), the evolution of SFR after the disk formation around $t \sim 2$ Gyr is quasi-static since the star formation mainly occurs in the disk plane. On the other hand, the SFR of the double-halo model (model C) increase at $t \sim 4$ Gyr. This increase in the SFR is caused by the merging of two halos. To clearly see the early merging history of each model, we select stars located near the galactic center (R $<$ 2 Kpc), which are the spherical component as the galactic bulge, plot the star formation history for these stars in Figure 30. The resulted number of STAR particles and mass for each model are summarized in Table 3. As shown in Figure 29, each model shows different star formation history. The model A rapidly reaches the peak value at $t \sim 0.4$ Gyr. This peak corresponds to the merging event as noted in Section 4.2. In contrast, the model B shows comparable peak value twice at $t \sim 0.5$ and 0.9 Gyr. This means that the model B is more clumpy initial condition than the model A. The SFR for the model C increases most slowly and become almost constant around $t = 0.5$ - 1.2 Gyr.

It is interesting to see the metallicity distribution function for these central stars. In Figure 31, we show the metallicity distribution function for each model. Qualitatively speaking, all models show the wide distribution function as the galactic bulge in spite

of the very different star formation history. As noted previously (Section 4.2), a strong star-burst caused by sub-galactic mergers produces the wide distribution function. This process is natural consequence of the CDM initial condition. However, the position of the peak value reflects the different star formation history. Specifically, the model A shows double peak distribution in contrast with other models. This double peak is explained by the chemical enrichment due to Type Ia supernova explosions. In Figure 32, we separately plot the distribution function of the very old stars ($t < 0.5$ Gyr) and other stars. In the present model, the first Type Ia supernova occurs $t \sim 0.5$ Gyr (see Figure 5 of Chapter 2). Hence, the stars that are younger than $t \sim 0.5$ Gyr are chemically contaminated by Type Ia supernovae. Namely, the higher peak ([Fe/H] ~ 0.3) is responsible for the stars that have contaminated by Type Ia supernovae. In the model B and C, the time duration of the star formation is longer than the model A so that the double peak is not achieved. From these results, we expect that if the formation time scale of the galactic bulge is shorter than 0.5 Gyr, the distribution function shows a double peak distribution. Actually, the current observed distribution function of the bulge (McWilliam & Rich 1994) is a double peak. However, this point needs more observation using a 8-m class telescope. Also, the time scale of first Type Ia supernovae from the star formation ($t_{\rm SNIa}$) is still ambiguous since the progenitor model of Type Ia supernovae is controversial (Branch et al. 1995). Using the chemical evolution model in the solar neighborhood, Yoshii Tsujimoto & Nomoto (1996) concluded that the range is confined within $t_{\rm SNIa} = 0.5$ - 3 Gyr. We note that our value of $t_{\rm SNIa} = 0.5$ Gyr is shorter than the value (~ 1 Gyr) adopted in Matteucci, Romano, & Molaro (1999).

As a result of the different evolution, each model shows a different stellar structure as presented in Figure 33. The upper panels of Figure 33 show the projected surface density of gases for each model. Although the model A and B have the gas disk, there is no gas disk in the model C. When we compare the model A and B, the gas disk of the model A is

thiner than the model B. Although both models are the single-halo model, the evolution of the model A is less stochastic than the model B. For the model B, the time scale of global star formation is shorter than the model A as shown in Figure 34. This figure shows the mass fraction of gases in the total baryon mass as a function of time for the model A (solid line) and B (dashed line). The gas fraction of the model B reaches the plateau value around $t = 2$ Gyr. In contrast, the model A takes long time, ~ 4 Gyr, to reach the plateau value. Namely, the consumption of gases in the model B is rapid due to the more frequent mergers than the model A. Hence, the model A shows the prominent gas and the stellar disk as shown in the lower panels of Figure 33. This figure presents the projected surface density of stars for each model. The resulted stellar system of the model B and C show more spherical shape than the model A. These results are caused by the several merging event during the evolution. The difference between the model B and C is whether the gas disk exists.

To summarize, each model shows a different gas and stellar structure as a consequence of a different evolution history, i.e, a merging history. We can state that each model A, B, C correspond to a spiral galaxy, an elliptical galaxy that has a gas disk, and a normal elliptical galaxy. The merging history of the model depends on the typical initial conditions. That is, the numerical results like presented here strongly depend on the initial conditions. In other words, the variety of the galaxy morphology might be naturally explained by the variety of the initial conditions. We note that the ignored physics in the present study, such as the effect of external tidal field and/or radiation fields, also affect the determination of the morphology of galaxies.

5.2. Dependence on numerical parameters

There are a number of numerical parameters in the present numerical model. In this thesis, we mainly concern the chemical properties of the stellar components so that we

only investigate the influence of the feedback parameter R_f to the chemical properties of stars. As noted in section 4.2 and 4.3, the mismatch between the numerical results and the observations may be solved by changing the size of R_f. We expect that a larger R_f leads the formation of more metal-rich stars. To see how the size of R_f affects the results, we redone the calculations of model A with larger $R_f = 0.8$ Kpc. The result for $R_f = 0.8$ Kpc model is almost indistinguishable from $R_f = 0.5$ Kpc model. Figure 35 compares the metallicity distribution function of solar cylinder stars for $R_f = 0.5$ Kpc, $R_f = 0.8$ Kpc and the observed one of Edvardsson et al. (1993). The fraction of the stars around [Fe/H] $= -0.6$ increases a little. Also, the fraction of the stars that is more metal-rich than [Fe/H] ~ -0.2 is not much changed. Since the gas particles in the SPH method are concentrated in the high density regions, merely increasing the feedback radius does not drastically affect the chemical enrichment history. Hence, the adoption of $R_f = 0.5$ Kpc, which equals to the gravitational softening length, is optimal choice of the current model. From this fact, we expect that more high resolution model is required to qualitatively model the chemical properties of the Galaxy.

5.3. Comparison with previous results

In the previous studies, such as Katz (1992) and Steinmetz & Müller (1994, 1995), various structural properties are mainly concerned and their results are almost consistent with the structural properties of the Galaxy. However, those previous studies lack the proper treatment of the chemical evolution. In this chapter, we mainly compare the chemical properties of stars with the observational facts of the Galaxy because our numerical code treat the chemical evolution of the gas properly. In our code, the chemical evolution model incorporates the effect of stellar winds, Type II supernovae, and Type Ia supernovae and we follow the chemical evolution of total metal (Z), iron (Fe) and oxygen (O). The first

proper treatment of chemical evolution in the SPH method is demonstrated in Raiteri, Villata, & Navarro (1996). They model the formation of the Galaxy and compare the chemical properties of stars with the observational facts of the Galaxy. Their model uses even smaller number of particles than Katz (1992).

Navarro & White (1993) investigated the dependence on the various numerical parameter in SPH simulations. By computing the adiabatic collapse of a gas sphere with different number of particles, they concluded that at least 300 particles are required to properly model the formation of galaxies. This conclusion is applicable to the dynamics of the model. Hence, the smaller number of particles used in the previous studies like Katz (1992) is sufficient because they only concern the dynamical properties of spiral galaxies. However, the high resolution is essential for the chemical evolution in the numerical model like ours. The reason is that the actual feedback radius is comparable to the radius of the supernova remnants (< 100 pc). Although whether the resolution used in the present model is sufficient is not known, the results presented in this chapter are the first high resolution three-dimensional chemical and dynamical model of the Galaxy. The results presented in the previous section show that the number of chemical properties of the Galaxy can be reproduced by our numerical model. If we want to obtain more quantitatively similar model to the Galaxy, we have to investigate the wide range of numerical parameters and/or the initial conditions.

Navarro & White (1993) reported that the energy feedback scheme strongly affects the result of the calculations. In their method, the energy ejected by stars is distributed to neighbor gas particles mostly as a thermal energy and the rest is distributed as a velocity perturbation to the gas particles; the fraction of the energy in a kinetic form ($f_{\rm kin}$) is a free parameter. They simulate the formation of a galaxy with the SPH method that incorporates the star formation recipes. In their results, the resulted stellar mass strongly depend on the

value of $f_{\rm kin}$; the stellar mass is changed by factor of ten. In our GRAPE-SPH code, the ejected energy by stars is distributed to neighbor gas particles in a pure thermal energy. That is, we set $f_{\rm kin} = 0$ in the present study. This is because the size our numerical model are smaller than those of Navarro & White (1993). To see how the specific energy feedback scheme affect results, we will require a higher resolution model. Also, higher resolution model will be required to properly model the detailed structure of the Galaxy such as the formation and evolution of the thin disk component (the scale length of the thin disk of the Galaxy is ~ 0.5 Kpc).

6. Summary

In this chapter, we present the results of high resolution simulations of the formation of the Galaxy.

First, we introduce the "probability criterion" and explain the meaning of the star formation parameter C. From the definition of C, we can interpret the meaning of C as follows:

- larger C means lower threshold density.
- smaller C means higher threshold density.

Namely, the changing the value of C may lead different global star formation history. To see how C affects a star formation history, we evolve a spherical top hat over-dense region of mixture of dark matter and gases with different values of C. The result of the calculations indicates that $C = 0.1$ and $C = 1.0$ galaxy resemble the late type and the early type galaxy, respectively. Changing the star formation parameter C leads the different structure and the kinematics of the resulted galaxies. The used number of particles in these calculations is

too small to make detail comparisons between our results and the several properties of the Galaxy. In particular, to properly model the chemical evolution of the Galaxy, we have to use larger number of particles. Thus, we have done the much higher resolution simulations of formation of the Galaxy as follows.

To efficiently generate the proper initial conditions, we adopt the path integral method to generate a 3 σ over-dense region. We compute 50 over-dense spherical regions and follow the dark matter evolution of each sphere. At appropriate redshift, we examine the properties of each halo and select the desired halo for hydrodynamical simulations. The results of low resolution hydrodynamical simulations indicate that the formation epoch of the gas disk is ~ 2 Gyr ($Z \sim 2.5$) from the beginning. We select the single halo model at $Z \sim 2.5$ since if the two dominant halos exist at this time, the disk will be destroyed by the major merger event. We select two single-halo model (model A and B) and one double-halo model (model C) as a comparison. Once we select some halo model, we restart the hydrodynamical N-body simulation from $Z \sim 25$.

Then, we present the result of the evolution of model A and the detailed comparison between the model galaxy and the number of observational facts of the Galaxy. By categorizing the stellar components with the metallicity and age, our model galaxy consists of three components as the Galaxy. Each stellar component shows quantitatively similar properties with the Galaxy.

The early evolution of model A reveals that the most bulge stars form during the merger event that occurred in the region of deepest potential. As a result of the strong star burst induced by the merger, the metallicity distribution of the bulge component become wide as the observation. From this result, we conclude that the galactic bulge can be formed by the sub clump merger in the proto galaxy.

For the disk stars, the age-metallicity relation and the metallicity gradient of our

numerical model match very well with the observation. However, the metallicity distribution function of our results shows too much metal-poor stars than the metallicity distribution function for solar neighborhood stars. The projected surface density of disk stars is well fitted by the exponential profile. Such exponential profile might be produced by the viscous evolution in the gas disk.

For the halo stars, the density profile of the halo stars shows $r^{-3.5}$ profile as the observed density profile of the halo globular clusters. As expected from the structure formation in the CDM scenario, there is no correlation between the metallicity of a star and, its position and kinematics. The distribution function of the estimated eccentricity of the halo stars is qualitatively similar to the observed distribution function. We conclude that the kinematics of the halo stars are qualitatively reproduced by our numerical model.

To summarize, our high-resolution numerical model of the Galaxy reproduces the number of observational properties of the Galaxy. In particular, the formation processes of the galactic bulge is naturally explained in the CDM cosmology. However, our model galaxy has too much metal-poor stars than the Galaxy. The reasons for this mismatch with the observations are either a specific initial condition and/or the incorrect numerical modeling. To discriminate the origin of the mismatch, we will have to construct the even higher resolution model and explore the parameter space of several numerical parameters.

Table 1. Dynamical properties of the model galaxies.

C[a]	(σ_z/σ_x)[b]	spin (λ)	stellar mass [c]
0.1	0.587	0.70	$4.2 \times 10^{10}\ M_\odot$
0.5	0.710	0.52	$5.4 \times 10^{10}\ M_\odot$
1.0	0.771	0.44	$4.6 \times 10^{10}\ M_\odot$

Note. — [a] C represents the star formation parameter.

[b] This column shows the ratio of X and Z axis velocity dispersion.

[c] The stellar mass at $t = 5.0$ Gyr.

Table 2. The number of STAR particles and mass for each component for the model A.

Component	Number	Mass	Averaged mass
halo	17,900	$1.29 \times 10^{10}\ M_{\odot}$	$7.20 \times 10^{5}\ M_{\odot}$
disk	36,848	$2.06 \times 10^{10}\ M_{\odot}$	$5.58 \times 10^{5}\ M_{\odot}$
bulge	16,219	$1.74 \times 10^{10}\ M_{\odot}$	$1.07 \times 10^{6}\ M_{\odot}$

Table 3. The number and mass of STAR particles near the galactic center for the three models.

Model	Number	Mass	Averaged mass
A	16,191	$1.74 \times 10^{10}\ M_{\odot}$	$1.07 \times 10^{6}\ M_{\odot}$
B	19,038	$3.11 \times 10^{10}\ M_{\odot}$	$1.63 \times 10^{6}\ M_{\odot}$
C	22,561	$2.70 \times 10^{10}\ M_{\odot}$	$1.20 \times 10^{6}\ M_{\odot}$

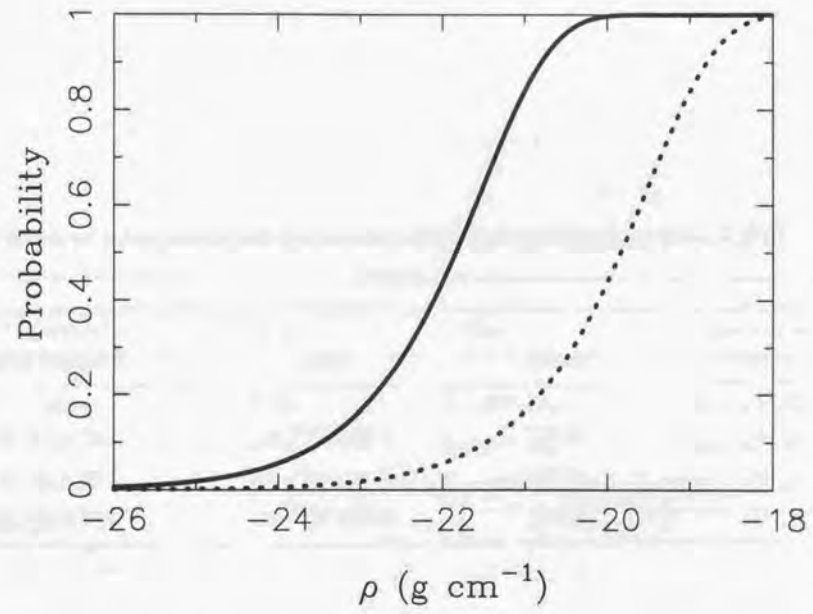

Fig. 1.— The star formation probability (P) as a function of density of gases. The solid and dashed lines correspond to "C = 1.0" and "C = 0.1", respectively.

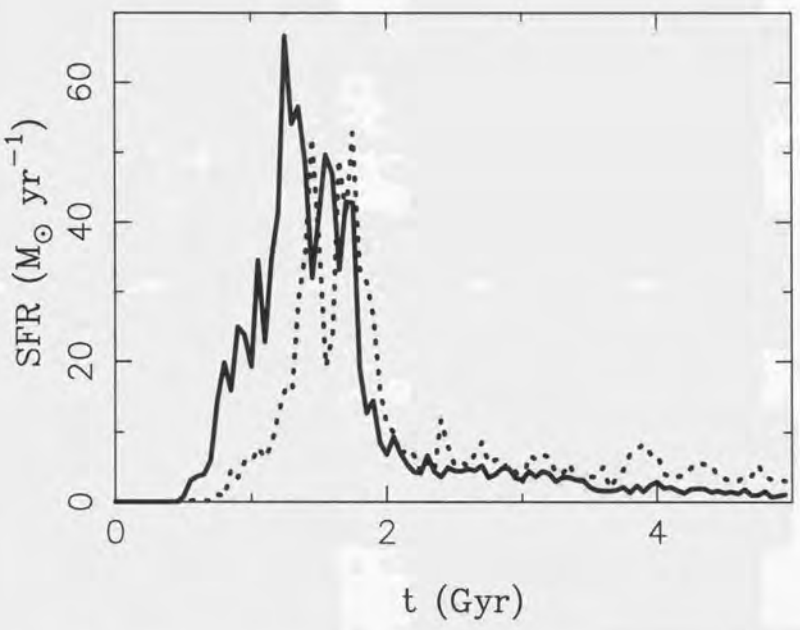

Fig. 2.— The SFR as a function of time for $C = 0.1$ and $C = 1.0$ galaxies. The dotted and solid lines correspond to $C = 0.1$ and $C = 1.0$, respectively.

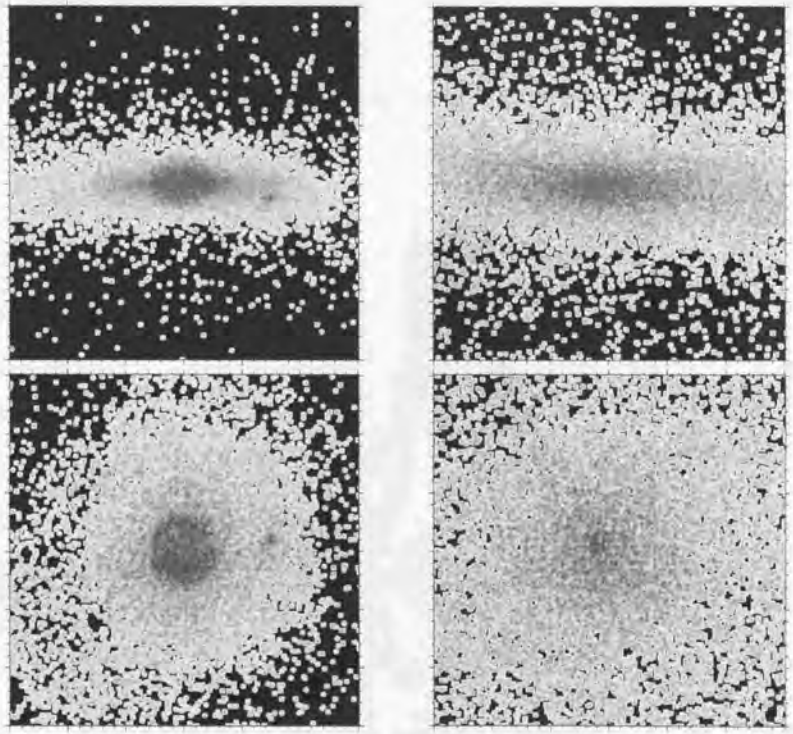

Fig. 3.— The projected surface density of stars for $C = 0.1$ (left panels) and $C = 1.0$ (right panels). The upper and lower panels correspond to the edge on view and face on view, respectively. The size of the panel is 20 kpc × 20 kpc.

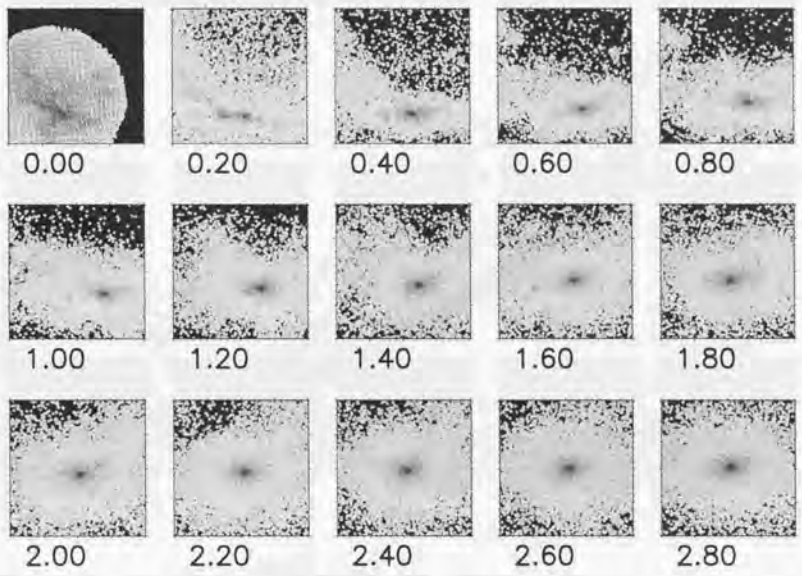

Fig. 4.— The evolution of the dark matter particles (projected to X-Z plane). The number located at the bottom of the each panel is the elapsed time from the beginning of the evolutions in 0.1 Gyr. The size of the all panels is 100Kpc × 100Kpc.

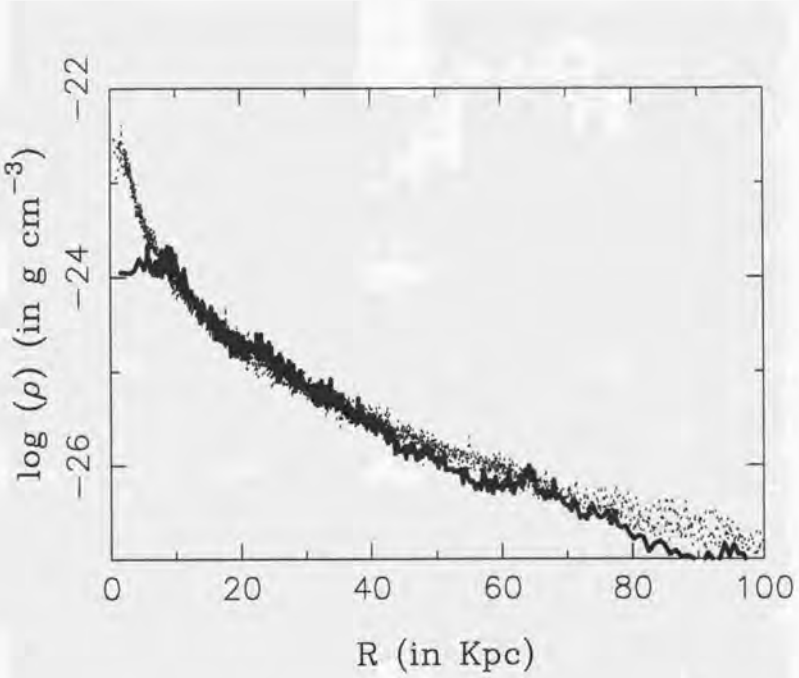

Fig. 5.— This figure shows the radial density profile of the dark matter particles for different epochs. The solid line corresponds to $t = 1$ Gyr. The other lines correspond to $t = 2$, 3, 4, and 5 Gyr.

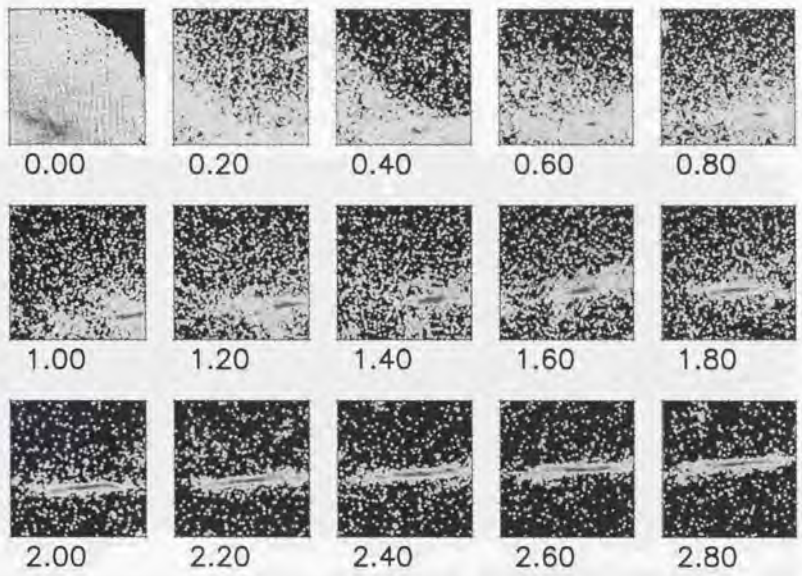

Fig. 6.— The evolution of the gas particles (projected to X-Z plane). The number located at the bottom of the each panel is the elapsed time from the beginning of the evolutions in 0.1 Gyr. The scale of the panel is changed from the top row to the third row. From the top, the panel in the each row corresponds to 70Kpc × 70Kpc, 50Kpc × 50Kpc and 30Kpc × 30Kpc.

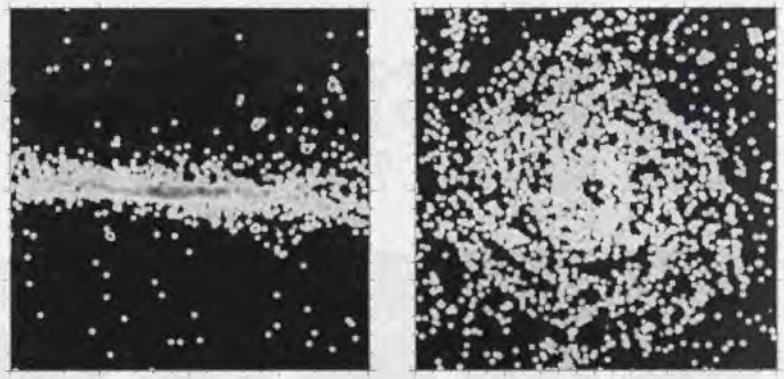

Fig. 7.— The projected gas density image at $t = 5$ Gyr. The left and right panel shows the edge on and face on view, respectively. The size of the panel is 20Kpc × 20Kpc.

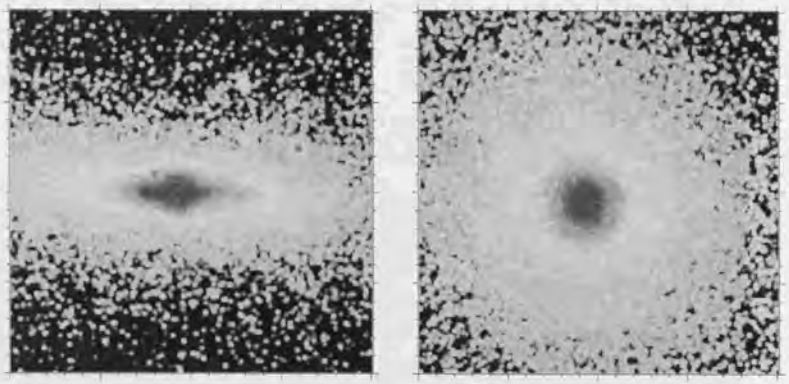

Fig. 8.— The projected stellar density image at $t = 5$ Gyr. The left and right panel shows the edge on and face on view, respectively. The size of the panel is 20Kpc × 20Kpc.

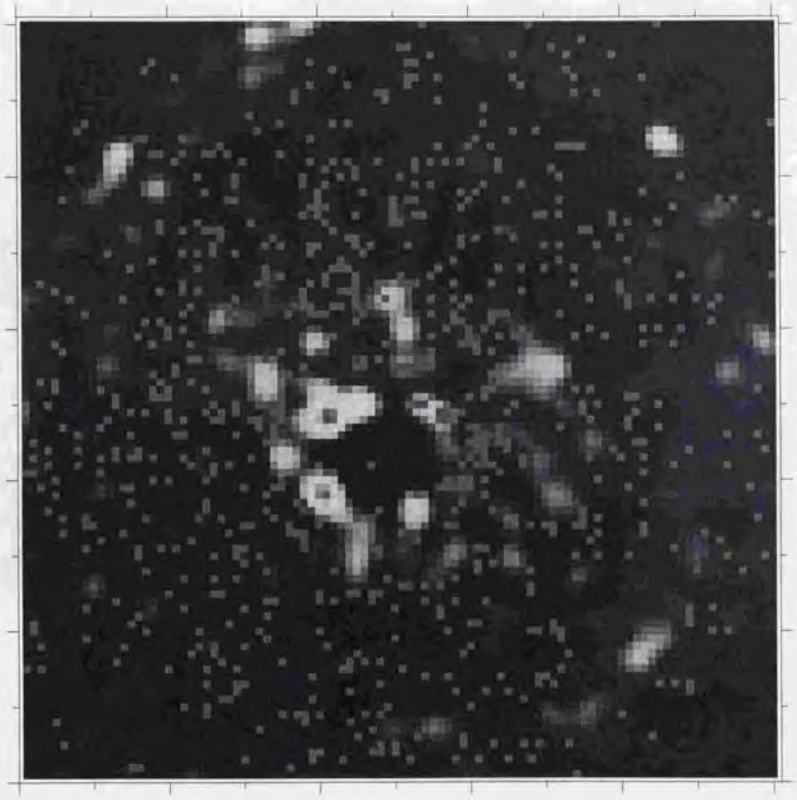

Fig. 9.— The gravitationally unstable region within the gas disk is shown in red. The size of the panel is 10Kpc × 10Kpc.

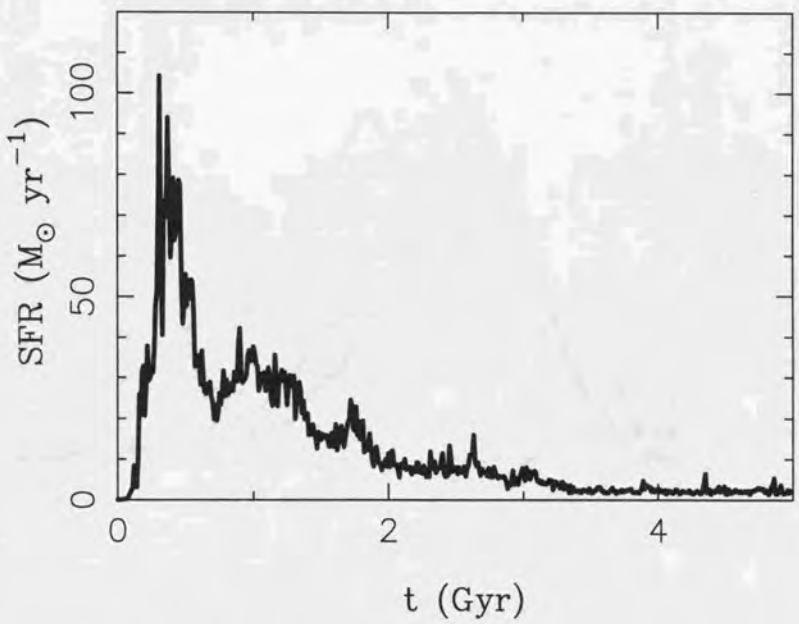

Fig. 10.— The total SFR as a function of time.

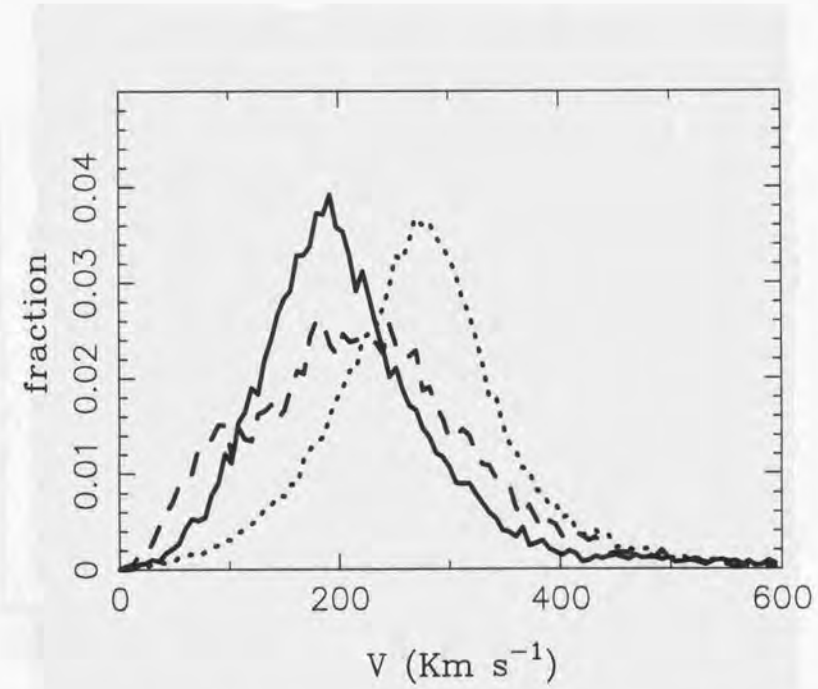

Fig. 11.— The velocity distribution function for three populations is shown. The solid, dashed and dotted lines correspond to the bulge, halo and disk stars.

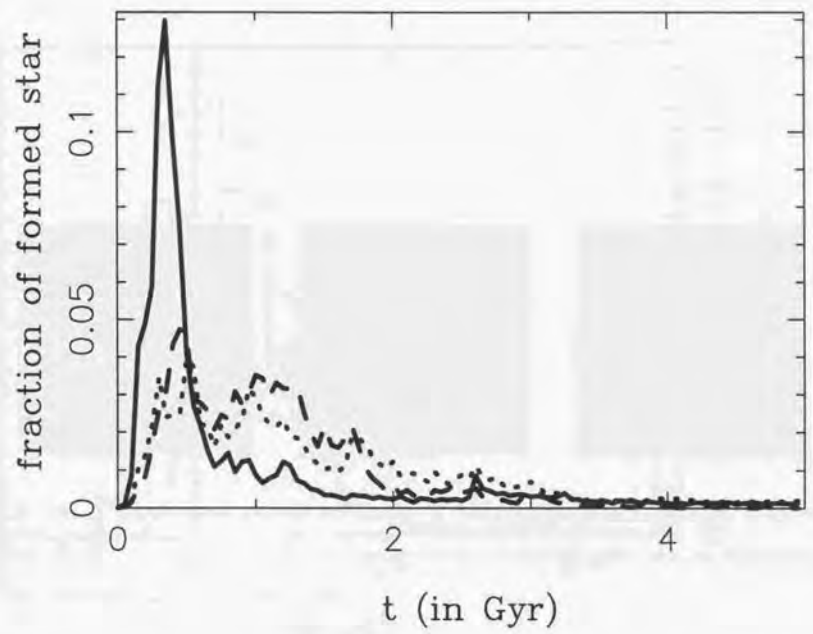

Fig. 12.— The evolution of a star formation history for three populations, e.g., halo, bulge, and disk stars. The SFR, which is divided by the total stellar mass of each population, as a function of time is shown. The solid, dashed and dotted lines correspond to the bulge, halo and disk stars.

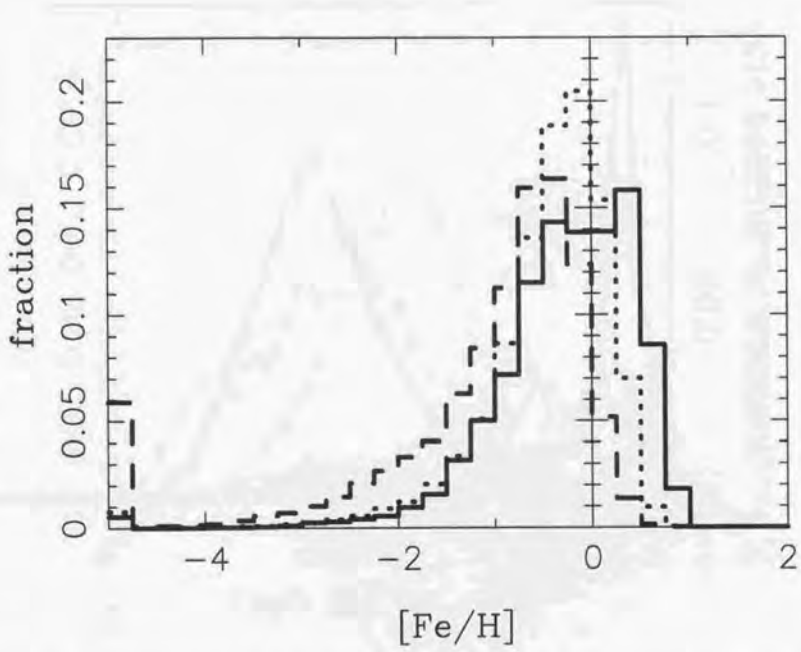

Fig. 13.— The metallicity distribution function for three populations is shown. The solid, dashed and dotted lines correspond to the bulge, halo and disk stars.

Fig. 14.— The projected particle positions at $t = 5$ Gyr for three components is shown. From the left panel, the metal-poor stars, the metal-rich and old stars, and the young stars. The size of the panel is 20Kpc × 20Kpc.

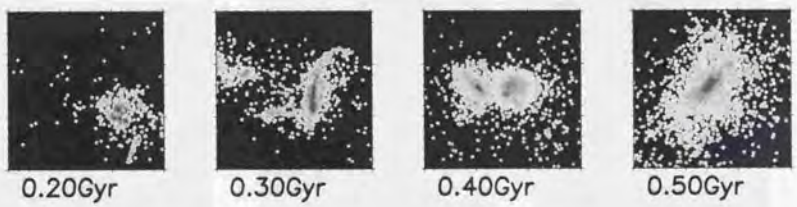

Fig. 15.— The projected stellar density for the first 0.5 Gyr of the evolution. The number located at the bottom of the each panel is the elapsed time in Gyr. During t = 0.4 - 0.5 Gyr, two clumps merge together.

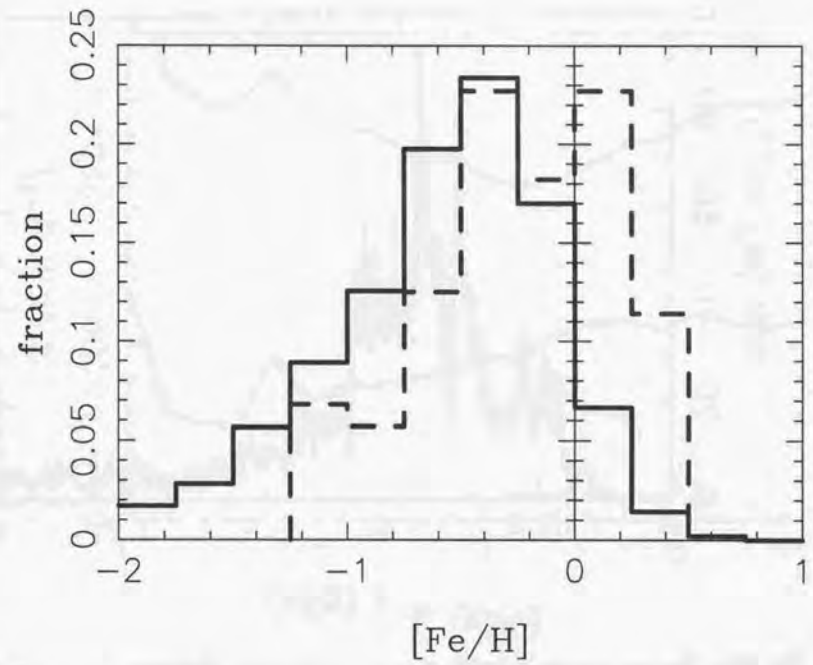

Fig. 16.— The metallicity distribution function of the bulge stars. The solid line is our model and the dashed line is the observed distribution.

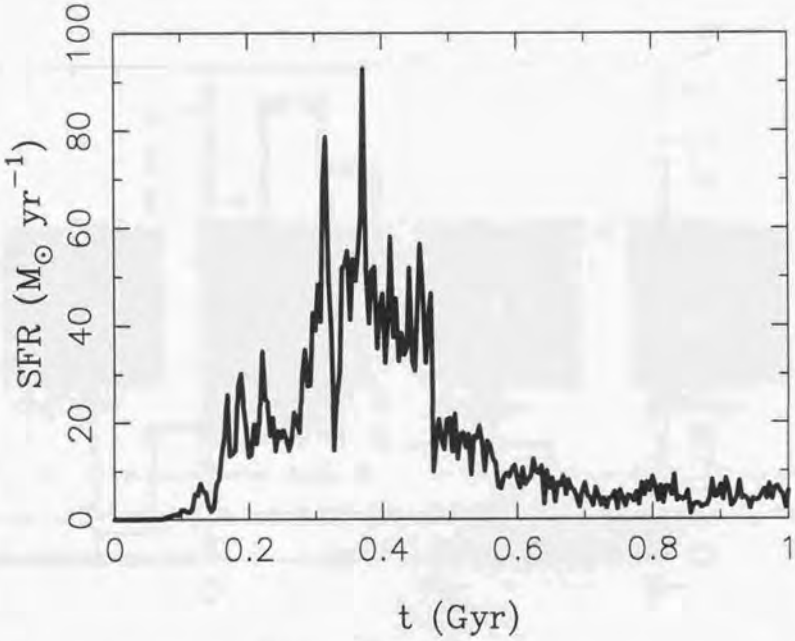

Fig. 17.— The star formation history of the true bulge stars. Each peak appeared in the plot may correspond to a merger event. The two highest peaks are caused by the merger event of two dominant clumps.

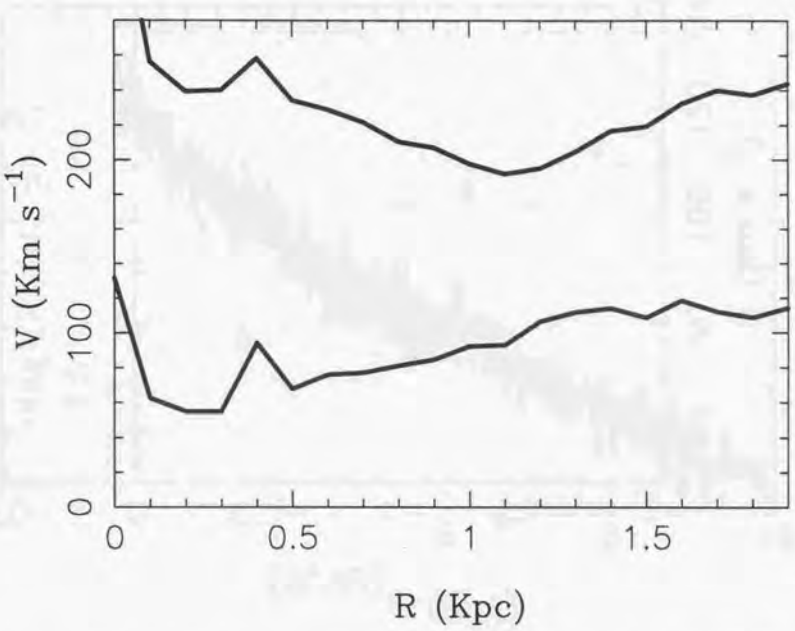

Fig. 18.— The mean velocity and the velocity dispersion for the bulge stars. The upper and lower lines are the mean velocity and velocity dispersion, respectively.

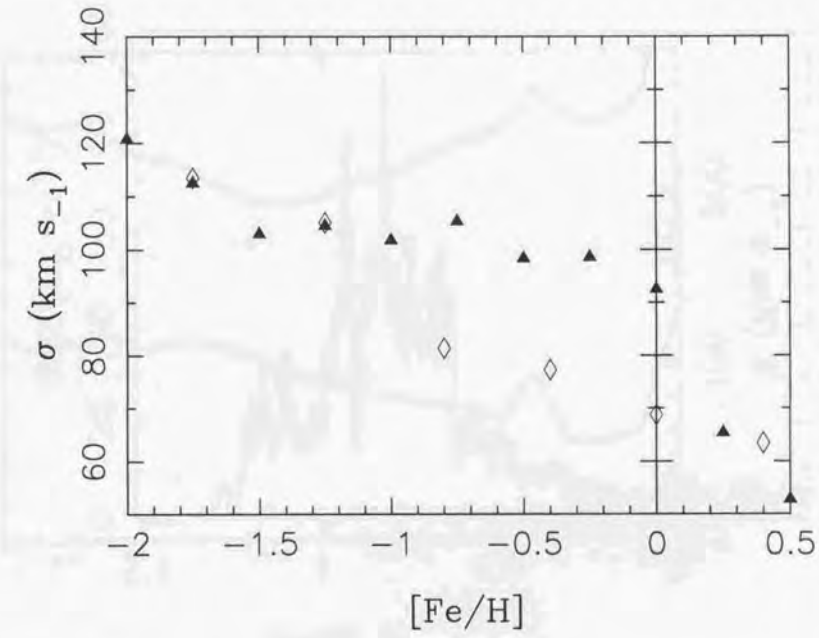

Fig. 19.— The mean velocity dispersion for the bulge stars as a function [Fe/H] is shown. The solid triangle is the our result and the square box is the observational results. The dispersion in the observation is $\sim$ 14 - 8 km s^{-1}.

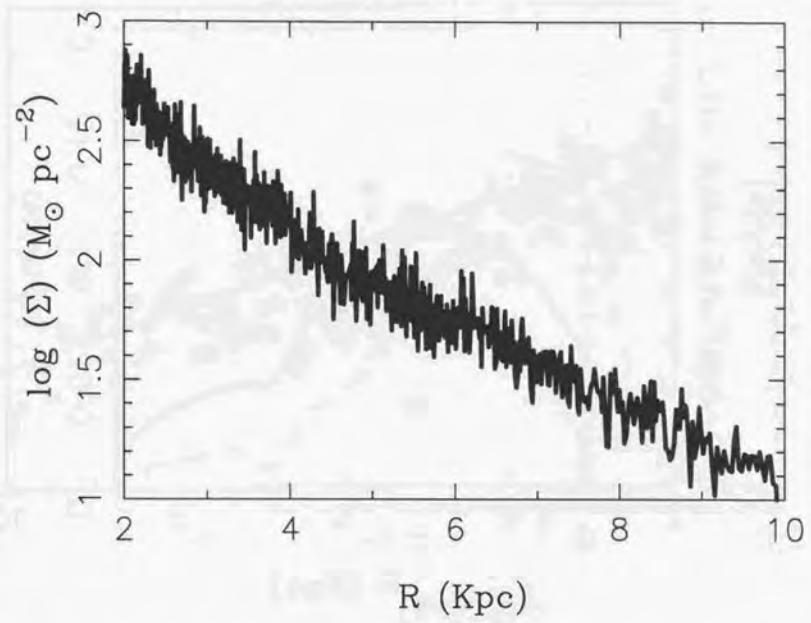

Fig. 20.— The projected stellar surface density profile for disk stars is shown. The scale length of the exponential profile is $\sim$ 5 Kpc.

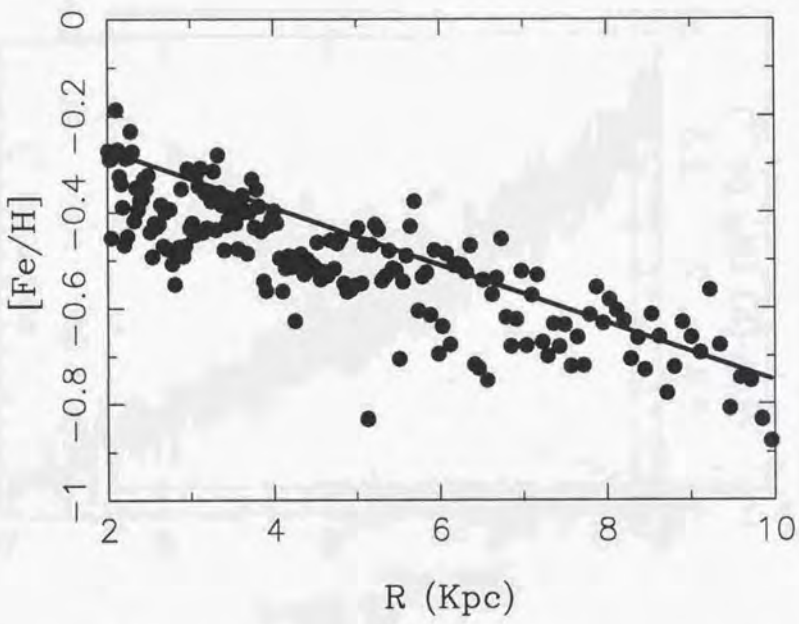

Fig. 21.— The relation between the metallicity ([Fe/H]) and the radius is shown. The straight line shows the observed gradient (~ -0.065 dex Kpc^{-1}).

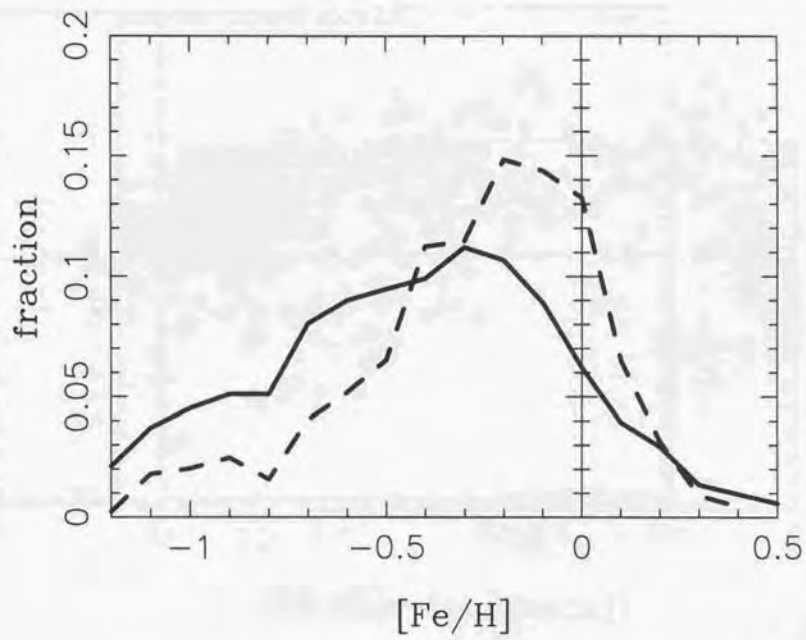

Fig. 22.— The metallicity distribution function of the solar cylinder stars (see text). The solid line is our model and the dashed line is the observed distribution.

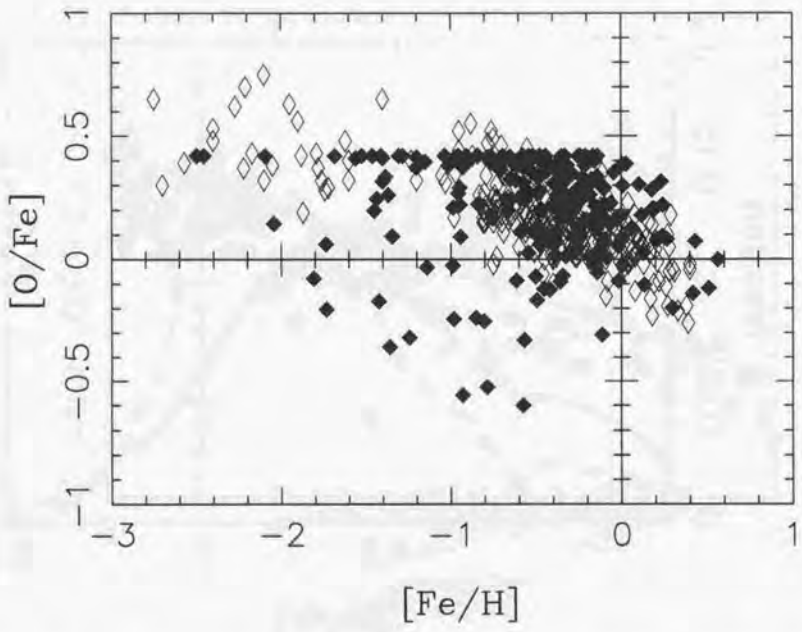

Fig. 23.— The relation between [O/Fe] and [Fe/H] for the solar cylinder stars. The solid dots are our model and the boxed dots are the observations.

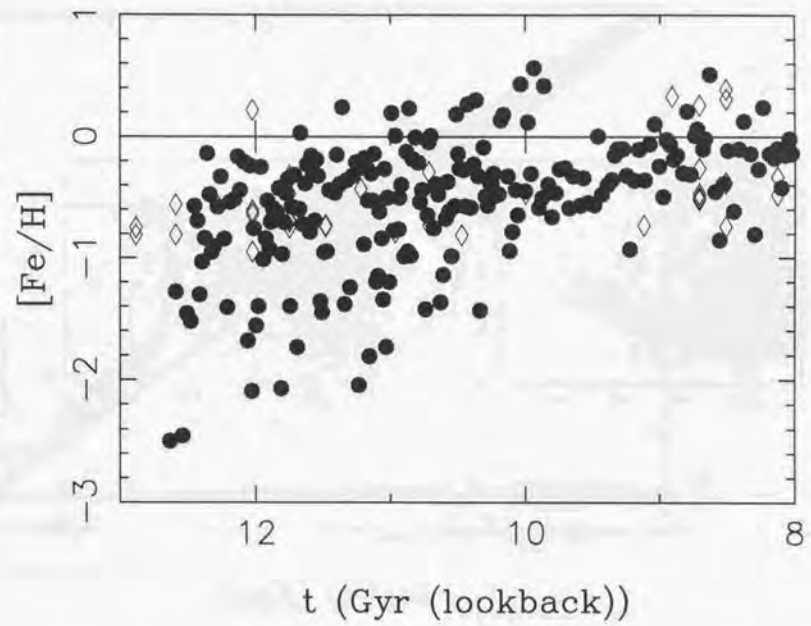

Fig. 24.— The age-metallicity relation for the solar cylinder stars. The solid dots are our model and the boxed dots are the observations.

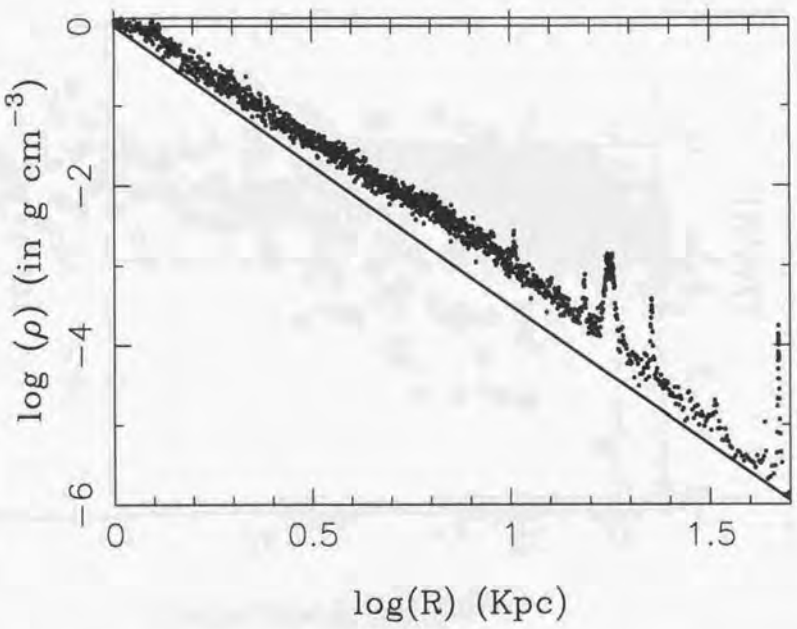

Fig. 25.— The stellar density profile of the outer halo is shown with dots. The strait line represents the observed density profile obtained by the halo globular clusters.

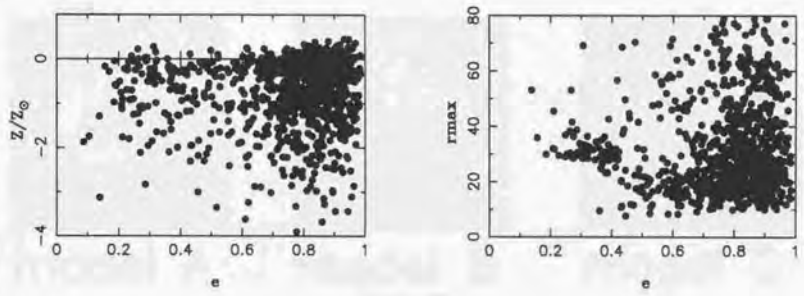

Fig. 26.— The relation between the estimated eccentricity of the halo stars and, the metallicity ([Z/Z$_\odot$]) (left panel) and the r_{max} (the maximum distance reached by the star) (right panel).

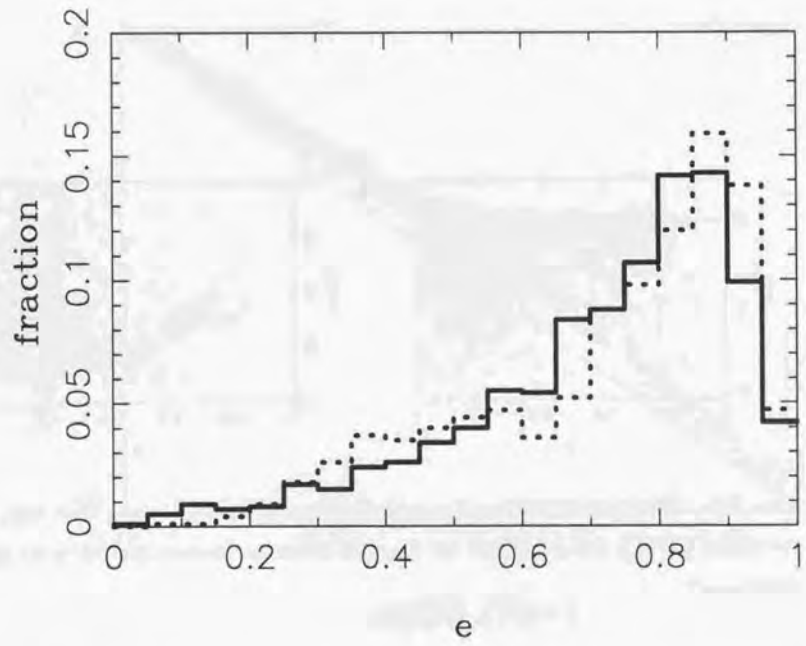

Fig. 27.— Normalized e-distribution function for the halo stars. The solid and dotted lines correspond to the stars with $[Z/Z_\odot] < -3$ and $-2 < [Z/Z_\odot] < -1$, respectively.

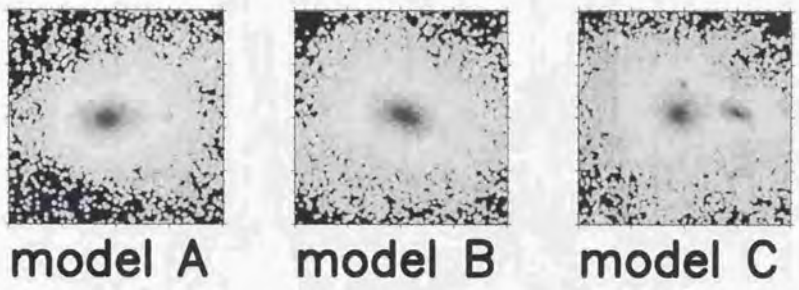

Fig. 28.— The projected dark matter density image at $t = 3$ Gyr for three model. The model A and B are the single-halo model and the model C is the double-halo model. The size of the panels is 200Kpc × 200Kpc.

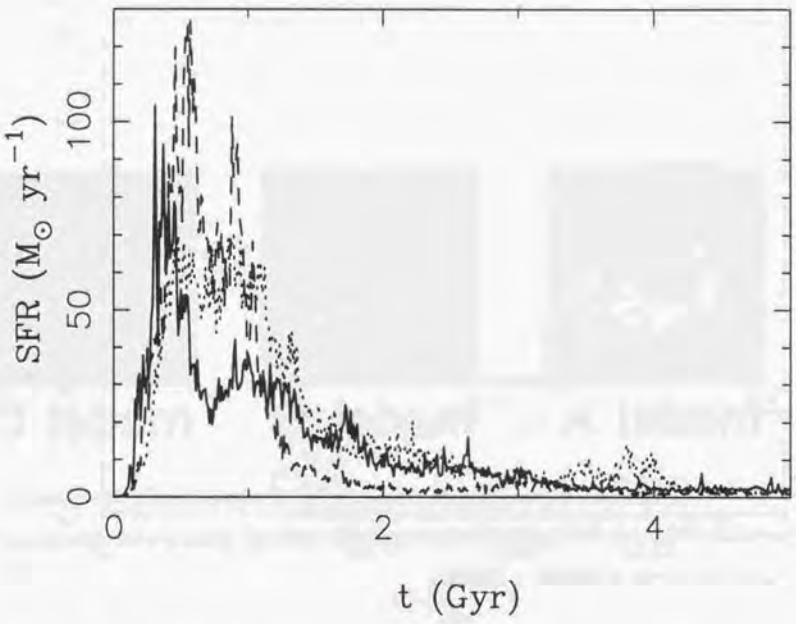

Fig. 29.— The SFR as a function of time for the model A (solid), B (dashed), and C (doted).

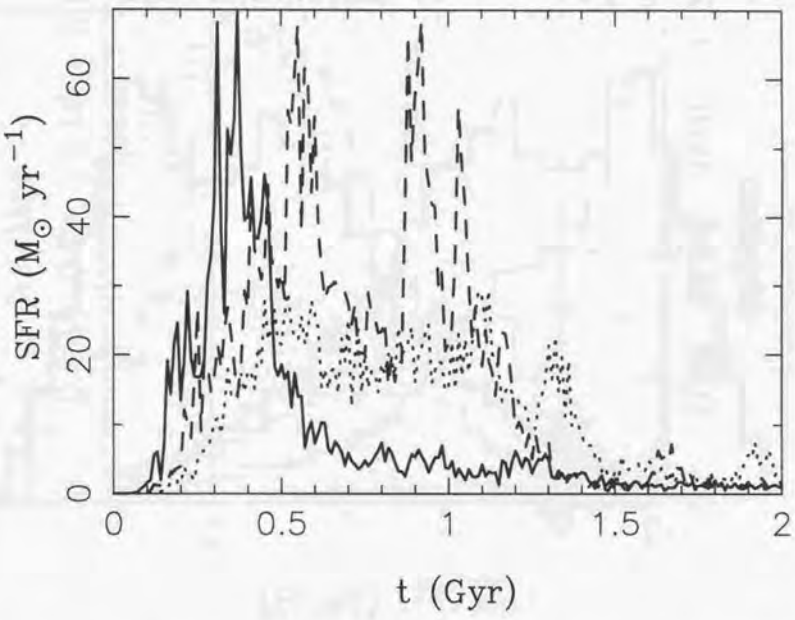

Fig. 30.— The SFR of the central stars as a function of time for the model A (solid), B (dashed), and C (doted).

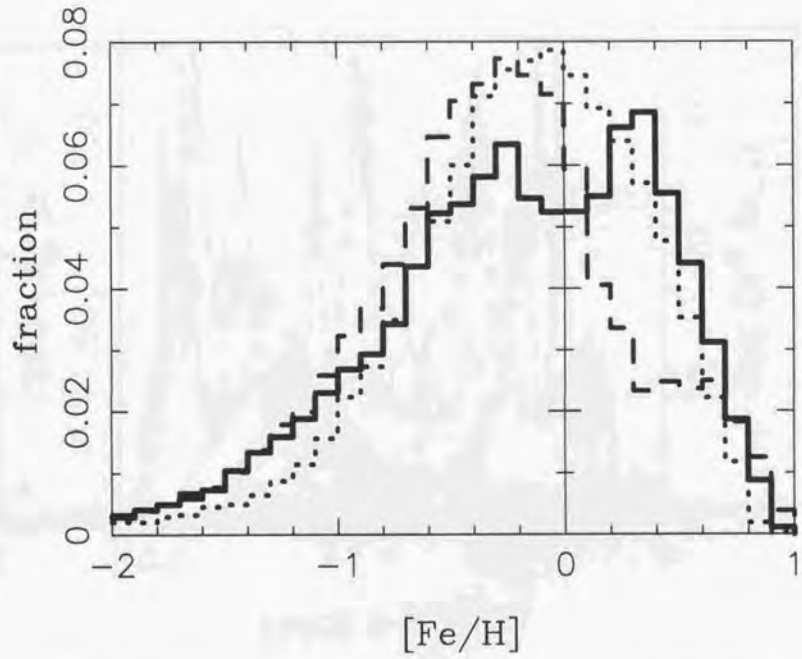

Fig. 31.— The metallicity distribution function of the central stars for the model A (solid), B (dashed), and C (doted).

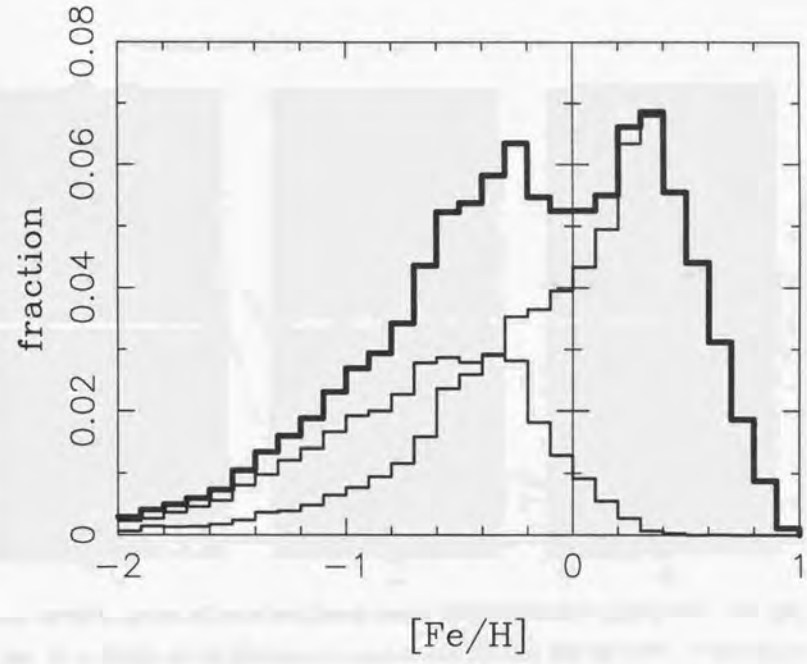

Fig. 32.— The metallicity distribution function of the central stars for the model A with the thick solid line. The left and right distribution function with thin lines correspond to the very old stars ($t < 0.5$ Gyr) and other stars, respectively

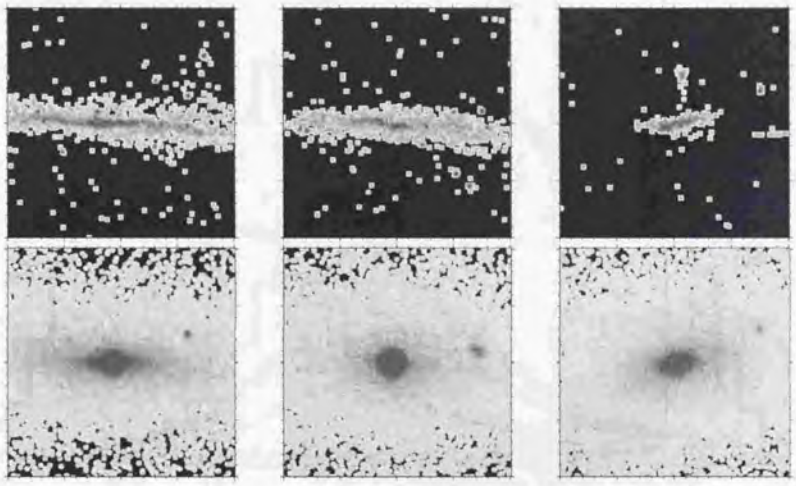

Fig. 33.— The projected density of gases (upper panel) and stars (lower panel) for the model A, B, and C. From the left column, each column corresponds to the model A, B, and C, respectively.

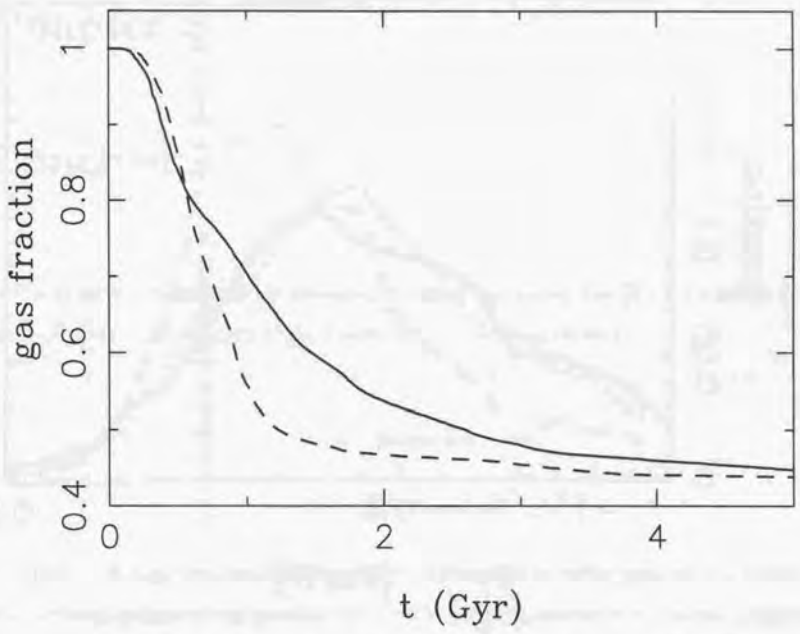

Fig. 34.— The mass fraction of gases in the baryon as a function of time for the model A and B.

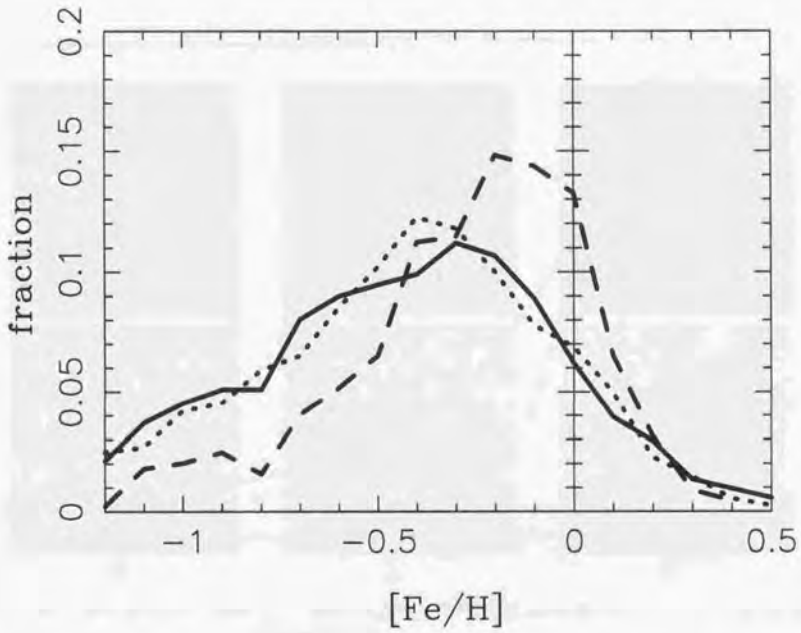

Fig. 35.— The metallicity distribution function of the solar cylinder stars (see text) for $R_f = 0.5$ Kpc (solid line), $R_f = 0.8$ Kpc (dotted line) and the observed distribution (dashed line).

Chapter 5

Conclusion

In this chapter, I summarize the results of my numerical simulations of the formation and chemical-dynamical evolution of the Galaxy and the globular clusters.

1. Summary

1.1. SPH method

First, I describe own numerical code for the formation of stellar systems and present the results of number of test calculations. I adopt the SPH method to model the formation of stellar systems. The SPH formulation of Navarro & White (1993) is used to implement the SPH method. I use the smoothing length that can vary spatially and evolve with a time. The equation of motion is integrated with a second order scheme. To simulate the formation of a stellar system from gases, the SPH code treats three different particles as dark, gas and star particles. The gravity between these particles is computed by the special purpose computer GRAPE to accelerate calculations (GRAPE-SPH code). This GRAPE-SPH code incorporates the various physical processes associated with the formation of stellar systems:

radiative cooling of gases, star formation, energy feedback from stars including stellar winds and supernovae, and chemical enrichment by stars. For the evolution of the metal-free cloud, I solve the rate equation of hydrogen and helium plasma to follow the formation and destruction of H_2 molecules. For the evolution of the metal-enriched cloud, I use the metallicity dependent cooling function to solve the energy equation. The feedback process is implemented self-consistently. In the GRAPE-SPH code, the chemical evolution of total metal (Z), iron (Fe) and oxygen (O) are computed. At last, own GRAPE-SPH code is an up-to-date SPH implementation for the formation of stellar systems. The number of test calculations indicates that this SPH implementation reproduces the analytic solution and the numerical results by previous authors.

1.2. Globular cluster formation

Using own GRAPE-SPH code, I investigate the formation processes of the globular clusters. For the processes of globular clusters formation, only the qualitative scenarios have been discussed previously. In this thesis, I present the first attempt to simulate the globular cluster formation using own GRAPE-SPH code. I assume that, in the collapsing galaxy, isothermal cold clouds form through thermal condensations and become proto-globular clouds (PGC). With this assumption, the size of the PGC is obtained by means of the linear stability analysis. Using these results, I compute the evolution of the inner region of the PGC starting from various initial radius R_i. The results of the calculations are summarized as follows:

1. In order for the globular cluster-like system to form from a metal-free PGC, the initial concentration of the PGC must be large enough.

2. It is required that the metallicity of a PGC is high enough to produce the globular

cluster-like system. The required metallicity is estimated to be $[Fe/H] \geq -2$.

3. In all cases, the shell like structure of the gas forms. Although the star formation occurs in the shell, the self-enrichment is not seen to occur.

1.3. Formation of the Galaxy

All previous numerical models of the formation of the Galaxy lacked the proper treatment of the chemical evolution and/or the required spatial resolutions. In this thesis, I present the results of detailed model of the formation and evolution of the Galaxy using own GRAPE-SPH code.

By introducing the "probability criterion", I can control the global star formation history by one numerical parameter C. The meaning of C is interpreted as follows:

- larger C means lower threshold density.
- smaller C means higher threshold density.

To see how C affects a star formation history, I evolve a spherical top hat over-dense region of mixture of dark matter and gases with different values of C. The result of the calculations indicates that $C = 0.1$ and $C = 1.0$ galaxy resemble the late type and the early type galaxy, respectively. These results are caused by the different star formation history due to the different value of C. The used number of particles in these calculations is too small to make detailed comparisons between our results and the several properties of the Galaxy. Especially, to properly model the chemical evolution of the Galaxy, the larger number of particles is required. Thus, I have done the much higher resolution simulations of formation of the Galaxy as follows.

To efficiently generate the proper initial conditions, I adopt the path integral method to generate a 3 σ over-dense region. By computing the dark matter evolution of each spherical region, we examine the properties of the resulted halos and select the desired halo for hydrodynamical simulations. I select two single-halo models (model A and B) and one double-halo model (model C) as a comparison.

Then, I present the result of the evolution of model A and the detailed comparisons between the model galaxy and the number of observational facts of the Galaxy. By categorizing the stellar components with the metallicity and age, we find that the model galaxy consists of three components as the Galaxy. Each stellar component shows quantitatively similar properties with the properties of the Galaxy.

The early evolution of model A reveals that the most bulge stars form during the merger event that occurred in the region of deepest potential. Because of the strong star burst induced by the merger, the metallicity distribution of bulge component becomes wide as the observation. From this result, I conclude that the galactic bulge can be formed by the sub clump merger in the proto galaxy.

For the disk stars, the age-metallicity relation and the metallicity gradient of the model galaxy match very well with the observation. However, the metallicity distribution function of the model galaxy shows too much metal poor stars than the metallicity distribution function for solar neighborhood stars. The projected surface density of disk stars is well fitted by the exponential profile. This exponential profile is produced by the viscous evolution in the gas disk.

For the halo stars, the density profile of the halo stars shows a $r^{-3.5}$ profile as the observed density profile of outer halo. As expected from the structure formation theory in the CDM cosmology, there is no correlation between the metallicity of a star and, its position and kinematics. The distribution function of the estimated eccentricity of the

halo stars is qualitatively similar to the observed distribution function. I conclude that our numerical model qualitatively reproduce the kinematics of the halo stars.

2. Implication to the formation of the Galaxy

Using the results of our numerical simulations, the formation process of the Galaxy is summarized as follows:

1. In the proto-galactic cloud, the first stars (population III stars) form in the small clumps. At this stage, the proto-galactic gas includes little heavy metal so that the globular cluster formation is not efficient. The stars formed during this time are the halo stars.

2. The small clumps merge gradually and produce larger clumps. Simultaneously, the population III stars eject heavy metal into the ISM. Accordingly, the PGC includes some heavy metal to be able to cool efficiently. Some PGCs eventually form the halo globular clusters and others fail. The failed globular clusters become the halo open clusters or the halo stars.

3. A few large clumps are eventually form by the merging of clumps. Such clumps merge in the galactic center and the strong star burst occurs. The stars formed during this stage are the bulge stars.

4. After the bulge formation, the extended and low-density gases collapse to lead the formation of the gas disk. In the gas disk, the high-density cloud is produced due to the local gravitational instability to form the stellar disk.

5. Owing to the gravitational instability, the viscous redistribution of the angular momentum occurs in the gas disk. After the redistribution of the angular momentum.

the exponential surface density profile of disk is archived.

My high-resolution numerical model of the Galaxy reproduces the number of observational properties of the Galaxy. Especially, the formation process of the galactic bulge is naturally explained in the CDM cosmology. However, the model galaxy has too much metal poor stars than the Galaxy. The reasons for this mismatch with the observations are either a typical initial condition or the incorrect numerical modeling. To investigate the origin of this mismatch, we should construct the even higher resolution model and explore the parameter space of several numerical parameters. If we want to obtain more quantitatively similar model to the Galaxy, I have to investigate the wide range of numerical parameters and/or the initial conditions. Also, higher resolution model will be required to properly model the detailed structure of the Galaxy such as the formation and evolution of the thin disk component.

Acknowledgment: I would like to thank Prof. Ken'ichi Nomoto, my advisor, for his help with this thesis, and T. Shigeyama and M. Mori for useful discussions and suggestions. I also thank other people in our group for useful comments.

Appendix

A. Remote GRAPE system

The Remote-GRAPE is the library, which we have developed for our GRAPE-SPH code, to speed up the calculations. In this section, we briefly describe the Remote-GRAPE and show the results of a performance analysis. The details of the implementation are presented in Nakasato, Mori & Nomoto (1997). Currently, the Remote-GRAPE library is adopted for the GRAPE-3AF system only. However, the adoption of the Remote-GRAPE library for a newer GRAPE system is strait-forward.

A.1. General performance of GRAPE-3AF system

The GRAPE-3AF system (Okumura et al. 1993) has 8 processors on one board, and the GRAPE board is connected to a host computer via VME (Versa Module Europe) bus. The processor chip is designed to calculate gravitational force with a Plummer softening, i.e.,

$$\boldsymbol{f}(\boldsymbol{r}_i) = -G \sum_j^N m_{ij} \frac{\boldsymbol{r}_i - \boldsymbol{r}_j}{(\boldsymbol{r}_{ij}^2 + \epsilon^2)^{1.5}}, \tag{A1}$$

During the force calculation, GRAPE-3AF can construct neighbor lists simultaneously (Fukushige et al. 1991; Okumura et al. 1993). The size of the buffer for neighbor lists is 1024×4byte, which limits the maximum number of neighbors per board.

In this section, we present general performance of GRAPE-3AF system, which is used in our calculations. In our site, we have two GRAPE system. One is a old configuration that the GRAPE boards are connected to Sun SPARC Classic (hereafter Classic) via Aval Data SVA-100 VME interface. Other is a newer configuration that the GRAPE boards are connected to a PC (Pentium Pro 200 MHz; hereafter PC), which runs the Linux operations system, via Bit3 PCI-VME converter interface.

First, we describe the performance of the "Classic" configuration. In Figures 1a (left) and 1b (right), we present the relation between the CPU time and number of particles, N, for different number of GRAPE boards. Figure 1a shows the case that calculates only gravity (hereafter Case G), while Figure 1b shows the case that calculates both gravity and neighbor lists (Case GN). The particles used in these experiments are randomly distributed within the calculation region and the size of the region changes with N to make the number density of particles almost constant. The average number of neighbor particles is almost constant ($\sim$ 40) for any N. In Case G, the performance is dramatically improved by increasing the number of boards. In Case GN, however, the use of larger number of boards does not significantly improve the performance. This is because the speed of the VME bus is too slow to read neighbor lists for large N with many boards, and the calculations required to construct neighbor lists on the host computer is rather costly work for the Classic.

We compare the performances of GRAPE system with different host computers. We use Classic and PC as the comparison. Figure 2a and 2b show cases G and GN, respectively, where the solid and dotted lines represent the cases of Classic and PC, respectively. For Case GN, the computation on host computer (in short, construction of neighbor lists) is longer than Case G. Thus the speed of the host computer apparently affect the performance.

A.2. The motivation to develop the Remote-GRAPE

As mentioned above, a GRAPE-3AF can efficiently calculate gravitational force between particles, and construct neighbor lists. In SPH method, physical quantities at one position are calculated by smoothly averaging over neighbor particles. Thus, SPH simulations are essentially equivalent to N-body simulation with complex, short range "force". The use of GRAPE for Smoothed Particle Hydrodynamics (GRAPE-SPH) can in principle greatly speed up the calculations on WS.

In GRAPE-SPH we can use GRAPE for calculating gravitational force and searching neighbor particles. All other calculations are performed on the host workstation (WS) which is directly connected to GRAPE. The current bottleneck of the performance of GRAPE-SPH is the slow host computer, while the choice of the host computer is limited by the interface of GRAPE-3AF. Steinmetz (1996) summarized the performance of GRAPE-SPH in his table 1 for one GRAPE-3AF board and Sun SPARC Station 10 as a host computer. He showed that about 80 % ($N \sim 60000$) of computing time is spent on the hydrodynamical and miscellaneous calculations, and only $\sim$ 20 % is spent on the GRAPE part. This implies that a higher performance is obtained if we can use a faster WS to calculate the SPH part. Our approach to solve this problem is to develop the software which allows us to use any computer connected to the network as a host of GRAPE. This makes it possible to use a host computer of any vendors and of any performance. For this purpose, we adopt the Parallel Virtual Machine as a basis of the code.

The Parallel Virtual Machine (PVM) is a software that enable us to develop a highly portable parallel program with the message-passing style (Geist et al. 1994). We can solve large computational problems by using a heterogeneous collection of computers as a single parallel computer. In PVM, subroutines to send and receive messages can be called from C language or Fortran. Here the message means that the data which are needed for solving

the problem. We name the library "Remote-GRAPE". The details of the implementation are presented in the section 3 of Nakasato, Mori & Nomoto (1997).

From here, we call a machine on which the main program runs as a `master` machine or `master` side, and a machine which is connected physically to GRAPE boards as a `slave` machine or `slave` side. Also we call the program which runs on the master machine as *master* task and the program which runs on the slave machine as *slave* task. Figure 2 of Chapter 2 shows the concept of our method.

A.3. Performance of SPH with Remote-GRAPE

In this section, we present the results of a performance analysis for GRAPE-SPH with Remote-GRAPE. The general performance of Remote-GRAPE system is presented in the section 4 of Nakasato, Mori & Nomoto (1997).

In order to see the actual advantage of SPH with Remote-GRAPE (hereafter Case SPH-RGN), we make a comparison with the performance of SPH that uses usual GRAPE on the slave machine (Case SPH-GN). We summarize the test cases for GRAPE-SPH in Table 1. The result presented in this sections are obtained with the following configurations; the master machine is DEC Alpha station 600 5/266 (cf. int92/fp92 : 292.8/433.5), and the slave machine is Sun SPARC Classic with five GRAPE-3AF boards. Hereafter all values are obtained from timing on these machines, and the timing is not CPU time but elapsed time.

In Table 2, we show the computing time spent in various parts of the calculation per step, namely, gravity and neighbor ($t_{\rm GRAPE}$), SPH ($t_{\rm SPH}$), and misc ($t_{\rm misc}$), where $t_{\rm GRAPE}$ is the time to calculate gravity and neighbor lists, and $t_{\rm SPH}$ and $t_{\rm misc}$ are, respectively, those for SPH calculations and miscellaneous calculations. The time spent on the host computers ($t_{\rm SPH+misc} = t_{\rm SPH} + t_{\rm misc}$), which has been the bottleneck of the performance in previous

GRAPE-SPH (Steinmetz 1996), differs 20 times between two cases. In Case SPH-RGN, we compare $t_{\rm GRAPE}$, $t_{\rm SPH}$, and $t_{\rm misc}$ for larger N in Figures 3a and 3b. For the adopted configuration, the time spent for gravity and neighbor part occupies the largest fraction of the total time (i.e., $\sim$ 80 %), and the fractions of the three parts are almost independent of N. The large fraction of $t_{\rm GRAPE}$ make the total time per step be $\sim$ 4 times shorter in Case SPH-RGN than Case SPH-GN despite the use of the 20 times faster host computer. This implies that in Case SPH-RGN, the bottle-neck of the performance is now the $t_{\rm GRAPE}$ part rather than the $t_{\rm SPH}$ part. Namely, if we can use faster master machine, it is better to calculate the neighbor lists by "master" machine and use the Remote-GRAPE for only gravity.

One of the best advantage of using the Remote-GRAPE library in the GRAPE-SPH code is that we can compute the hydrodynamical part and gravity part in parallel. The Figure 4 presents the flow-chart of this parallel method. With this parallel method, we can overlap the calculations of gravity ($t_{\rm GRAPE}$) and hydrodynamics ($t_{\rm SPH}$). This means that the total computation time become (τ)

$$\tau = \max(t_{\rm GRAPE}, t_{\rm SPH}) + t_{\rm misc}. \tag{A2}$$

From results in the previous paragraph, in the Case SPH-RGN τ is represented as

$$\tau = t_{\rm GRAPE} + t_{\rm misc}. \tag{A3}$$

Thus, we would better to construct the neighbor lists on the master side in the parallel method. We examine the parallel method and present the results in Figure 5, where the solid and dashed lines correspond to the Case PSPH-RG and Case SPH-RGN, respectively. In the Case PSPH-RG, the neighbor lists are constructed on the master side by using the Tree methods. The enhancement of the performance is rather dramatically. In Table 3, we present comparison of Case SPH-GN, SPH-RGN, and PSPH-RG for $N \sim 10000$. The

performance of case PSPH-RG is 3 times faster than case SPH-RGN, 10 times than case SPH-GN. However, if we use the Tree methods to construct neighbor lists, the clustering state of particles apparently affect the performance. In the case of the SPH simulation including the star formation recipe, the number of gas particles decrease because of the conversion of gas particles to star particles during the evolutions. Thus, in such a actual calculations, the clustering is not a very serious problem.

At last, the best performance is obtained by the following configurations;

- We have to use the state-of-the-art machine for the master side. This will greatly speed up the calculations of hydrodynamical parts.
- Using a faster interconnect between the slave and the master. The use of the 100 Base-T network is 2 times faster than the 10 Base-T network (Nakasato, Mori & Nomoto 1997).
- Searching the neighbor lists on master machine.
- Lastly, the parallel method double the performance of the code.

A.4. Summary

We describe the Remote-GRAPE library and analyze its performance. It allows us to use GRAPE-3A with the computer which is not directly connected to GRAPE. Thus, we can use the state-of-the-art computer as a host computer. We analyze the performance of original GRAPE system in some detail as summarized below:

1. If we calculate only gravity forces, the use of larger number of boards leads to higher performance.

2. In calculating both gravity and neighbor lists, however, the computation required on host WS is larger than the former case, so that the increase of number of the boards is less advantageous.

3. The speed of the host WS dramatically change the performance of GRAPE system.

In the actual application, the performance of our SPH code using Remote-GRAPE is 3 - 4 times faster than the SPH code using original GRAPE on the slave machine. We can get further high (10 times than the SPH on slave machine) performance by using the parallel method with Remote-GRAPE to calculating only gravity. This improvement allow us to model the formation of stellar system with high resolutions.

Table 1. Description of test cases for GRAPE-SPH.

Case	Gravity	Neighbor lists	SPH part	Parallel[a]
SPH-GN	slave	slave	slave	×
SPH-RGN	slave	slave	master	×
PSPH-RG	slave	master	master	○

Note. — "slave" and "master" in each column represent respectively that the part is done on "slave" or "master" machine.

[a]This column indicates whether parallel or not.

Table 2. Comparison of the performance of SPH code with usual GRAPE (S-GN) and Remote-GRAPE (S-RGN).

Case	N[a]	$t_{\rm GRAPE}$[b] sec (%)	$t_{\rm SPH}$[b] sec (%)	$t_{\rm misc}$[b] sec (%)	Total[b] sec
SPH-GN	5000	2.1 (14)	12.1 (84)	0.3 (2)	14.5
SPH-RGN	5000	3.3 (83)	0.6 (17)	0.02 (0)	3.9
SPH-GN	10000	4.2 (15)	23.1 (83)	0.6 (2)	27.9
SPH-RGN	10000	6.2 (83)	1.2 (16)	0.04 (1)	7.4

Note. — [a] N is the number of gas particles.

[b] $t_{\rm GRAPE}$, $t_{\rm SPH}$, and $t_{\rm misc}$ are the elapsed time in gravity plus neighbor, sph, and miscellaneous part, respectively, and their percentage are given in parenthesis. Total is the total elapsed time for one step.

Table 3. Comparison of the performance of Case SPH-GN, Case SPH-RGN and Case PS-RG.

Case	Total sec
SPH-GN	27.9
SPH-RGN	7.4
PSPH-RG	2.5

Note. — The elapse time for one step is shown. $N \sim 10000$.

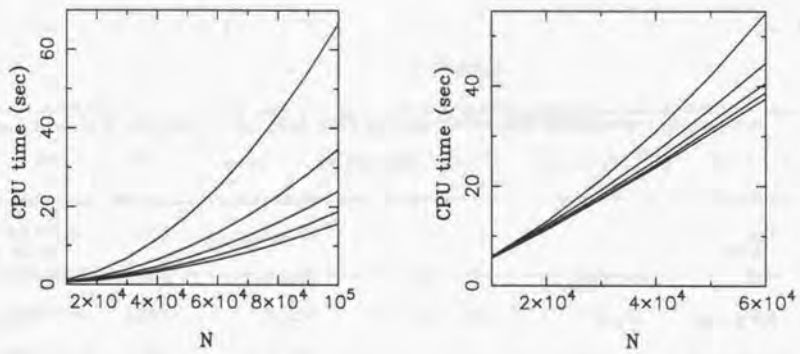

Fig. 1.— (a) left : The CPU time as a function of the number of particles N in calculating only gravitational force (Case G). The five solid lines correspond to the number of GRAPE boards of 1 to 5 from top to bottom. (b) right : The CPU time as a function of the number of particles N in calculating both gravitational force and neighbor lists (Case GN). In both panels, the GRAPE boards are connected to SPARC Classic.

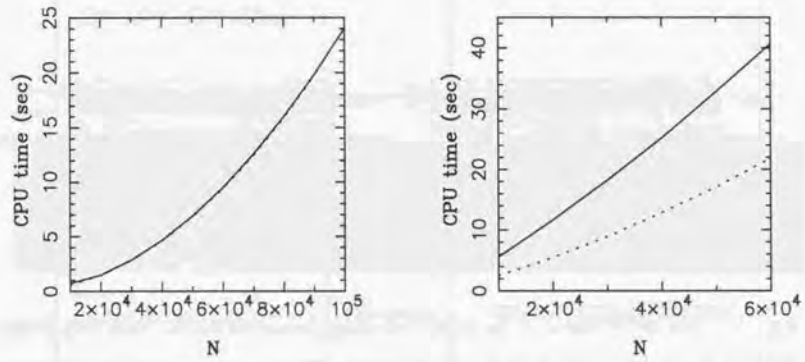

Fig. 2.— The CPU time as a function of N where SPARC Classic (solid) and PentiumPro PC (dotted) are used as a host computer of GRAPE. The number of GRAPE board is three for both machine. (a) left : Case G. (b) right : Case GN.

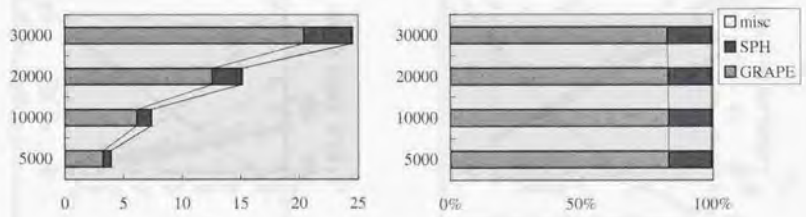

Fig. 3.— The performance of our SPH code using Remote-GRAPE (case SPH-RGN) for different N. (a) left : The elapsed time. (b) right : The fraction occupied by different part of the code.

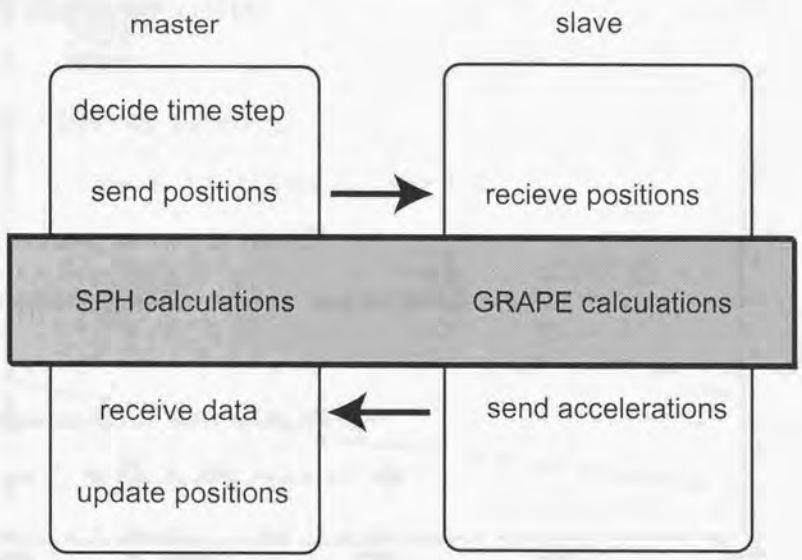

Fig. 4.— The flow-chart of the parallel method. The master machine and slave machine do the hatched tasks (SPH calculations and GRAPE calculations) at the same time, i.e., in parallel. This makes double the speed of the calculations.

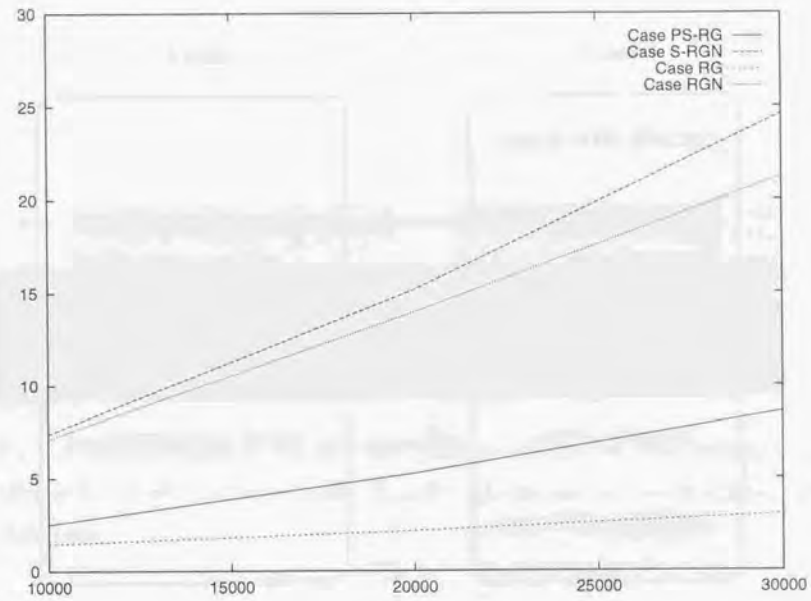

Fig. 5.— The elapse time per step as a function of N in Case PSPH-RG (solid line) and SPH-RGN (dashed line). The dotted and short-dashed lines correspond respectively to case G and case GN.

Bibliography

Abbot, D.C., 1982, ApJ, 263, 723

Abel, G.O., Corwin, H.G., & Olowin, R.P., 1989, ApJS, 70, 1

Alcock et al., 1993, Nature, 365, 621,

Anninos, P., & Norman, M., 1996, ApJ, 459, 12

Armandoroff, T.E., & Zinn, R., 1988, AJ, 96, 92

Armandoroff, T.E., 1989, AJ, 97, 375

Barnes, J., & Hut, P., 1986, Nature, 324, 446

Barnes, J., & Efstathiou, G., 1987, ApJ, 319, 575

Benz, W., Bowers, R., Cameron, A., & Press, W., 1990, ApJ, 348, 647

Bertschinger, E., 1987, ApJL, 323, 103

Bertschinger, E., 1995, http://arcturus.mit.edu/cosmics/

Binney, J., & Tremaine, S., Galactic Dynamics (Princeton: Princeton University Press)

Binney, J., & Merrifield, M., Galactic Astronomy (Princeton: Princeton University Press)

Blanco, V., & Terndrup, D., 1989, AJ, 98, 843

Boesgaard, A.M., et al. 1999, AJ, 117, 1549

Bouwens, R., Cayon, L., & Silk, J., 1999, ApJ, 516, 77

Branch, D., Yungelson, L.R., Boffi, F.R., Livio, M., & Baron, E., 1995, PASP, 107, 1019

Brown, J.H., Burkert, A., & Truran, J.W., 1991, ApJ, 376, 115

Brown, J.H., Burkert, A., & Truran, J.W., 1995, ApJ, 440, 666

Barbuy, B., & Erdelyi-Mendes M., 1989, A&A, 214, 239

Carraro, G., Lia, C., & Chosi, C., 1998, MNRAS, 297, 1021

Chiba, M., & Yosii, Y., 1998, AJ, 115, 168

David, L.P., Forman, W., & Jones, C., 1990, ApJ, 459, 29

Dietrich, M., et al., 1999, A&AL, 352, 1

Djorogovski, S.G., & Meylan, G., 1993, in ASP Conf. Ser. Vol. 50, Structure and Dynamics of Globular Clusters, eds. Djorogovski, S.G., & Meylan, G., (San Francisco: Astronomical Society of the Pacific), 325

Dubath, P., Meylan, G., & Mayor, M., A&A, 324, 505

Ebert, R., 1955, Zs. Ap., 37, 217

Edvardsson, et al., 1993, A&A, 275, 101

Efstathiou, G., & Jones, B.J.T., 1979, MNRAS, 186, 133

Efstathiou, G., Davis, M., Frenk, C.S., & White, S.D.M., 1985, ApJS, 57, 241

Eggen, O.J., Lynden-Bell, D., & Sandage, A.R., 1962, ApJ, 136, 748

Elmergreen, B.G., Efremov, Y., Pudritz, R.E., & Zinnecker, H., 1999, astro-ph/9903136

ESA. 1997, The Hipparcos and Tycho Catalogues (ESA SP-1200) (Noordwijk)

Evrard, A. E., 1988, MNRAS, 235, 911

Fall, S.M., & Rees, M.J., 1985, ApJ, 298, 18

Fall, S.M., & Rees, M.J., 1987, in IAU Symposium 126, Globular cluster systems in galaxies, eds. Grindlay, J. & Philip, D. (Dordrecht: Kluwer), 323

Field, G.B., 1965, ApJ, 142, 531

Friel, E.D., 1995, Annu. Rev. Aston. Astrophys., 33, 381

Friedli, D., & Benz, W., 1995, A&A, 301, 649

Fukushige, T., Ito, T., Makino, J., Ebisuzaki, T., Sugimoto, D., & Umemura, M., 1991, PASJ, 43, 841

Geist, A., Beguelin, A., Dongarra, J., Jiang, W., Manchek, R., & Sunderam, V., 1994, PVM: Parallel Virtual Machine(Cambridge: MIT Press)

Gingold, A., & Monaghan, J., 1977, MNRAS, 181, 374

Gratton, R.G., 1991, in IAU Symp. 145, Evolution of Stars: The Photometric Abundance Connection, eds. G.Michaud & A.V. Tutukov, (Montreal:Univ. Montreal), 27

Greggio, L., & Renzini, A., 1983, A&A, 118, 217

Habe, A., & Ohta, K., 1992, PASJ, 44, 203

Hachisu, I., Kato, M., & Nomoto, K., 1996, ApJL, 470, 97

Hachisu, I., Kato, M., & Nomoto, K., 1999, ApJ, 522, 487

Harris, W.E., 1976, AJ, 81, 1095

Harris, W.E, 1991, Annu. Rev. Aston. Astrophys., 29, 543

Hernquist, L., & Katz, N., 1989, ApJS, 70, 419

Ho, L.C., & Filippenko, A.V., 1996, ApJL, 466, 83

Honma, M., & Sofue, Y., 1997, PASJ, 49, 453

Huchra, J., Geller, M., Clemens, C., Tokarz, S., & Michel, A., 1995, Bull. Inf. C.D.S., 41, 31

Katz, N., 1992, ApJ, 391, 502

Katz, N., Weinberg, D.H., & Hernquist, L., 1996, ApJS, 105, 19

King, I.R., 1962, AJ, 67, 471

Kobayashi, C., Tsujimoto, T., Nomoto, K., Hachisu, I., & Kato, M., 1998, ApJL, 503, 155

Köppen, J., & Arimoto, N., 1990, A&A, 240, 22

Kumai, Y., Basu, & B., Fujimoto, M., 1993, ApJ, 404, 144

Larson, R.B., 1969, MNRAS, 145, 271

Larson, R.B., 1972, Nature Phys. Sci., 236, 7

Lattanzio, C., Monaghan, J., Pongracic, H., & Schwarz, P., 1985, MNRAS, 215, 125

Leitherer, C., Robert, C., & Drissen, L., 1992, ApJ 401, 596

Lin, D.N.C., & Murray, S.D., 1996, in IAU Symposium 174, Dynamical evolution of star clusters, eds. Hut., P. & Makino, J. (Dordrecht: Kluwer), 283

Lucy, L., 1977, AJ, 82, 1013

Maciel, W.J., & Quireza, C., 1999, A&A, 629, 634

Matteucci, F., & Greggio, L., 1986, A&A, 154, 279

Matteucci, F., & Brocato, E., 1990, ApJ, 365, 539

Matteucci, F., Romano, D., & Molaro, P., 1999, A&A, 341, 458

Makino, J., & Funato, Y., 1993, PASJ, 45, 279

Massey, P., & Hunter, D.A., 1998, ApJ, 493, 180

McCrea, W.H., 1957, MNRAS, 117, 562

McWilliam, A., & RIch, R.M., 1994, ApJS, 91, 749

Meerson, B., 1996, Reviews of Modern Physics, 68, 1, 215

Meylan, G., & Heggie, D.C., 1997, A&AR, 8, 1

Minniti, D., 1996, ApJ, 459, 579

Monaghan, J. J., 1992, Annu. Rev. Aston. Astrophys., 30, 534

Monaghan, J.J., & Gingold, R.A., 1983, J. Comput. Phys., 52, 347

Monaghan, J.J., & Lattanzio, J.C., 1985, A&A, 149, 135

Mori, M., Yoshii, Y., Tsujimoto, T., & Nomoto, K., 1997, ApJL, 478, 21

Mori, M., Yoshii, Y., & Nomoto, K., 1999, ApJ, 511, 585

Murray, S.D., & Lin, D.N.C., 1993, ASP Conf. Ser. Vol. 48, 738

Murray, S.D., White, S.D.M., Blondin, J.M., & Lin, D.N.C., 1993, 407, 588

Nissen, P.E., Gustafsson, B., Edvardsson, B., & Gilmore, G., 1994, A&A, 285, 440

Nakasato, N., Mori, M., & Nomoto, K., 1997, ApJ, 484, 608

Nagasawa, M., & Miyama, S.M., 1987, Prog. Theor. Phys., 78, 1250

Navarro, J.F., & Steinmetz, M., 1997, ApJ, 478, 13

Navarro, J.F., & White, S.D.M., 1993, MNRAS, 265, 271

Navarro, J.F., & White, S.D.M., 1993, MNRAS, 267, 401

Noguchi, M., 1998, Nature, 392, 253

Nomoto, K., Yamaoka, H., Shigeyama, T., Kumagai, S., & Tsujimoto, T., 1994, in Supernovae, Les Houces Session LIV, eds. Bludman et al. (Amsterdam: North-Holland), 199

Nomoto, K., Hashimoto, M., Tsujimoto, T., Thielemann, F.-K., Kishimoto, N., Kubo, Y., & Nakasato, N., 1997, Nucl. Phys. A., 616, 79c

Olofsson G., et al., 1999, 350, 883

Okumura, S., Makino, J., Ebisuzaki, T., Fukushige, T., Ito, T., & Sugimoto, D., 1993, PASJ, 45, 329

Osterbrock, D.E., 1974, Astrophysics of Gaseous Nebulae (San Fransisco: W. H. Freeman and Company)

Padmanabhan, T., Structure formation in the universe (Cambridge: Cambridge University Press)

Pagel, B.E.J, 1997, Nucleosynthesis and Chemical Evolution of Galaxies (Cambridge: Cambridge University Press)

Palmer, P.L., & Papaloizou, J., 1987, MNRAS, 224, 1043

Parker, E.N., 1953, ApJ, 117, 431

Peebles, P.J.E., & Dicke, R.H., 1968, ApJ, 154, 891

Pont, E., Mayor, M., & VandenBerg, D.A., 1998, A&A, 329, 87

Raiteri, C.M., Villata, M., & Navarro, J.F., 1996, A&A, 315, 105

Saio, H., & Yoshii, Y., 1990, ApJ, 363, 40

Schmidt, M., 1959, ApJ, 129, 243

Searle, L., & Zinn, R., 1978, ApJ, 225, 357

Shapiro, P.R., Kang, H., 1987, ApJ, 318, 32

Shull, J.M, & Silk, J., 1979, ApJ, 234, 427

Sod, G.A., 1978, J. Comput. Phys., 27, 1

Sommer-Larsen, J., 1991, MNRAS, 249, 368

Spitzer, L., Jr., 1978, Physical Processes in the Interstellar Medium (New York: Wiley Interscience)

Steinmetz, M., 1996, MNRAS, 278, 1005

Steinmetz, M., & Müller, E., 1994, A&A, 281, 97

Steinmetz, M., & Müller, E., 1995, MNRAS, 276, 549

Sugimoto, D., Chikada, Y., Makino, J., et al., 1990, Nature, 345, 33

Suntzeff, N., 1993, in ASP Conf. Ser. Vol. 48, The Globular Cluster-Galaxy Connection, eds. Smith, G.H., & Brodie, J.P., (San Francisco: Astronomical Society of the Pacific), 167

Sutherland, R.S., & Dopita, M.A., 1993, ApJS, 88, 253

Thacker, R.J., Tittley, E.R., Pearce, F.R., Couchman, H.M.P., & Thomas, P.A., 1998, astro-ph/989221

Tsujimoto, T., Nomoto, K., Yoshii, Y., Hashimoto, M., Yanagida, S., & Thielemann, F.-K., 1996, MNRAS, 277, 945

Toomre, A., 1964, ApJ, 139, 1217

Truran, J.W., & Cameron, A.G.W., Ap. Sp. Sci., 14, 179

Umemura, M., Fukushige, T., Makino, J., Ebisuzaki, T., Sugimoto, D., Turner, E., & Loeb, A., 1993, PASJ 45, 311

Yoshii, Y., & Sommer-Larsen, J., 1989, MNRAS, 236, 779

Yoshii, Y., Tsujimoto, T., & Nomoto, K., 1996, ApJ, 462, 266

Zel'dovich, Ya.B., 1970, A&A, 5, 84

Zinn, R., & West, M.J., 1984, ApJS, 55, 45

Zinn, R., 1985, ApJ, 293, 424

Zwart, S.F.P., Makino, J., McMillan, S.L.W., & Hut, P., 1999, A&A, 348, 117